ISBN 978-82-326-0164-6 (printed version)
ISBN 978-82-326-0165-3 (electronic version)
ISSN 1503-8181

Gunhild Allard Reigstad

Doctoral Thesis

Doctoral theses at NTNU, 2014:120

Gunhild Allard Reigstad

Mathematical Modelling of Fluid Flows in Pipe Networks

Doctoral theses at NTNU, 2014:120

NTNU

NTNU
Norwegian University of
Science and Technology
Faculty of Engineering
Science and Technology
Department of Energy and
Process Engineering

NTNU – Trondheim
Norwegian University of
Science and Technology

NTNU – Trondheim
Norwegian University of
Science and Technology

Gunhild Allard Reigstad

Mathematical Modelling of Fluid Flows in Pipe Networks

Thesis for the degree of Philosophiae Doctor

Trondheim, March 2014

Norwegian University of Science and Technology
Faculty of Engineering
Science and Technology
Department of Energy and
Process Engineering

NTNU – Trondheim
Norwegian University of
Science and Technology

NTNU
Norwegian University of Science and Technology

Thesis for the degree of Philosophiae Doctor

Faculty of Engineering
Science and Technology
Department of Energy and
Process Engineering

ISBN 978-82-326-0164-6 (printed version)
ISBN 978-82-326-0165-3 (electronic version)
ISSN 1503-8181

Doctoral theses at NTNU, 2014:120

Printed by Skipnes Kommunikasjon as

Abstract

The mathematical description of splitting and merging of flows is an important part of a detailed heat exchanger simulation model suitable for studying dynamic and static flow instabilities. This thesis considers one such description, the network models for fluid flow in junctions. Briefly described, these models consist of a one dimensional hyperbolic conservation law, the corresponding equation of state, coupling conditions and wave equations. In the present work, the generalized Riemann problem has been considered and thus each pipe section has a constant initial condition.

The set of coupling conditions enables the construction of boundary conditions at the pipe-junction interface of each pipe section connected at a junction. They are defined such that the boundary condition of each section is related to the initial conditions of all the connected pipe sections. The wave equations relate the constructed boundary condition and the initial condition of a pipe section under the restriction that the constructed state must propagate into the section.

This thesis mainly considers network models derived for the isothermal and isentropic Euler equations. A mandatory coupling condition is thus that mass is conserved at the junction. However, as the conservation laws consist of two equations, a second condition is needed. The choice of a momentum related coupling constant, $\mathcal{H}(\rho, v)$, is common in the literature and has therefore been applied in this thesis as well. In particular, the proper selection of the coupling constant expression has been the main focus of the work.

Both pressure and momentum flux have been commonly applied as momentum related coupling constant in network models presented in the literature. In this thesis, existence and uniqueness of solutions to the generalized Riemann problem have been proved for network models that apply the two different constants. The proof is restricted to sets of initial conditions that belong to the subsonic region. That is, the region where both the initial conditions and the solutions are subsonic.

An investigation of the physical soundness of the solutions for a junction

connecting three pipe sections revealed that none of the proposed coupling constants yield physical solutions for all subsonic flows at the pipe-junction interfaces. In particular, a duality was observed for isothermal flows. In the flow-ranges where pressure as coupling constant yields physical solutions, momentum flux yields unphysical solutions, and opposite. Unphysical solutions are characterised by the presence of energy production in a junction.

The lack of physically sound solutions within the entire subsonic region lead to a search for an alternative coupling constant. As a result, the Bernoulli invariant has been suggested and existence and uniqueness of solutions to the corresponding generalized Riemann problem have been proved for sets of initial data that belong to the subsonic region. It has also been proved that the constant yields physically sound solutions for all subsonic solutions.

A numerical implementation of three network models based on the isothermal Euler equations have been performed in addition to the theoretical investigation. The three different models applied pressure, momentum flux and Bernoulli invariant as momentum related coupling constant, respectively. Test cases for three different network layouts were derived, and corresponding numerical results presented. Each set of simulation results has been analysed with respect to physical soundness. All cases are seen to support the analytically based conclusion; only Bernoulli invariant as momentum related coupling constant yields physical solutions for all sets of initial conditions that belong to the subsonic region.

Preface

My PhD has been carried out in the period from May 2010 to April 2014 at the Department of Energy and Process Engineering at NTNU. It has been a journey in new knowledge, in the joy of discovering promising results, the frustration of facing overwhelming complex problems and the long hours needed in order to present ones results such that they are available to others. The work has been performed within the project "Enabling low emission LNG systems" which is led by SINTEF Energy Research. I gratefully acknowledge the support of the project partners; Statoil and GDF SUEZ, and the Research Council of Norway (193062/S60) for support through the *Petromaks* programme.

A special thanks also goes to my main supervisor, Tor Ytrehus (NTNU) and my co-supervisor Tore Flåtten (SINTEF Energy Research/SINTEF Materials and Chemistry). Tor Ytrehus for giving me great guidance as I entered into the work, for insightful discussions on physical principles as the questions arose and for a good closure of the work. Tore Flåtten for being a research partner spending time and energy entering into the topic of network models together with me and for providing vital results for me to build on.

There are many people who have made these years enjoyable. My colleagues who have given me nice lunch-breaks, Halvor Lund and Karl Yngve Lervåg who have helped me with the many facets of Linux, Alexandre Morin who proof read parts of this thesis and my friends and extended family who have cared and given me joyful memories - thank you very much.

Finally I would like to thank the two most special persons in my life; my husband Tor Inge and my daughter Ingvild Margrete. Being loved by you, and loving you, makes me complete. Without you Tor Inge, your support and extra effort at home, this journey would not have been possible.

Trondheim, March 2014
Gunhild Allard Reigstad

Contents

"It is open to every man to choose the direction of his striving; and also every man may draw comfort from Lessing's fine saying, that the search for truth is more precious than its possession."

Albert Einstein

1 Introduction

How can the flow conditions in pipe sections connected at a junction be correctly described? In this thesis, the question has been approached by considering the mathematical description of such problems, known as "network models". The models have been investigated both by mathematical techniques and by analysis of numerical results. Throughout the investigation the physical soundness of the solutions has been the main evaluation criterion.

1.1. Background and Motivation

In the process of liquefying natural gas, heat exchangers play a central role. Correspondingly, the total efficiency of an LNG[1] production plant is highly influenced by the performance of a set of heat exchangers.

When designing an industrial plant, it is important to obtain optimal conditions for the overall plant within the feasible ranges of each of the components installed. Optimal conditions may for instance be measured as minimum investment and operating costs at a given production rate. The design process is complex, as one in many cases must iterate between overall plant evaluations and performance calculations of each component. The

[1] Liquefied Natural Gas

complexity is due to the fact that CPU-time restrictions limit the detail level describing each component when the assembled plant is to be evaluated.

For heat exchanger units, the detailed simulation models are often based on the assumption that the exchanger is well-behaved and can be treated in a relatively simplified manner. However, in some cases exchangers must be designed with great care for this assumption to hold. One such example is the design of heat exchangers where a multicomponent refrigerant consisting of light hydrocarbons evaporates [47]. Such heat exchange is present in several liquefaction concepts, like the MFC [44], SMR [28], DMR [28] and APCI processes [38] as well as the proposed Liquefin [47] process.

In their theoretical study, Skaugen et al. [50] showed how unfortunate thermo-hydraulic design could yield large spacial and temporal temperature variations within compact heat exchangers applied in an SMR process. Such variations could lead to reduced performance and an increased likelihood of cracks in the exchangers due to material fatigue. They showed that a re-design of the exchanger would be necessary to remove the risk for the unwanted behaviour. As a consequence, either the energy demand of the plant or the size of the heat exchanger would increase.

The presented analysis was based on steady state simulations that indicated an unfortunate sensitivity to mal-distribution of flows. It is very common that a stream which enters a heat exchanger from the piping of the overall plant is divided into several sub-streams. These should ideally be equal in terms of mass flux per area. However, small disturbances are likely to occur, such that there is a slight difference between the streams. Normally such a disturbance would have negligible consequences, and the flow conditions in the exchanger would remain close to the designed operating point. For certain combinations of fluids, heat exchanger geometries and number of parallel sub-streams, a small deviation would result in significantly different flow conditions. This is known as Ledinegg instability [50].

While a single component fluid evaporates at a constant temperature, a multicomponent fluid will have a change in fluid temperature as it is heated from the saturated liquid– to the saturated gas state. A set of sub-streams with large temperature differences throughout the exchanger could therefore at certain conditions be the consequence of having significant mal-distribution of flows [50].

The consequences of Ledinegg instability have been experimentally investigated and documented for parallel flow in pipe sections [29]. However, for heat exchanger applications, and in particular for compact designs applied extensively within LNG processes, the number of parallel streams are high.

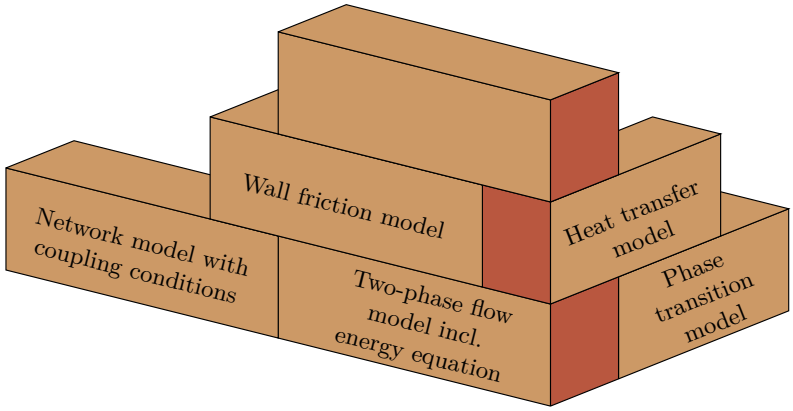

Figure 1.1.: Illustration building blocks relevant for CFD based simulation model

Consequently it is a difficult task to predict the occurrence of the instability. Skaugen et al. [50] applied a heat exchanger model which predicts steady state conditions. Steady state simulation results were also applied in another study performed by Rolland et al. [47]. Such results are suitable to identify designs for which there is a risk of having Ledinegg instability. However, if one wants to verify that the performance of an exchanger will be influenced by the instability, more detailed numerical models are needed. The models must also account for dynamic flow conditions within the exchanger. This insight, together with the lack of such models, has lead to the desire to develop more detailed and robust heat exchanger models for general purposes.

One possible way to achieve a more detailed model is to use the approach of computational fluid dynamics (CFD). This is however not straightforward and many challenges must be overcome before a suitable model is available. In Figure 1.1, different building blocks of such a model are indicated. The model should describe the dynamics both at the entry and exit points, and within the heat exchanger. At an entry point, the incoming flow would usually be split into several sub-streams. Similarly, at the exit point, the sub-streams would merge into one stream. These points may be viewed as a kind of junctions.

Within the heat exchanger, it is important that the model describes the flow conditions. Conservation equations for mass, momentum and energy should be applied, and both single phase and two-phase flow conditions

should be described properly. The latter condition is relevant for the parts of the heat exchanger where a stream is partially evaporated or condensed such that both a gas and a liquid phase exist. The models should as well describe the phase transition process of evaporation and condensation. In addition, heat transfer and frictional forces at the wall-fluid interface should be accounted for.

The focus of this PhD was decided to be on the splitting and merging processes. In particular it was decided to investigate the suitability of the network theory for fluid flows, a mathematical approach based on the generalized Riemann formulation. Initially, two-phase flow models like the drift-flux and the two-fluid models were seen as the most relevant conservation laws for which network models should be considered. However, as the work was initiated it became clear that there were unresolved questions concerning network models for single phase flow that needed to be settled first. Therefore, focus was shifted towards network models based on the Euler equations.

1.2. Outline of the Thesis

In the present thesis, network models based on the isothermal and isentropic Euler equations have been investigated. In addition, there exists network models for the Euler equations and the drift-flux model. The outline of the thesis is as follows:

- An introduction to the various conservation laws is given in Chapter 2.
- Chapter 3 describes the generalized Riemann problem formulation that the network theory for fluid flows is based upon. Since the solutions of these problems are based upon the solutions of the standard Riemann problem, this problem and its solutions are shown first.
- Chapter 4 presents an overview of modelling approaches for junction flow and relevant literature. This includes approaches based upon network theory as well as on finite junction volume and correlation based approaches.
- In Chapter 5, an introduction is given to the five scientific papers that constitute the main contribution of this thesis.
- The results are summarised in Chapter 6 and an outlook on further work is given.

- Appendix A shows detailed calculations on the shock wave equations derived in Section 3.1.
- Appendix B to F contain the main contribution of the thesis; five scientific papers that concern
  - An improved Roe solver for the drift-flux two-phase flow model
  - Coupling constants and the generalized Riemann problem for isothermal junction flow
  - Numerical network models and entropy principles for isothermal junction flow
  - Numerical investigation of network models for isothermal junction flow
  - Existence and uniqueness of solutions to the generalized Riemann problem for isentropic flow

"Remember that all models are wrong; the practical question is how wrong do they have to be to not be useful. "

George Edward Pelham Box

2 Physical Models

Network models have mainly been developed for fluid flow described by the Euler equations for gas dynamics or simplified sets of equations based on the assumption of isentropic or isothermal flow [e.g. 2, 3, 14, 16]. Models have also been developed for the drift-flux model [4, 5]. In the following, the various conservation laws will be described.

2.1. The Euler Equations

2.1.1. The general Euler equations

The general Euler equations for an M dimensional problem are stated as

$$\frac{\partial \rho}{\partial t} + \nabla \cdot (\rho \boldsymbol{v}) = 0, \tag{2.1}$$

$$\frac{\partial}{\partial t}(\rho v_j) + \sum_{i=1}^{M} \frac{\partial}{\partial x_i}(\rho v_i v_j) + \frac{\partial p}{\partial x_j} = 0 \qquad \forall j \in [1, \ldots, M], \tag{2.2}$$

$$\frac{\partial E}{\partial t} + \nabla \cdot (\boldsymbol{v}(E + p)) = 0. \tag{2.3}$$

The equations describe conservation of mass (2.1), linear momentum (2.2) and total energy (2.3) for a thermodynamic system, that is for matter within

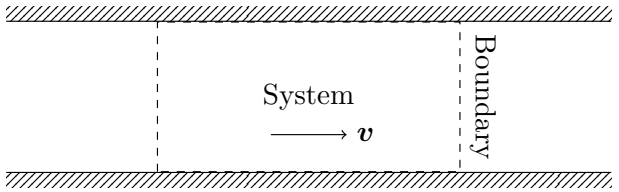

Figure 2.1.: Thermodynamic system, its boundary and surroundings

a closed boundary which separates the system from its surroundings [32, 35]. An example of such a system is shown in Figure 2.1.

The Euler equations are valid for compressible and incompressible fluids with negligible viscosity and heat conductivity. Additionally, body forces are neglected [31, 53]. In the equations ρ is the fluid density, $\boldsymbol{v}$ is the fluid velocity, $\rho\boldsymbol{v}$ is the mass flux and p is the pressure. The total energy is defined as

$$E = \frac{1}{2}\rho\boldsymbol{v}^2 + \rho e, \tag{2.4}$$

where the internal energy fulfils the $T\,\mathrm{d}s$ relation [35, Eq. (6.17a)]

$$de = Tds + \frac{p}{\rho^2}d\rho. \tag{2.5}$$

Here e is specific internal energy, T is absolute temperature and s is the specific entropy.

A complete description of the problem is only available when an equation of state is given. This equation relates pressure to the conserved variables, ρ, ρv and E. For the Euler equations it is common to use an equation of state derived for ideal, calorically perfect gases. An ideal gas has the property that the internal energy, e, is a function of absolute temperature, T, alone [35, p 96].

$$e = e\left(T\right). \tag{2.6}$$

An expression for the internal energy may be derived from the definition of the specific heat at constant volume

$$c_v\left(T\right) = \frac{\mathrm{d}e}{\mathrm{d}T}. \tag{2.7}$$

If the gas is calorically perfect, c_v is a constant, and internal energy simply becomes [32]

$$e\left(T\right) = c_v T. \tag{2.8}$$

Similarly, for an ideal gas the specific heat at constant pressure, c_p, is a function of temperature alone

$$c_p\left(T\right) = \frac{\mathrm{d}h}{\mathrm{d}T} \tag{2.9}$$

and is a constant for a calorically perfect gas. Here h is the specific enthalpy which is related to the internal energy as

$$h = e + \frac{p}{\rho}. \tag{2.10}$$

Pressure, temperature and density of an ideal gas are related by the equation of state

$$p = \rho R T, \tag{2.11}$$

where R is a gas dependent constant equal to the universal gas constant $\bar{R}$ divided by the molecular weight of the gas. By applying this equation together with the specific heat differentials [(2.7), (2.9)], the specific heats are seen to be related by R through

$$c_p(T) = c_v(T) + R. \tag{2.12}$$

γ is defined as the ratio between the two specific heats

$$\gamma(T) = \frac{c_p(T)}{c_v(T)}. \tag{2.13}$$

–Due to (2.12) it is obvious that $\gamma > 1$.

The equation of state may be rewritten by inserting the original equation (2.11) into the expression for internal energy (2.8) and apply the equation relating the gas constant to the specific heats (2.12) together with the definition of γ (2.13)

$$e = \frac{p}{\left(\gamma - 1\right)\rho}. \tag{2.14}$$

Rearranging and using the expression for the total energy given in (2.4), pressure may be expressed as

$$p = \left(\gamma - 1\right)\left(E - \frac{1}{2}\rho v^2\right). \tag{2.15}$$

It should be noted that this expression is valid for calorically perfect gases only, as Equation (2.8) is based on this condition.

For a one dimensional problem, the conservation equations (2.1)- (2.3) reduce to

$$\frac{\partial \rho}{\partial t} + \frac{\partial}{\partial x}(\rho v) = 0, \tag{2.16}$$

$$\frac{\partial}{\partial t}(\rho v) + \frac{\partial}{\partial x}\left(\rho v^2 + p\right) = 0, \tag{2.17}$$

$$\frac{\partial E}{\partial t} + \frac{\partial}{\partial x}(v(E+p)) = 0, \tag{2.18}$$

for the three fundamental variables ρ, v and E, with p given from (2.15).

2.1.2. The isentropic and isothermal Euler equations

For the special case of gas flows with initially uniform entropy and only small, smooth perturbations around a background state, the assumption of constant entropy holds. Under these assumptions, the isentropic Euler equations may be applied [31]. The equations consist of the mass- and momentum conservation equations of the general Euler equations, together with an equation that describes the constant entropy. The last equation replaces the energy equation of the general Euler equations. Thus, for a one dimensional problem, the equations may be written as

$$\frac{\partial \rho}{\partial t} + \frac{\partial}{\partial x}(\rho v) = 0, \tag{2.19}$$

$$\frac{\partial}{\partial t}(\rho v) + \frac{\partial}{\partial x}\left(\rho v^2 + p\right) = 0, \tag{2.20}$$

$$\mathrm{d}s = 0. \tag{2.21}$$

At isentropic conditions, the equation of state (2.11) may be rewritten by using the $T\,\mathrm{d}s$ relation (2.5). Due to the constant entropy assumption (2.21), this reduces to

$$\mathrm{d}e = \frac{p}{\rho^2}\,\mathrm{d}\rho. \tag{2.22}$$

Inserting the differential relation for c_v (2.7), the equation of state (2.11) and the relation between the gas constant and specific heats (2.12), we obtain

$$c_v\,\mathrm{d}T = (c_p - c_v)\frac{T}{\rho}\,\mathrm{d}\rho. \tag{2.23}$$

A separation of the variables then gives

$$\frac{1}{(\gamma-1)\,T}\,\mathrm{d}T = \frac{1}{\rho}\,\mathrm{d}\rho. \tag{2.24}$$

For a calorically perfect gas, γ is constant and thus integration of (2.24) yields

$$\frac{\rho}{\rho_0} = \left(\frac{T}{T_0}\right)^{\frac{1}{\gamma-1}}, \tag{2.25}$$

where the subscript 0 refers to a reference state. By applying the equation of state (2.11), (2.25) may be rewritten to a function of pressure and density

$$\frac{p}{p_0} = \left(\frac{\rho}{\rho_0}\right)^{\gamma}. \tag{2.26}$$

The equation is also referred to as the gamma pressure law when presented as

$$p(\rho) = k\rho^{\gamma}. \tag{2.27}$$

In this equation, the reference states are expressed by the constant k. It may be shown that this constant depends on the entropy of the flow [31, 32].

The fluid speed of sound may be calculated from its definition

$$a^2 = \left(\frac{\partial p}{\partial \rho}\right)_s. \tag{2.28}$$

Inserting (2.27) and (2.11), $a(T)$ is found as

$$\begin{aligned} a^2 &= \gamma k \rho^{\gamma-1} \\ &= \gamma \frac{p}{\rho} \\ &= \gamma RT. \end{aligned} \tag{2.29}$$

At the physically unrealisable limit $\gamma = 1$, the conservation equations (2.19)-(2.20) together with the pressure law (2.27) are sometimes denoted the isothermal Euler equations. The equations are then additionally based on the assumption of constant fluid temperature, and thus the equation of state (2.11) simplifies to

$$p(\rho) = a^2\rho, \tag{2.30}$$

where $a = \sqrt{RT}$ is the constant speed of sound in the fluid.

An isothermal *and* isentropic fluid flow is not physically viable as isentropic flow calls for changes in temperature and opposite. However, the resulting equations may give an approximate description of gases which have such a large heat capacity that the changes in fluid temperature are marginal. Relevant applications are for example astrophysical problems and

flow in immersed tubes where the fluid temperature is nearly constant [31]. Temperature changes may in some cases also be neglected for flows of low speed where the heat content of the flow is large compared to the kinetic energy of the fluid. At these conditions the temperature increase may be neglected even in the case when the entire kinetic energy is transformed into heat [32].

2.2. The Drift-Flux Model

2.2.1. Conservation equations

The drift-flux model is commonly used to describe two-phase flows where the gas and the liquid phases are mixed. The model is based on the assumption of equal pressure

$$p_{\mathrm{g}} = p_{\ell} = p, \tag{2.31}$$

which is a reasonable simplification for a mixed flow regime [18].

In the present work, the flow is assumed to be isentropic or isothermal. Thus, the applied conservation law consists of two equations describing mass conservation for the liquid and gas phases (2.32) and one equation describing conservation of total momentum (2.33) [18]. The latter equation is derived by summing the two equations which describe conservation of momentum for each of the fluid phases and applying the equal pressure assumption (2.31).

$$\frac{\partial m_k}{\partial t} + \frac{\partial I_k}{\partial x} = 0,\ k = \mathrm{g}, \ell, \tag{2.32}$$

$$\frac{\partial}{\partial t}\left(I_{\mathrm{g}} + I_{\ell}\right) + \frac{\partial}{\partial x}\left(I_{\mathrm{g}} v_{\mathrm{g}} + I_{\ell} v_{\ell} + p\right) = -F_{\mathrm{w}}. \tag{2.33}$$

Here, m_k is the volumetric mass of phase k

$$m_k = \rho_k \alpha_k, \tag{2.34}$$

I_k is the volumetric momentum of phase k

$$I_k = \rho_k \alpha_k v_k, \tag{2.35}$$

ρ_k and v_k are the mass density and velocity of phase k, respectively, and α_k is the volume fraction which satisfies the equation

$$\alpha_{\ell} + \alpha_{\mathrm{g}} = 1. \tag{2.36}$$

F_{w} is a momentum source term describing the effect of wall friction.

2.2.2. Thermodynamic submodel

We consider isentropic or isothermal flows, thus pressure may be expressed as a function of density alone

$$p = p\left(\rho_\ell\right) = p\left(\rho_\mathrm{g}\right). \tag{2.37}$$

The selected thermodynamic submodel is a locally linearisation of a general thermodynamic model

$$\rho_k = \rho_{k,0} + \frac{p_k - p_{k,0}}{c_k^2}, \tag{2.38}$$

where the fluid speed of sound is calculated as

$$c_k^2 \equiv \frac{\partial p}{\partial \rho_k}\left(p_{k,0}\right) \tag{2.39}$$

and $p_{k,0}$ is defined as

$$p_{k,0} = p\left(\rho_{k,0}\right). \tag{2.40}$$

For convenience, the model is implemented in the form

$$p_k = c_k^2\left(\rho_k - \rho_k^0\right), \tag{2.41}$$

where the variable ρ_k^0 is defined by

$$\rho_k^0 = \rho_{k,0} - \frac{p_{k,0}}{c_k^2} \tag{2.42}$$

2.2.3. Hydrodynamic submodel

In order to close the set of equations, an equation relating the liquid and gas velocities is needed. The equation, denoted the slip relation, is defined as $\Phi = v_\mathrm{g} - v_\ell$, and in general it is presented on the form [19]

$$v_\mathrm{g} - v_\ell = \Phi\left(m_\mathrm{g}, m_\ell, v_\mathrm{g}\right). \tag{2.43}$$

In the present work, two different slip relations were considered; the no slip relation

$$\Phi = 0, \tag{2.44}$$

and the Zuber-Findlay slip relation.

$$\Phi = \frac{\left(K-1\right)v_\mathrm{g} + S}{K\alpha_\ell}. \tag{2.45}$$

The Zuber-Findlay slip relation is valid for slug and bubbly flow regimes, and K and S are flow dependent constants [19].

"An ocean traveller has even more vividly the impression that the ocean is made of waves than that it is made of water."

Sir Arthur Stanley Eddington

3 Network Theory and the Generalized Riemann Problem

Network theory for fluid flow in junctions is based on the formulation of a generalized Riemann problem [25]. The solution of the problem is found by considering the solutions of standard Riemann problems. Hence we will begin by considering the standard Riemann problem. In particular we will show its solutions for the isentropic and isothermal Euler equations.

The derivation also shows the need for entropy conditions in order to identify the physically sound solutions. The formal description of such conditions are presented in Chapter 3.2 along with a condition particularly derived for the isothermal Euler equations.

Based on the solutions of the standard Riemann problem and on the outlined entropy conditions, the network theory for the isentropic and isothermal Euler equations is presented in Chapter 3.3.

3.1. The Standard Riemann Problem

The Riemann problem is named after Bernhard Riemann [51, Sec. 1.5.4]. It consists of a conservation law for N conserved variables

$$\frac{\partial \boldsymbol{U}}{\partial t} + \frac{\partial \boldsymbol{f}(\boldsymbol{U})}{\partial x} = 0, \tag{3.1}$$

together with piecewise constant initial data having a single discontinuity, for instance at $x = 0$

$$\boldsymbol{U}(x,0) = \begin{cases} \boldsymbol{U}_{\mathrm{L}} & \text{if } x < 0, \\ \boldsymbol{U}_{\mathrm{R}} & \text{if } x > 0. \end{cases} \tag{3.2}$$

Here

$$\boldsymbol{U} = \begin{bmatrix} u_1 \\ u_2 \\ \vdots \\ u_N \end{bmatrix} \tag{3.3}$$

is the vector of conserved variables, and

$$\boldsymbol{f}(\boldsymbol{U}) = \begin{bmatrix} f_1(u_1, u_2, ..., u_N) \\ f_2(u_1, u_2, ..., u_N) \\ \vdots \\ f_N(u_1, u_2, ..., u_N) \end{bmatrix} \tag{3.4}$$

is the vector of flux functions [53].

For a hyperbolic conservation law, the solution to the standard Riemann problem is a function of $\xi = x/t$ alone and it consists of a finite set of waves that move with constant speeds away from the origin [31, Sec. 1.2.1]. A conservation law is hyperbolic if it has N real eigenvalues, where N is the number of conserved variables. If the eigenvalues additionally are distinct, the system is denoted as strictly hyperbolic [26, Ch. 5].

The eigenvalues are calculated from the Jacobian matrix of the flux function

$$\boldsymbol{A} = \frac{\partial \boldsymbol{f}}{\partial \boldsymbol{U}}. \tag{3.5}$$

The derivatives are valid for smooth solutions, and at this condition it is possible to reformulate the conservation law (3.1)

$$\frac{\partial \boldsymbol{U}}{\partial t} + \boldsymbol{A}\frac{\partial \boldsymbol{U}}{\partial x} = 0. \tag{3.6}$$

The eigenvalues, λ_j, and eigenvectors, $\boldsymbol{r}_j$, are defined to fulfil

$$(\boldsymbol{A}(\boldsymbol{U}) - \lambda_j \boldsymbol{I})\,\boldsymbol{r}_j = 0. \tag{3.7}$$

The eigenvalues, λ_j are thus solutions of the characteristic equation

$$|\boldsymbol{A} - \lambda_j \boldsymbol{I}| = 0. \tag{3.8}$$

For a strictly hyperbolic conservation law, there are N distinct $(\lambda_j - r_j)$ pairs. Each pair is said to belong to the j-th family. If a family is genuinely nonlinear, that is

$$\nabla \lambda_j (\boldsymbol{U}) \cdot \boldsymbol{r}_j (\boldsymbol{U}) \neq 0 \tag{3.9}$$

for all $\boldsymbol{U}$, or a family is linearly degenerate such that

$$\nabla \lambda_j (\boldsymbol{U}) \cdot \boldsymbol{r}_j (\boldsymbol{U}) \equiv 0 \tag{3.10}$$

for all $\boldsymbol{U}$, then the solution will contain one wave which is related to the family. Consequently, if all families of a conservation law are either genuinely nonlinear or linearly degenerate, the solution consists of N waves. For conservation laws where one or more families are neither genuinely nonlinear nor linearly degenerate, the structure of one wave per family is not guaranteed, and hence the overall solution may be far more complex [31, Sec. 13.8.4].

Waves of genuinely non-linear families may be rarefaction waves or shock waves. Rarefaction waves are smooth solutions, that is $u_j \; \forall j \in [1, .., N]$ are continuous functions of $\xi = {}^{x}/_{t}$. Such waves thus satisfy the conservation law as written in (3.1). Shock waves are moving discontinuities which do not satisfy (3.1) in the classical sense. A shock is however an admissible solution to a conservation law if it is stated on integral form.

Among the different integral forms developed, the weak formulation is the most convenient to work with mathematically [31]. The approach makes use of test functions, ϕ, which are continuously differentiable and have compact support. That is, ϕ is in the function space C_0^1 and it is "identically zero outside of some bounded region of the x-t plane" [31, p.215], respectively.

In the weak formulation, the conservation law of a one dimensional problem is multiplied by the test function, ϕ, and integrated in space and time

$$\int_0^\infty \int_{-\infty}^\infty \left[\frac{\partial \boldsymbol{U}}{\partial t} + \frac{\partial \boldsymbol{f}(\boldsymbol{U})}{\partial x} \right] \phi \, \mathrm{d}x \, \mathrm{d}t = 0. \tag{3.11}$$

We integrate by parts, keeping in mind that ϕ is equal to zero at $t = \infty$, and obtain [26, 31]

$$\begin{aligned} -\int_{-\infty}^\infty \boldsymbol{U}(x,0)\, \phi(x,0) \, \mathrm{d}x - \int_{-\infty}^\infty \int_0^\infty \boldsymbol{U} \frac{\partial \phi}{\partial t} \, \mathrm{d}t \, \mathrm{d}x \\ - \int_0^\infty \int_{-\infty}^\infty \boldsymbol{f}(\boldsymbol{U}) \frac{\partial \phi}{\partial x} \, \mathrm{d}x \, \mathrm{d}t = 0, \end{aligned} \tag{3.12}$$

or

$$\int_{-\infty}^{\infty} \boldsymbol{U}(x,0)\,\phi(x,0)\,\mathrm{d}x + \int_{0}^{\infty}\int_{-\infty}^{\infty}\left(\boldsymbol{U}\frac{\partial\phi}{\partial t} + \boldsymbol{f}(\boldsymbol{U})\frac{\partial\phi}{\partial x}\right)\mathrm{d}x\,\mathrm{d}t = 0. \quad (3.13)$$

Solutions to the Riemann problems of the isentropic and isothermal Euler equations consist of two wave families, both genuinely non-linear. The two states of the initial problem (3.2) are connected by two waves which are either rarefaction or shock waves. For the Euler equations and the drift-flux model with no slip, the second family is linearly degenerate and the corresponding wave is a contact discontinuity. The properties of such waves are out of the scope of the present work. This is described for instance by Holden and Risebro [26] and Toro [53].

In the following, the eigenvalues and eigenvectors of the isentropic and isothermal Euler equations will be derived. The derivation of equations for rarefaction and shock waves will be described in Chapter 3.1.2 and 3.1.3, respectively.

3.1.1. The isentropic/isothermal Euler equations: eigenvalues and eigenvectors

The Jacobi matrix of the isentropic Euler equations (2.19)- (2.20) is

$$\boldsymbol{A} = \begin{bmatrix} 0 & 1 \\ -\frac{(\rho v)^2}{\rho^2} + p'(\rho) & \frac{2(\rho v)}{\rho} \end{bmatrix} \quad (3.14)$$

The characteristic equation (3.8) is thus

$$\begin{vmatrix} -\lambda_j & 1 \\ -\frac{(\rho v)^2}{\rho^2} + p'(\rho) & \frac{2(\rho v)}{\rho} - \lambda_j \end{vmatrix} = 0, \quad (3.15)$$

which may be simplified to

$$\lambda_j^2 - \frac{2(\rho v)}{\rho}\lambda_j + \left(\frac{(\rho v)^2}{\rho^2} - p'(\rho)\right) = 0. \quad (3.16)$$

The solutions of the quadratic equation are

$$\begin{aligned} \lambda_j =& \frac{1}{2}\left(\frac{2(\rho v)}{\rho} \pm \sqrt{\left(-\frac{2(\rho v)}{\rho}\right)^2 - 4\left(\frac{(\rho v)^2}{\rho^2} - p'(\rho)\right)}\right) \\ =& \frac{(\rho v)}{\rho} \pm \sqrt{p'(\rho)}. \end{aligned} \quad (3.17)$$

The eigenvalues may be ordered

$$\lambda_1 = v - \sqrt{p'(\rho)} < \lambda_2 = v + \sqrt{p'(\rho)}, \tag{3.18}$$

and we may use the family notation

$$\lambda_j = v + (-1)^j \sqrt{p'(\rho)}. \tag{3.19}$$

Comparing Equation (3.18) to Equation (3.19) it is clear that there are two wave families, that is $j \in \{1, 2\}$. In addition it may be noted that the first family has the smallest eigenvalue.

The eigenvectors are found by solving (3.7)

$$\begin{bmatrix} -\lambda_j & 1 \\ -\frac{(\rho v)^2}{\rho^2} + p'(\rho) & \frac{2(\rho v)}{\rho} - \lambda_j \end{bmatrix} \boldsymbol{r}_j = 0, \tag{3.20}$$

which gives the solutions

$$\boldsymbol{r}_j = \begin{bmatrix} 1 \\ \lambda_j \end{bmatrix}, \quad j = 1, 2. \tag{3.21}$$

3.1.2. The isentropic/isothermal Euler equations: rarefaction waves

As stated earlier, rarefaction waves are smooth waves, which depend only on $\xi = x/t$ [1]

$$\boldsymbol{U}(x, t) = \boldsymbol{w}(x/t) = \boldsymbol{w}(\xi). \tag{3.22}$$

Entering $\boldsymbol{w}(\xi)$ into the conservation law (3.1), the following relations may be derived

$$\begin{aligned} \frac{\partial \boldsymbol{w}(\xi)}{\partial t} + \frac{\partial \boldsymbol{f}(\boldsymbol{w}(\xi))}{\partial x} &= 0, \\ -\frac{x}{t^2}\frac{\mathrm{d}\boldsymbol{w}}{\mathrm{d}\xi} + \frac{1}{t}\boldsymbol{A}(\boldsymbol{w})\frac{\mathrm{d}\boldsymbol{w}}{\mathrm{d}\xi} &= 0, \\ (\boldsymbol{A}(\boldsymbol{w}) - \xi \boldsymbol{I})\frac{\mathrm{d}\boldsymbol{w}}{\mathrm{d}\xi} &= 0. \end{aligned} \tag{3.23}$$

[1] The derivation of the wave equations found in this chapter relies heavily on Holden and Risebro [26, Ch. 5]

Comparing Equation (3.23) and Equation (3.7), we see that

$$\frac{\mathrm{d}\boldsymbol{w}}{\mathrm{d}\xi} = \boldsymbol{r}_j\left(\boldsymbol{w}\left(\xi\right)\right), \tag{3.24}$$

$$\xi = \frac{x}{t} = \lambda_j. \tag{3.25}$$

This has two implications. First, from Equation (3.25) we observe that as x, and thus ξ, increases from the left to the right state, the eigenvalues, λ_j, must also increase. Another consequence of Equation (3.25) is that

$$\boldsymbol{w}\left(\lambda_j\left(\boldsymbol{U}_{\mathcal{L}}\right)\right) = \boldsymbol{U}_{\mathcal{L}}, \tag{3.26}$$

$$\boldsymbol{w}\left(\lambda_j\left(\boldsymbol{U}_{\mathcal{R}}\right)\right) = \boldsymbol{U}_{\mathcal{R}}. \tag{3.27}$$

Second, Equation (3.25) may be used to normalise the eigenvectors. Using the chain rule, the fact that λ_j is a function of $\boldsymbol{w}$, and the result in Equation (3.24) we have

$$\begin{aligned}\frac{\mathrm{d}}{\mathrm{d}\xi}\left(\lambda_j\right) =& \nabla\lambda_j\left(\boldsymbol{w}\right)\frac{\mathrm{d}\boldsymbol{w}}{\mathrm{d}\xi},\\ =& \nabla\lambda_j\left(\boldsymbol{w}\right)\boldsymbol{r}_j.\end{aligned} \tag{3.28}$$

Inserting $\lambda_j = \xi$ into Equation (3.28) we see that the derivative in this equation should be equal to 1

$$\frac{\mathrm{d}}{\mathrm{d}\xi}\left(\lambda_j\right) = \frac{\mathrm{d}}{\mathrm{d}\xi}\left(\xi\right) = 1. \tag{3.29}$$

Thus, (3.28) and (3.29) show that the wave-family is genuinely non-linear as stated in (3.9).

The normalisation is important when $\boldsymbol{w}$ is sought as a function of ξ. Inserting the expressions for eigenvalues (3.17) and eigenvectors (3.21) of the isentropic Euler equations, Equation (3.28) becomes

$$\begin{aligned}\nabla\lambda_j\left(\boldsymbol{w}\right)\boldsymbol{r}_j =& \nabla\left(\frac{\left(\rho v\right)}{\rho} + \left(-1\right)^j\sqrt{p'\left(\rho\right)}\right)\begin{bmatrix}1\\ \left(\frac{\left(\rho v\right)}{\rho} + \left(-1\right)^j\sqrt{p'\left(\rho\right)}\right)\end{bmatrix}\\ =& \left(-1\right)^j\left(\frac{p''\left(\rho\right)}{2\sqrt{p'\left(\rho\right)}} + \frac{\sqrt{p'\left(\rho\right)}}{\rho}\right).\end{aligned} \tag{3.30}$$

Hence, the derivative of $\boldsymbol{w}$ (3.24) may be written as

$$\frac{\mathrm{d}\boldsymbol{w}}{\mathrm{d}\xi} = \begin{bmatrix}\frac{\mathrm{d}\rho}{\mathrm{d}\xi}\\ \frac{\mathrm{d}\left(\rho v\right)}{\mathrm{d}\xi}\end{bmatrix} = \frac{1}{\left(-1\right)^j\left(\frac{p''\left(\rho\right)}{2\sqrt{p'\left(\rho\right)}} + \frac{\sqrt{p'\left(\rho\right)}}{\rho}\right)}\begin{bmatrix}1\\ \lambda_j\end{bmatrix}. \tag{3.31}$$

It is also possible to express wave curves in terms of the relation between the conserved variables. For the isentropic Euler equations, density, ρ, and the mass flux, (ρv) are conserved. The relation between these variables is found from Equation (3.31)

$$\frac{\mathrm{d}(\rho v)}{\mathrm{d}\rho} = \lambda_j = \frac{(\rho v)}{\rho} + (-1)^j \sqrt{p'(\rho)}. \tag{3.32}$$

As

$$\frac{\mathrm{d}(\rho v)}{\mathrm{d}\rho} - \frac{(\rho v)}{\rho} = \rho \frac{\mathrm{d}}{\mathrm{d}\rho}\left(\frac{(\rho v)}{\rho}\right), \tag{3.33}$$

separation of variables yields

$$\frac{\mathrm{d}}{\mathrm{d}\rho}\left(\frac{(\rho v)}{\rho}\right) = \frac{\mathrm{d}v}{\mathrm{d}\rho} = \frac{1}{\rho}(-1)^j \sqrt{p'(\rho)}. \tag{3.34}$$

Equation (3.34) may then be integrated from left state, $\mathcal{L}$, to the right state, $\mathcal{R}$, of the wave

$$\int_{\rho_\mathcal{L}}^{\rho_\mathcal{R}} \frac{\mathrm{d}v}{\mathrm{d}\rho}\,\mathrm{d}\rho = \int_{\rho_\mathcal{L}}^{\rho_\mathcal{R}} (-1)^j \frac{\sqrt{p'(\rho)}}{\rho}\,\mathrm{d}\rho. \tag{3.35}$$

The left hand side of this equation may be written as

$$\int_{\rho_\mathcal{L}}^{\rho_\mathcal{R}} \frac{\mathrm{d}v}{\mathrm{d}\rho}\,\mathrm{d}\rho = [v]_{\rho_\mathcal{L}}^{\rho_\mathcal{R}} = v_\mathcal{R} - v_\mathcal{L}. \tag{3.36}$$

In the special case when the isothermal pressure law (2.30) is applied, integration of the right hand side of (3.35) gives

$$v_\mathcal{R} - v_\mathcal{L} = \int_{\rho_\mathcal{L}}^{\rho_\mathcal{R}} (-1)^j a \frac{1}{\rho}\,\mathrm{d}\rho = (-1)^j a \left[\ln(\rho)\right]_{\rho_\mathcal{L}}^{\rho_\mathcal{R}}, \tag{3.37}$$

that is

$$v_\mathcal{R} - v_\mathcal{L} = (-1)^j a \ln\left(\frac{\rho_\mathcal{R}}{\rho_\mathcal{L}}\right). \tag{3.38}$$

In the general case, the γ-pressure law (2.27) is applied with $\gamma > 1$

$$\begin{aligned} v_\mathcal{R} - v_\mathcal{L} &= \int_{\rho_\mathcal{L}}^{\rho_\mathcal{R}} (-1)^j \sqrt{\gamma k} \frac{\sqrt{\rho^{\gamma-1}}}{\rho}\,\mathrm{d}\rho, \\ &= (-1)^j \sqrt{\gamma k} \int_{\rho_\mathcal{L}}^{\rho_\mathcal{R}} \rho^{\frac{\gamma-3}{2}}\,\mathrm{d}\rho, \\ &= (-1)^j \sqrt{\gamma k} \left[\frac{2}{\gamma-1}\rho^{\frac{\gamma-1}{2}}\right]_{\rho_\mathcal{L}}^{\rho_\mathcal{R}}. \end{aligned} \tag{3.39}$$

Or, simplified

$$v_{\mathcal{R}} - v_{\mathcal{L}} = (-1)^j \frac{2\sqrt{\gamma k}}{\gamma - 1} \left(\rho_{\mathcal{R}}^{\frac{\gamma-1}{2}} - \rho_{\mathcal{L}}^{\frac{\gamma-1}{2}} \right). \tag{3.40}$$

As stated earlier, due to (3.25) the following must be fulfilled

$$\lambda_j \left(\boldsymbol{U}_{\mathcal{R}} \right) \geq \lambda_j \left(\boldsymbol{U}_{\mathcal{L}} \right). \tag{3.41}$$

For the isothermal equations, the wave equation (3.38), the expressions for the eigenvalues (3.18) and the pressure law (2.30) may be inserted into (3.41) to give

$$\begin{aligned} v_{\mathcal{R}} + (-1)^j a = v_{\mathcal{L}} + (-1)^j a \ln \left(\frac{\rho_{\mathcal{R}}}{\rho_{\mathcal{L}}} \right) + (-1)^j a \geq & v_{\mathcal{L}} + (-1)^j a, \\ (-1)^j a \ln \left(\frac{\rho_{\mathcal{R}}}{\rho_{\mathcal{L}}} \right) \geq & 0. \end{aligned} \tag{3.42}$$

For a wave of the first family, $j = 1$, this implies that $\rho_{\mathcal{R}} \leq \rho_{\mathcal{L}}$. If the wave is of the second family, $j = 2$, $\rho_{\mathcal{R}} \geq \rho_{\mathcal{L}}$.

If the isentropic equations are considered with $\gamma > 1$, the corresponding wave equation (3.40) and pressure law (2.27), together with the expressions for the eigenvalues (3.18) may be inserted into the inequality (3.41) to give following criterion

$$\begin{aligned} v_{\mathcal{L}} + (-1)^j \frac{2\sqrt{\gamma k}}{\gamma - 1} \left(\rho_{\mathcal{R}}^{\frac{\gamma-1}{2}} - \rho_{\mathcal{L}}^{\frac{\gamma-1}{2}} \right) + (-1)^j \sqrt{\gamma k \rho_{\mathcal{R}}^{(\gamma-1)}} & \\ \geq \; v_{\mathcal{L}} + (-1)^j \sqrt{\gamma k \rho_{\mathcal{L}}^{(\gamma-1)}}, & \end{aligned} \tag{3.43}$$

or,

$$(-1)^j \frac{\gamma + 1}{\gamma - 1} \sqrt{\gamma k} \left(\rho_{\mathcal{R}}^{\frac{\gamma-1}{2}} - \rho_{\mathcal{L}}^{\frac{\gamma-1}{2}} \right) \geq \; 0. \tag{3.44}$$

This is seen to give the same selection criterion for rarefaction waves as found from Equation (3.42); a wave of the first family, $j = 1$, is a rarefaction wave if $\rho_{\mathcal{R}} \leq \rho_{\mathcal{L}}$. If the wave is of the second family, $j = 2$, it is a rarefaction wave if $\rho_{\mathcal{R}} \geq \rho_{\mathcal{L}}$.

3.1.3. The isentropic/isothermal Euler equations: shock waves

The expressions for shock waves are derived from the Rankine-Hugoniot condition [26, Ch. 5]

$$s \left(\boldsymbol{U}_{\mathcal{R}} - \boldsymbol{U}_{\mathcal{L}} \right) = \boldsymbol{f} \left(\boldsymbol{U}_{\mathcal{R}} \right) - \boldsymbol{f} \left(\boldsymbol{U}_{\mathcal{L}} \right), \tag{3.45}$$

where s is the wave velocity. The condition, which is derived by applying the weak formulation (3.11), states when $\boldsymbol{U}$ is conserved across a discontinuity [26, Eq. (1.19)].

Applying the condition on the isentropic Euler equations (2.19)- (2.20), we obtain a system of two equations

$$s\left(\rho_{\mathcal{R}}-\rho_{\mathcal{L}}\right)=(\rho v)_{\mathcal{R}}-(\rho v)_{\mathcal{L}}\,, \tag{3.46}$$

$$s\left((\rho v)_{\mathcal{R}}-(\rho v)_{\mathcal{L}}\right)=\left(\frac{(\rho v)_{\mathcal{R}}^{2}}{\rho_{\mathcal{R}}}+p\left(\rho_{\mathcal{R}}\right)\right)-\left(\frac{(\rho v)_{\mathcal{L}}^{2}}{\rho_{\mathcal{L}}}+p\left(\rho_{\mathcal{L}}\right)\right). \tag{3.47}$$

Inserting (3.46) into (3.47), we obtain the following quadratic equation

$$\begin{aligned}(\rho v)_{\mathcal{R}}^{2}-2\frac{\rho_{\mathcal{R}}}{\rho_{\mathcal{L}}}(\rho v)_{\mathcal{L}}(\rho v)_{\mathcal{R}}+\frac{\rho_{\mathcal{R}}^{2}}{\rho_{\mathcal{L}}^{2}}(\rho v)_{\mathcal{L}}^{2}&\\ -\frac{\rho_{\mathcal{R}}}{\rho_{\mathcal{L}}}\left(\rho_{\mathcal{R}}-\rho_{\mathcal{L}}\right)\left(p\left(\rho_{\mathcal{R}}\right)-p\left(\rho_{\mathcal{L}}\right)\right)=0,&\end{aligned} \tag{3.48}$$

which has the solutions

$$(\rho v)_{\mathcal{R}}=\frac{\rho_{\mathcal{R}}}{\rho_{\mathcal{L}}}(\rho v)_{\mathcal{L}}\pm\sqrt{\frac{\rho_{\mathcal{R}}}{\rho_{\mathcal{L}}}\left(\rho_{\mathcal{R}}-\rho_{\mathcal{L}}\right)\left(p\left(\rho_{\mathcal{R}}\right)-p\left(\rho_{\mathcal{L}}\right)\right)}. \tag{3.49}$$

When the γ-pressure law (2.27) is applied, the velocities are related by

$$v_{\mathcal{R}}=v_{\mathcal{L}}\pm\sqrt{\frac{k\left(\rho_{\mathcal{R}}-\rho_{\mathcal{L}}\right)\left(\rho_{\mathcal{R}}^{\gamma}-\rho_{\mathcal{L}}^{\gamma}\right)}{\rho_{\mathcal{R}}\rho_{\mathcal{L}}}}. \tag{3.50}$$

For shock waves, additional conditions denoted the Lax entropy conditions must be satisfied if the wave is physically reasonable. For strictly hyperbolic systems like the isentropic and isothermal Euler equations, physical shock waves of family j are characterised by [26, Ch. 5]

$$\lambda_{j}\left(\boldsymbol{U}_{\mathcal{R}}\right)<s<\lambda_{j}\left(\boldsymbol{U}_{\mathcal{L}}\right). \tag{3.51}$$

The shock wave velocity may be found from Equation (3.46)

$$\begin{aligned}s=&\frac{(\rho v)_{\mathcal{R}}-(\rho v)_{\mathcal{L}}}{\rho_{\mathcal{R}}-\rho_{\mathcal{L}}}\\ =&\frac{\left(\rho_{\mathcal{R}}-\rho_{\mathcal{L}}\right)(\rho v)_{\mathcal{L}}\pm\rho_{\mathcal{L}}\sqrt{\frac{\rho_{\mathcal{R}}}{\rho_{\mathcal{L}}}\left(\rho_{\mathcal{R}}-\rho_{\mathcal{L}}\right)\left(p\left(\rho_{\mathcal{R}}\right)-p\left(\rho_{\mathcal{L}}\right)\right)}}{\left(\rho_{\mathcal{R}}-\rho_{\mathcal{L}}\right)\rho_{\mathcal{L}}}.\end{aligned} \tag{3.52}$$

The wave speeds are thus

$$s = v_{\mathcal{L}} \pm \frac{1}{(\rho_{\mathcal{R}} - \rho_{\mathcal{L}})} \sqrt{\frac{\rho_{\mathcal{R}}}{\rho_{\mathcal{L}}} k \left(\rho_{\mathcal{R}} - \rho_{\mathcal{L}}\right) \left(\rho_{\mathcal{R}}^{\gamma} - \rho_{\mathcal{L}}^{\gamma}\right)}, \tag{3.53}$$

when the γ-pressure law is inserted.

We begin by considering a shock wave of the first family. The condition for which the wave is physically sound (3.51) is then

$$v_{\mathcal{R}} - \sqrt{k\gamma\rho_{\mathcal{R}}^{\gamma-1}} < v_{\mathcal{L}} \pm \frac{1}{(\rho_{\mathcal{R}} - \rho_{\mathcal{L}})} \sqrt{\frac{\rho_{\mathcal{R}}}{\rho_{\mathcal{L}}} k \left(\rho_{\mathcal{R}} - \rho_{\mathcal{L}}\right) \left(\rho_{\mathcal{R}}^{\gamma} - \rho_{\mathcal{L}}^{\gamma}\right)} < v_{\mathcal{L}} - \sqrt{k\gamma\rho_{\mathcal{L}}^{\gamma-1}}. \tag{3.54}$$

The last inequality has one solution only

$$s_1 = v_{\mathcal{L}} - \frac{1}{(\rho_{\mathcal{R}} - \rho_{\mathcal{L}})} \sqrt{\frac{\rho_{\mathcal{R}}}{\rho_{\mathcal{L}}} k \left(\rho_{\mathcal{R}} - \rho_{\mathcal{L}}\right) \left(\rho_{\mathcal{R}}^{\gamma} - \rho_{\mathcal{L}}^{\gamma}\right)}, \quad \rho_{\mathcal{R}} > \rho_{\mathcal{L}}. \tag{3.55}$$

The corresponding equation relating the velocities is

$$v_{\mathcal{R}} = v_{\mathcal{L}} - \sqrt{\frac{k \left(\rho_{\mathcal{R}} - \rho_{\mathcal{L}}\right) \left(\rho_{\mathcal{R}}^{\gamma} - \rho_{\mathcal{L}}^{\gamma}\right)}{\rho_{\mathcal{R}} \rho_{\mathcal{L}}}}. \tag{3.56}$$

Detailed calculations that show the existence of only one solution to the inequality is given in Appendix A. Calculations for the second family is shown there as well.

For shock waves of the second family, the condition is

$$v_{\mathcal{R}} + \sqrt{k\gamma\rho_{\mathcal{R}}^{\gamma-1}} < v_{\mathcal{L}} \pm \frac{1}{(\rho_{\mathcal{R}} - \rho_{\mathcal{L}})} \sqrt{\frac{\rho_{\mathcal{R}}}{\rho_{\mathcal{L}}} k \left(\rho_{\mathcal{R}} - \rho_{\mathcal{L}}\right) \left(\rho_{\mathcal{R}}^{\gamma} - \rho_{\mathcal{L}}^{\gamma}\right)} < v_{\mathcal{L}} + \sqrt{k\gamma\rho_{\mathcal{L}}^{\gamma-1}}, \tag{3.57}$$

where the only solution of the first inequality is

$$s_2 = v_{\mathcal{L}} - \frac{1}{(\rho_{\mathcal{R}} - \rho_{\mathcal{L}})} \sqrt{\frac{\rho_{\mathcal{R}}}{\rho_{\mathcal{L}}} k \left(\rho_{\mathcal{R}} - \rho_{\mathcal{L}}\right) \left(\rho_{\mathcal{R}}^{\gamma} - \rho_{\mathcal{L}}^{\gamma}\right)}, \quad \rho_{\mathcal{R}} < \rho_{\mathcal{L}}. \tag{3.58}$$

The equation relating the velocities is thus

$$v_{\mathcal{R}} = v_{\mathcal{L}} - \sqrt{\frac{k \left(\rho_{\mathcal{R}} - \rho_{\mathcal{L}}\right) \left(\rho_{\mathcal{R}}^{\gamma} - \rho_{\mathcal{L}}^{\gamma}\right)}{\rho_{\mathcal{R}} \rho_{\mathcal{L}}}}. \tag{3.59}$$

To summarise, we have the following equations for shock wave speeds and velocity

$$s_j = v_{\mathcal{L}} - \frac{1}{(\rho_{\mathcal{R}} - \rho_{\mathcal{L}})}\sqrt{\frac{\rho_{\mathcal{R}}}{\rho_{\mathcal{L}}} k\,(\rho_{\mathcal{R}} - \rho_{\mathcal{L}})\,(\rho_{\mathcal{R}}^{\gamma} - \rho_{\mathcal{L}}^{\gamma})}, \quad (-1)^j\,(\rho_{\mathcal{R}} - \rho_{\mathcal{L}}) < 0, \tag{3.60}$$

$$v_{\mathcal{R}} = v_{\mathcal{L}} - \sqrt{\frac{k\,(\rho_{\mathcal{R}} - \rho_{\mathcal{L}})\,(\rho_{\mathcal{R}}^{\gamma} - \rho_{\mathcal{L}}^{\gamma})}{\rho_{\mathcal{R}}\rho_{\mathcal{L}}}}, \quad (-1)^j\,(\rho_{\mathcal{R}} - \rho_{\mathcal{L}}) < 0. \tag{3.61}$$

Here we have used the family notation, with $j = \{1, 2\}$ for waves of the first and second family, respectively.

Equations may be derived specifically for the isothermal Euler equations by inserting $\gamma = 1$ and $k = a^2$ into the shock speed equations (3.60) and the velocity equations (3.61)

$$s_j = v_{\mathcal{L}} + (-1)^j\, a\sqrt{\frac{\rho_{\mathcal{R}}}{\rho_{\mathcal{L}}}}, \quad (-1)^j\,(\rho_{\mathcal{R}} - \rho_{\mathcal{L}}) < 0, \tag{3.62}$$

$$v_{\mathcal{R}} = v_{\mathcal{L}} + (-1)^j\, a\left(\sqrt{\frac{\rho_{\mathcal{R}}}{\rho_{\mathcal{L}}}} - \sqrt{\frac{\rho_{\mathcal{L}}}{\rho_{\mathcal{R}}}}\right), \quad (-1)^j\,(\rho_{\mathcal{R}} - \rho_{\mathcal{L}}) < 0. \tag{3.63}$$

The rarefaction- and shock wave equations, (3.38) and (3.63), for the isothermal Euler equations are shown in Figure 3.1. The curves show $v_{\mathcal{R}}$ as a function of $\rho_{\mathcal{R}}$ for a selected left state $(\rho_{\mathcal{L}}, v_{\mathcal{L}})$.

3.1.4. The solution to the Riemann problem

This is a very brief description of the solution to the Riemann problem for the isothermal Euler equations. For more comprehensive presentations, see for example Holden and Risebro [26], LeVeque [31] and Toro [53].

Identifying the waves connecting the two states of the Riemann problem

As we are considering the isothermal Euler equations, the solution of the Riemann problem consists of two waves. An example of such a solution is showed in Figure 3.2, where it is presented in the x, t-plane. The solution is a shock wave of the first family and a rarefaction wave of the second family. The order of the wave family numbers is not arbitrary in such a solution. It will always be increasing as we move from left to right. The figure also indicates the inverted slopes, $\frac{\mathrm{d}x}{\mathrm{d}t}$, for the shock wave and each

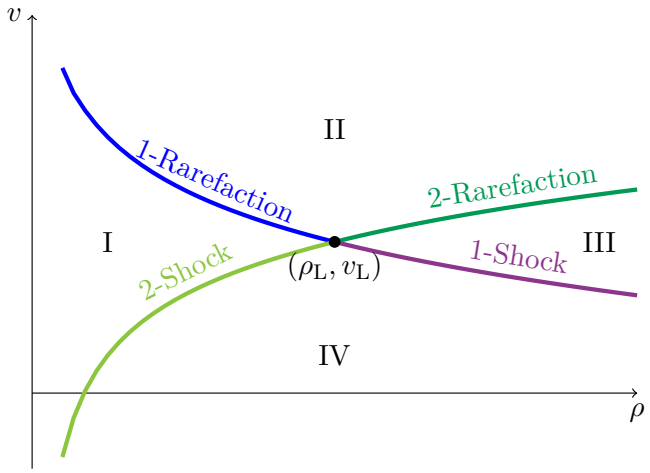

Figure 3.1.: Wave curves for the isothermal Euler equations

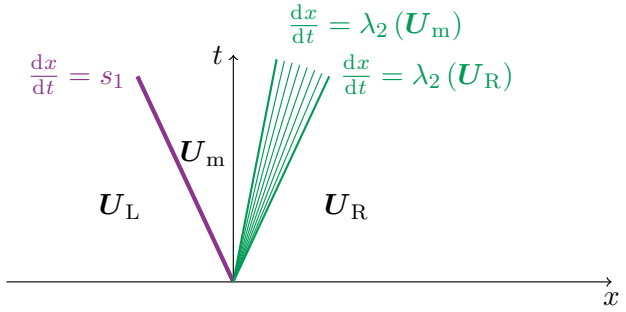

Figure 3.2.: Solution to the Riemann problem in the x-t plane

of the rarefaction wave fronts. For the shock wave, this is the shock wave velocity (3.45). For the rarefaction wave, Equation (3.25) is used.

Based on the composition of waves found in Figure 3.2, we may conclude that the right hand state of this Riemann problem, $\boldsymbol{U}_R$, is positioned in the region labelled III in Figure 3.1. This is shown in Figure 3.3, where the waves of the second family that are emerging from (ρ_m, v_m) are plotted in addition to the wave curves shown in Figure 3.1.

The intermediate state, $\boldsymbol{U}_m$, is found from the shock wave equation (3.63) written for the first family and the rarefaction wave equation (3.38) written

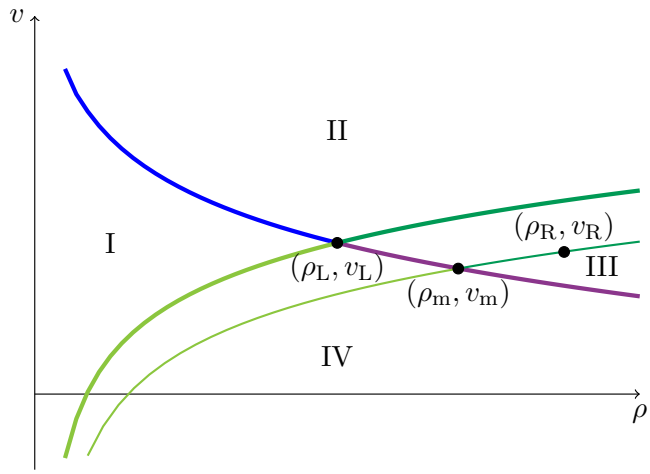

Figure 3.3.: The solution to a Riemann problem whose right hand state is positioned in region III

for the second family, forming the set of equations

$$v_m - v_L = -a\left(\sqrt{\frac{\rho_m}{\rho_L}} - \sqrt{\frac{\rho_L}{\rho_m}}\right), \tag{3.64}$$

$$v_R - v_m = a \ln\left(\frac{\rho_R}{\rho_m}\right). \tag{3.65}$$

In Equation (3.64), $v_{\mathcal{R}}$ and $\rho_{\mathcal{R}}$ of Equation (3.63) have been replaced by v_m and ρ_m, as $\boldsymbol{U}_m$ is the right state of the shock wave. j is set equal to 1 as the shock wave is of the first family. Similarly, v_m and ρ_m describes the left state in the rarefaction wave equation (3.65) and j is set equal to 2.

For (ρ_R, v_R) in each of the four regions in Figure 3.1, there is a given combination of waves linking the two states of the initial condition. These are shown in Table 3.1. The intermediate states for the regions I, II and IV are found in a similar manner as for region III, by using the correct wave family and left and right states in the Equations (3.38) and (3.63).

Expressing variables as function of time and position

So far we have derived expressions that relate the left and the right states of a rarefaction or a shock wave. In the following we would like to state the solutions as a function of time and space. The expression for $\boldsymbol{U}(x,t)$ is easily derived for a solution containing a shock wave of family j. The shock

Initial condition	1st wave family	2nd wave family
I	Rarefaction	Shock
II	Rarefaction	Rarefaction
III	Shock	Rarefaction
IV	Shock	Shock

Table 3.1.: Wave structures for solutions to the Riemann problem depending on initial conditions

wave is a single discontinuity between the left and right states, $\boldsymbol{U}_{\mathcal{L}}$ and $\boldsymbol{U}_{\mathcal{R}}$, which propagates with speed s_j (3.62)

$$\boldsymbol{U}(x,t) = \begin{cases} \boldsymbol{U}_{\mathcal{L}} & \text{for } x < s_j t, \\ \boldsymbol{U}_{\mathcal{R}} & \text{for } x \geq s_j t. \end{cases} \tag{3.66}$$

For a rarefaction wave we have the following solution [26, Eq. (5.23)]

$$\boldsymbol{U}(x,t) = \begin{cases} \boldsymbol{U}_{\mathcal{L}} & \text{for } x \leq \lambda_j(\boldsymbol{U}_{\mathcal{L}})\, t, \\ \boldsymbol{w}(x/t) & \text{for } \lambda_j(\boldsymbol{U}_{\mathcal{L}})\, t \leq x \leq \lambda_j(\boldsymbol{U}_{\mathcal{R}})\, t, \\ \boldsymbol{U}_{\mathcal{R}} & \text{for } x \geq \lambda_j(\boldsymbol{U}_{\mathcal{R}})\, t. \end{cases} \tag{3.67}$$

The similarity solution, $\boldsymbol{w}(x/t)$, is defined by Equation (3.31). Using the pressure law of the isothermal Euler equations (2.30), the differential equation becomes

$$\frac{\mathrm{d}\boldsymbol{w}}{\mathrm{d}\xi} = \begin{bmatrix} \frac{\mathrm{d}\rho}{\mathrm{d}\xi} \\ \frac{\mathrm{d}(\rho v)}{\mathrm{d}\xi} \end{bmatrix} = \frac{\rho}{(-1)^j\, a} \begin{bmatrix} 1 \\ \lambda_j \end{bmatrix}. \tag{3.68}$$

The density function may then be found from the first differential equation

$$\frac{\mathrm{d}\rho}{\mathrm{d}\xi} = (-1)^j \frac{\rho}{a}. \tag{3.69}$$

Integrating from the left state of the wave, we obtain

$$\begin{aligned} \int_{\rho_{\mathcal{L}}}^{\rho} \frac{1}{\rho}\, \mathrm{d}\rho &= \frac{(-1)^j}{a} \int_{\xi_{\mathcal{L}}}^{\xi} \mathrm{d}\xi, \\ \ln\left(\frac{\rho}{\rho_{\mathcal{L}}}\right) &= \frac{(-1)^j}{a} (\xi - \xi_{\mathcal{L}}). \end{aligned} \tag{3.70}$$

Solving for ρ and inserting the expression for $\xi_{\mathcal{L}}$ using Equation (3.25), we get

$$\rho = \rho_{\mathcal{L}} e^{\frac{(-1)^j}{a}\left(\frac{x}{t} - v_{\mathcal{L}}\right) - 1}. \tag{3.71}$$

The velocity may be found using Equation (3.38)

$$\begin{aligned} v =& v_{\mathcal{L}} + (-1)^j \, a \ln\left(\frac{\rho}{\rho_{\mathcal{L}}}\right) \\ =& \frac{x}{t} - (-1)^j \, a. \end{aligned} \tag{3.72}$$

Looking at the general expression for $\boldsymbol{U}$ in Equation (3.67), we may write $\rho\,(x,t)$ and $v\,(x,t)$ as

$$\rho\,(x,t) = \begin{cases} \rho_{\mathcal{L}} & \text{for } x \leq \left(v_{\mathcal{L}} + (-1)^j \, a\right) t, \\ \rho_{\mathcal{L}} e^{\frac{(-1)^j}{a}\left(\frac{x}{t} - v_{\mathcal{L}}\right) - 1} & \text{for } \left(v_{\mathcal{L}} + (-1)^j \, a\right) t \leq x \leq \left(v_{\mathcal{R}} + (-1)^j \, a\right) t, \\ \rho_{\mathcal{R}} & \text{for } x \geq \left(v_{\mathcal{R}} + (-1)^j \, a\right) t, \end{cases} \tag{3.73}$$

$$v\,(x,t) = \begin{cases} v_{\mathcal{L}} & \text{for } x \leq \left(v_{\mathcal{L}} + (-1)^j \, a\right) t, \\ \frac{x}{t} - (-1)^j \, a & \text{for } \left(v_{\mathcal{L}} + (-1)^j \, a\right) t \leq x \leq \left(v_{\mathcal{R}} + (-1)^j \, a\right) t, \\ v_{\mathcal{R}} & \text{for } x \geq \left(v_{\mathcal{R}} + (-1)^j \, a\right) t. \end{cases} \tag{3.74}$$

3.2. Entropy Solutions for the Isothermal Euler Equations

3.2.1. Weak solutions and the entropy - entropy flux pair of a conservation law

The drawback of having the conservation law on integral form, as in (3.11), is that the solutions are not necessarily unique. In particular, unphysical solutions may be weak solutions of a conservation law. By applying an entropy condition, it is possible to avoid such unphysical solutions. The name, entropy condition, originates from the Euler equations. For this set of equations, a physical shock obeys the second law of thermodynamics, that is, entropy must increase across the shock [31].

The entropy condition may be found by looking at the solution of the viscous regularisation of the conservation law (3.1) [26]

$$\frac{\partial \boldsymbol{U}^\epsilon}{\partial t} + \frac{\partial \boldsymbol{f}\left(\boldsymbol{U}^\epsilon\right)}{\partial x} = \epsilon \frac{\partial^2 \boldsymbol{U}^\epsilon}{\partial x^2}, \tag{3.75}$$

at the limit $\epsilon \to 0$ [26, 31]. The right hand side of Equation (3.75) is a viscous term, and ϵ is a small positive number. For fluid flow, this term models the effect of the fluid viscosity. Equation (3.75) is parabolic, and has a unique solution to any set of initial data [31, Ch. 11.13]. Thus, at the vanishing viscosity limit; $\epsilon \to 0$, the unique solution of (3.75) is identical to the physically sound solution of the conservation law (3.1).

In order to derive an entropy condition from Equation (3.75), a convenient approach is to write the equation on a weak form as shown below [26]

$$\int_0^\infty \int_{-\infty}^\infty \eta'\left(\boldsymbol{U}^\epsilon\right) \left[\frac{\partial \boldsymbol{U}^\epsilon}{\partial t} + \frac{\partial \boldsymbol{f}\left(\boldsymbol{U}^\epsilon\right)}{\partial x} - \epsilon \frac{\partial^2 \boldsymbol{U}^\epsilon}{\partial x^2} \right] \phi \, \mathrm{d}x \, \mathrm{d}t = 0. \tag{3.76}$$

Here, we have also multiplied by the first derivative of a convex entropy function, $\eta\left(\boldsymbol{U}^\epsilon\right)$.

Next, we introduce the entropy flux function $\Phi\left(\boldsymbol{U}\right)$. It is related to the entropy function through the integrability condition[2] [52]

$$\left(\Phi'\left(\boldsymbol{U}\right)\right)^T = \left(\eta'\left(\boldsymbol{U}\right)\right)^T \boldsymbol{f}'\left(\boldsymbol{U}\right). \tag{3.77}$$

With the aid of the chain rule, Equation (3.76) may then be re-formulated to

$$\int_0^\infty \int_{-\infty}^\infty \left[\frac{\partial \eta\left(\boldsymbol{U}^\epsilon\right)}{\partial t} + \frac{\partial \Phi\left(\boldsymbol{U}^\epsilon\right)}{\partial x} - \epsilon \eta'\left(\boldsymbol{U}^\epsilon\right) \frac{\partial^2 \boldsymbol{U}^\epsilon}{\partial x^2} \right] \phi \, \mathrm{d}x \, \mathrm{d}t = 0, \tag{3.78}$$

which can be written as

$$\int_0^\infty \int_{-\infty}^\infty \left[\frac{\partial \eta\left(\boldsymbol{U}^\epsilon\right)}{\partial t} + \frac{\partial \Phi\left(\boldsymbol{U}^\epsilon\right)}{\partial x} - \epsilon \left(\frac{\partial^2 \eta\left(\boldsymbol{U}^\epsilon\right)}{\partial x^2} - \eta''\left(\boldsymbol{U}^\epsilon\right) \left(\frac{\partial \boldsymbol{U}^\epsilon}{\partial x} \right)^2 \right) \right] \phi \, \mathrm{d}x \, \mathrm{d}t = 0. \tag{3.79}$$

[2] $\boldsymbol{B}^T$ is used as notation for the transpose of a matrix $\boldsymbol{B}$.

The test function, ϕ, is chosen to be non-negative and in the function space $C_0^\infty(\mathbb{R} \times \langle 0, \infty \rangle)$ such that $\phi(x, 0) = 0 \; \forall x \in \mathbb{R}$. Integrating by parts, we have

$$\int_0^\infty \int_{-\infty}^\infty \Bigg(- \frac{\partial \phi}{\partial t} \eta(\boldsymbol{U}^\epsilon) - \frac{\partial \phi}{\partial x} \Phi(\boldsymbol{U}^\epsilon) - \epsilon \frac{\partial^2 \phi}{\partial x^2} \eta(\boldsymbol{U}^\epsilon) + \epsilon \eta''(\boldsymbol{U}^\epsilon) \left(\frac{\partial \boldsymbol{U}^\epsilon}{\partial x} \right)^2 \phi \Bigg) \mathrm{d}x \, \mathrm{d}t = 0. \quad (3.80)$$

Looking at the fourth term, we see that it is positive as $\epsilon \geq 0$, $\eta''(\boldsymbol{U}) \geq 0$ and the partial derivative of $\boldsymbol{U}$ is squared. Thus we have the inequality

$$\int_0^\infty \int_{-\infty}^\infty \left(-\frac{\partial \phi}{\partial t} \eta(\boldsymbol{U}^\epsilon) - \frac{\partial \phi}{\partial x} \Phi(\boldsymbol{U}^\epsilon) - \epsilon \frac{\partial^2 \phi}{\partial x^2} \eta(\boldsymbol{U}^\epsilon) \right) \mathrm{d}x \, \mathrm{d}t \leq 0 \quad (3.81)$$

In the limit $\epsilon \to 0$, the third term in Equation (3.81) vanishes [26, 31]. The entropy condition may thus be written as

$$\int_0^\infty \int_{-\infty}^\infty \left[\frac{\partial \eta(\boldsymbol{U})}{\partial t} + \frac{\partial \Phi(\boldsymbol{U})}{\partial x} \right] \phi \, \mathrm{d}x \, \mathrm{d}t \leq 0, \quad (3.82)$$

or, on a differential form

$$\frac{\partial \eta(\boldsymbol{U})}{\partial t} + \frac{\partial \Phi(\boldsymbol{U})}{\partial x} \leq 0. \quad (3.83)$$

In general, the existence of an entropy – entropy - flux pair is not guaranteed for a hyperbolic conservation law that consists of more than one equation [31]. For such conservation laws, the integrability condition (3.77) is only fulfilled for entropy functions whose Hessian matrix symmetrizes $f'(\boldsymbol{U})$ [11, 52]. That is

$$\frac{\partial^2 \eta}{\partial \boldsymbol{U}^2} \frac{\partial \boldsymbol{f}}{\partial (\boldsymbol{U})} = \left(\frac{\partial^2 \eta}{\partial \boldsymbol{U}^2} \frac{\partial \boldsymbol{f}}{\partial (\boldsymbol{U})} \right)^T. \quad (3.84)$$

The expression can be re-formulated since the Hessian matrix of the entropy function is symmetric [8]

$$\frac{\partial^2 \eta}{\partial \boldsymbol{U}^2} \frac{\partial \boldsymbol{f}}{\partial (\boldsymbol{U})} = \left(\frac{\partial \boldsymbol{f}}{\partial (\boldsymbol{U})} \right)^T \left(\frac{\partial^2 \eta}{\partial \boldsymbol{U}^2} \right)^T = \left(\frac{\partial \boldsymbol{f}}{\partial (\boldsymbol{U})} \right)^T \frac{\partial^2 \eta}{\partial \boldsymbol{U}^2}. \quad (3.85)$$

This is in accordance with the multi-dimensional condition presented by Cockburn et al. [11], and will be applied in the next section for the isothermal Euler equations.

Additionally, for Equation (3.83) to hold, the entropy function must be convex. That is, the Hessian matrix $\eta''(\boldsymbol{U})$ must be positive definite [31]. A symmetric matrix $\boldsymbol{A}$ is positive definite if

$$\boldsymbol{x}^T \boldsymbol{A} \boldsymbol{x} > 0 \tag{3.86}$$

for all non-zero column vectors $\boldsymbol{x}$ [8].

3.2.2. An entropy - entropy flux pair for the isothermal Euler equations

Mechanical energy and the related flux function is a well known entropy - entropy flux pair for the isothermal Euler equations [17, Sec. 7.4]. In the following we will show that the entropy function satisfies the conditions in Equation (3.86) and Equation (3.85). The entropy function and the related flux function are derived from the energy equation (2.18), using the expressions for total energy (2.4), internal energy (2.5) and the isothermal pressure law (2.30). Using the primary variables, density (ρ) and velocity (v), the entropy function is

$$\eta = \frac{1}{2}\rho v^2 + \rho a^2 \ln\left(\frac{\rho}{\rho_0}\right) \tag{3.87}$$

while the entropy flux function is

$$\Phi = \rho v \left(\frac{1}{2}v^2 + a^2\left(\ln\left(\frac{\rho}{\rho_0}\right) + 1\right)\right). \tag{3.88}$$

For convenience we also derive the entropy and the entropy flux as functions of the conserved variables. The vector of conserved variables, $\boldsymbol{U}$ is identified from the conservation equations (2.19)- (2.20), and may be stated as

$$\boldsymbol{U} = \begin{bmatrix} \rho \\ \rho v \end{bmatrix} = \begin{bmatrix} u_1 \\ u_2 \end{bmatrix}, \tag{3.89}$$

using primary and conserved variables, respectively. Thus, in conserved variables, the entropy– and entropy - flux functions are

$$\eta(\boldsymbol{U}) = \frac{1}{2}\frac{u_2^2}{u_1} + u_1 a^2 \ln\frac{u_1}{\rho_0}, \tag{3.90}$$

$$\Phi(\boldsymbol{U}) = u_2\left(\frac{1}{2}\left(\frac{u_2}{u_1}\right)^2 + a^2\left(\ln\left(\frac{u_1}{\rho_0}\right)+1\right)\right). \tag{3.91}$$

The Hessian matrix of η may be calculated from (3.90)

$$\begin{aligned}\boldsymbol{\eta}''(\boldsymbol{U}) &= \frac{1}{u_1}\begin{bmatrix}\left(\frac{u_2}{u_1}\right)^2 + a^2 & -\frac{u_2}{u_1}\\ -\frac{u_2}{u_1} & 1\end{bmatrix}\\ &= \frac{1}{\rho}\begin{bmatrix}a^2+v^2 & -v\\ -v & 1\end{bmatrix}.\end{aligned} \tag{3.92}$$

The matrix is positive definite since

$$\begin{aligned}\boldsymbol{x}^T\boldsymbol{\eta}''\boldsymbol{x} &= \begin{bmatrix}x_1 & x_2\end{bmatrix}\frac{1}{\rho}\begin{bmatrix}a^2+v^2 & -v\\ -v & 1\end{bmatrix}\begin{bmatrix}x_1\\ x_2\end{bmatrix}\\ &= \frac{1}{\rho}\left((vx_1-x_2)^2 + x_1^2a^2\right) > 0.\end{aligned} \tag{3.93}$$

The next step is to calculate the Jacobian matrix of the flux vector, $\boldsymbol{f}'(\boldsymbol{U})$, based on the conservation law (2.19)- (2.20) together with the relevant pressure law (2.30). The flux function expressed in primary and conserved variables is

$$\boldsymbol{f} = \begin{bmatrix}\rho v\\ \rho\left(v^2+a^2\right)\end{bmatrix} = \begin{bmatrix}u_2\\ u_1\left(\left(\frac{u_2}{u_1}\right)^2 + a^2\right)\end{bmatrix}, \tag{3.94}$$

and the Jacobian is thus (see also (3.14)):

$$\frac{\partial \boldsymbol{f}}{\partial \boldsymbol{U}} = \begin{bmatrix}0 & 1\\ a^2 - \left(\frac{u_2}{u_1}\right)^2 & 2\frac{u_2}{u_1}\end{bmatrix} = \begin{bmatrix}0 & 1\\ a^2-v^2 & 2v\end{bmatrix}. \tag{3.95}$$

Then, the left and right hand sides of Equation (3.85) may be found as:

$$\begin{aligned}\frac{\partial^2\eta}{\partial \boldsymbol{U}^2}\frac{\partial \boldsymbol{f}}{\partial(\boldsymbol{U})} &= \frac{1}{\rho}\begin{bmatrix}a^2+v^2 & -v\\ -v & 1\end{bmatrix}\begin{bmatrix}0 & 1\\ a^2-v^2 & 2v\end{bmatrix}\\ &= \frac{1}{\rho}\begin{bmatrix}v(v^2-a^2) & a^2-v^2\\ a^2-v^2 & v\end{bmatrix},\end{aligned} \tag{3.96}$$

and

$$\begin{aligned}\left(\frac{\partial \boldsymbol{f}}{\partial(\boldsymbol{U})}\right)^T\frac{\partial^2\eta}{\partial \boldsymbol{U}^2} &= \begin{bmatrix}0 & a^2-v^2\\ 1 & 2v\end{bmatrix}\frac{1}{\rho}\begin{bmatrix}a^2+v^2 & -v\\ -v & 1\end{bmatrix}\\ &= \frac{1}{\rho}\begin{bmatrix}v(v^2-a^2) & a^2-v^2\\ a^2-v^2 & v\end{bmatrix},\end{aligned} \tag{3.97}$$

respectively. This proves that the Hessian matrix of the suggested entropy function symmetrizes the Jacobi matrix of the flux function.

Based on the results in Equation (3.93), (3.96) and (3.97), we can conclude that the entropy function (3.87) is a convex entropy function of the isothermal Euler equations.

The entropy flux function must satisfy the integrability condition (3.77). For the isothermal Euler equations this results in a set of two non-linear differential equations:

$$\begin{aligned}\begin{bmatrix}\frac{\partial\Phi}{\partial u_1} & \frac{\partial\Phi}{\partial u_2}\end{bmatrix} &= \begin{bmatrix}a^2\left(\ln\left(\frac{u_1}{\rho_0}\right)+1\right)-\left(\frac{u_2}{u_1}\right)^2, & \frac{u_2}{u_1}\end{bmatrix}\begin{bmatrix}0 & 1\\ a^2-\left(\frac{u_2}{u_1}\right)^2 & 2\frac{u_2}{u_1}\end{bmatrix}\\ &= \begin{bmatrix}\frac{u_2}{u_1}\left(a^2-\left(\frac{u_2}{u_1}\right)^2\right), & \frac{3}{2}\left(\frac{u_2}{u_1}\right)^2+a^2\left(\ln\left(\frac{u_1}{\rho_0}\right)+1\right)\end{bmatrix}.\end{aligned} \tag{3.98}$$

We may first consider the equation

$$\frac{\partial\Phi}{\partial u_1} = \frac{u_2}{u_1}\left(a^2-\left(\frac{u_2}{u_1}\right)^2\right). \tag{3.99}$$

If we consider u_2 as a constant and assume that the constant of integration, C, is a function of u_2 only, we can integrate and obtain:

$$\begin{aligned}\Phi(u_1,u_2) =& \int\frac{\partial\Phi}{\partial u_1}\,\mathrm{d}u_1\\ =& \int\frac{u_2}{u_1}\left(a^2-\left(\frac{u_2}{u_1}\right)^2\right)\mathrm{d}u_1\\ =& a^2u_2\ln(u_1)+\frac{1}{2}\frac{u_2^3}{u_1^2}+C(u_2).\end{aligned} \tag{3.100}$$

Using this result together with the second differential equation,

$$\frac{\partial\Phi}{\partial u_2} = \frac{3}{2}\left(\frac{u_2}{u_1}\right)^2+a^2\left(\ln\left(\frac{u_1}{\rho_0}\right)+1\right), \tag{3.101}$$

we get an expression for $C'(u_2)$

$$\begin{aligned}\frac{\partial\Phi}{\partial u_2} =& \frac{\partial}{\partial u_2}\left(a^2u_2\ln(u_1)+\frac{1}{2}\frac{u_2^3}{u_1^2}+C(u_2)\right)\\ =& a^2\ln(u_1)+\frac{3}{2}\left(\frac{u_2}{u_1}\right)^2+\frac{\mathrm{d}C(u_2)}{\mathrm{d}u_2}.\end{aligned} \tag{3.102}$$

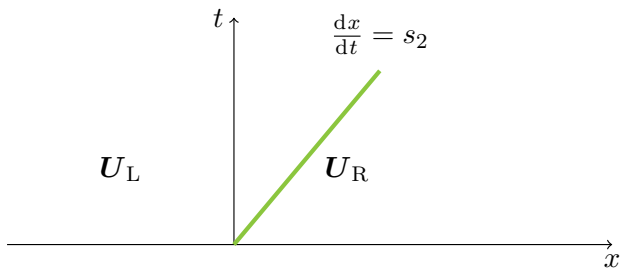

Figure 3.4.: Solution to a Riemann problem which consists of a non-trivial shock wave only

Therefore

$$\frac{\mathrm{d}C(u_2)}{\mathrm{d}u_2} = a^2 \left(1 - \ln\left(\rho_0\right)\right). \tag{3.103}$$

As Equation (3.103) does not include u_1, it may easily be integrated to yield the entropy flux function

$$\Phi = u_2 \left(a^2 \left(\ln\left(\frac{u_1}{\rho_0}\right) + 1 \right) + \frac{1}{2} \left(\frac{u_2}{u_1}\right)^2 \right), \tag{3.104}$$

which is identical to the suggested entropy flux function in Equation (3.91). This confirms that the suggested entropy – (3.87) and entropy - flux functions (3.88) is an entropy– entropy - flux pair for the isothermal Euler equations.

3.3. The Generalized Riemann Problem

In some particular cases, the solution to a standard Riemann problem (see Section 3.1) will consist of one or more waves of zero strength [53, p. 84]. For the isothermal Euler equations, two initial conditions may be connected by only one non-trivial wave if the right state, $(\rho_\mathrm{R}, v_\mathrm{R})$, lies on one of the wave curves emerging from the left state, $(\rho_\mathrm{L}, v_\mathrm{L})$, see Figure 3.1. For instance, assume that the right state lies on the 2-Shock wave curve. The intermediate state, $(\rho_\mathrm{m}, v_\mathrm{m})$, will then coincide with the left state. The rarefaction wave connecting the left and intermediate states is a wave of zero strength. An illustration of such a solution is found in Figure 3.4.

The construction of Riemann problems, whose solution contains trivial waves, is one of the main ingredients in the network theory for fluid flow.

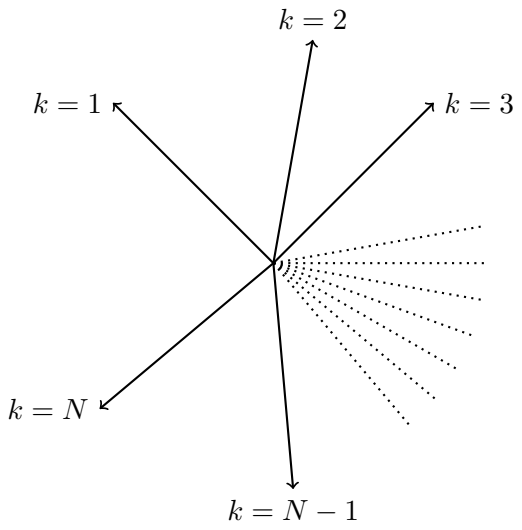

Figure 3.5.: A junction connecting N pipe sections

The theory is an approach used to solve flow conditions in a pipe network and relies on the solution of the generalized Riemann problem.

The generalized Riemann problem [25] consists of N segments, for instance pipe sections, that are connected at a junction as seen in Figure 3.5. In each segment, there is a constant initial condition

$$\boldsymbol{U}_k(x,0) = \bar{\boldsymbol{U}}_k \quad \forall k \in 1,...,N,\ x \in \mathbb{R}^+. \tag{3.105}$$

The fluid flow within each segment is described by a one dimensional, hyperbolic, conservation law

$$\frac{\partial \boldsymbol{U}_k}{\partial t} + \frac{\partial \boldsymbol{f}(\boldsymbol{U}_k)}{\partial x} = 0,\ x \in \mathbb{R}^+. \tag{3.106}$$

As seen from Equation (3.105) and (3.106), the segments are related to local, positive, x-axes. By definition, $x = 0$ at the segment - junction interface.

For each pipe section k, $\boldsymbol{U}_k(x,t)$ is found by constructing a standard Riemann problem

$$\begin{aligned} &\frac{\partial \boldsymbol{U}_k}{\partial t} + \frac{\partial}{\partial x}\boldsymbol{f}(\boldsymbol{U}_k) = 0, \\ &\boldsymbol{U}_k(x,0) = \begin{cases} \bar{\boldsymbol{U}}_k & \text{if } x > 0 \\ \boldsymbol{U}_k^* & \text{if } x < 0. \end{cases} \end{aligned} \tag{3.107}$$

While the solution to (3.107) is valid for $x \in \mathbb{R}$, $\boldsymbol{U}_k(x,t)$ is the solution to (3.107) restricted to $x \in \mathbb{R}^+$.

The state $\boldsymbol{U}_k^*$ is the constructed boundary condition at $x = 0$ for the k-th pipe. In general it is depending on the initial conditions of all the N segments

$$\boldsymbol{U}_k^*\left(\bar{U}_1, ..., \bar{U}_N\right) = \lim_{x \to 0^+} \boldsymbol{U}_k(x,t). \tag{3.108}$$

The dependency is expressed in a set of coupling conditions. The set is closely linked to the hyperbolic conservation law (3.106) which describes the flow in each segment. The conditions must therefore be derived for each law. For the isentropic and the isothermal Euler equations (2.19)- (2.20) there are two coupling conditions:

CC1: Mass is conserved at the junction:

$$\sum_{k=1}^{N} A_k \rho_k^* v_k^* = 0, \tag{3.109}$$

CC2: There is a unique, scalar, momentum related coupling constant at the junction:

$$\mathcal{H}(\rho_k^*, v_k^*) = \tilde{\mathcal{H}} \quad \forall k \in \{1, ..., N\}. \tag{3.110}$$

It may be noticed that the conservation of mass at a junction (3.109) only depends on the mass fluxes at the junction-section interfaces, see e.g. (2.16). This is due to the assumption that each junction is a point, which can not store mass at any time. The cross-sectional area of each segment, A_k, is as well included to cover cases where these may be different for the segments.

A closed set of equations, determining the boundary conditions, is obtained by adding the restriction that $\boldsymbol{U}_k^*$ and $\bar{\boldsymbol{U}}_k$ must be connected by waves of non-negative speed only. This ensures that the boundary condition propagates into each segment. The condition is reasonable at subsonic flow conditions, which is considered in the present work. Subsonic waves of the first family propagate with non-positive speed, while waves of the second family behave as desired. Thus the relations between $\boldsymbol{U}_k^*$ and $\bar{\boldsymbol{U}}_k$ are found from the equations for rarefaction and shock waves using $j = 2$.

For the isentropic Euler equations, rarefaction waves are described by Equation (3.40)

$$v_k^* = \bar{v}_k + \frac{2\sqrt{\gamma k_p}}{\gamma - 1}\left({\rho_k^*}^{\frac{\gamma-1}{2}} - \bar{\rho}_k^{\frac{\gamma-1}{2}}\right), \quad \rho_k^* \leq \bar{\rho}_k, \tag{3.111}$$

and shock waves are described by Equation (3.61)

$$v_k^* = \bar{v}_k + \sqrt{\frac{k_p \left(\bar{\rho}_k - \rho_k^*\right)\left(\bar{\rho}_k^\gamma - \rho_k^{*\gamma}\right)}{\bar{\rho}_k \rho_k^*}}, \quad \rho_k^* > \bar{\rho}_k. \tag{3.112}$$

Here, (ρ_k^*, v_k^*) is the left state and $(\bar{\rho}_k, \bar{v}_k)$ is the right state of the wave. We have also denoted the constant of the pressure law (2.27) as k_p to distinguish it from the notation of pipe section k.

In the network model based on the isothermal Euler equations, the rarefaction waves (3.38) may be written as

$$v_k^* - \bar{v}_k = a \ln\left(\frac{\rho_k^*}{\bar{\rho}_k}\right), \quad \rho_k^* \leq \bar{\rho}_k, \tag{3.113}$$

while the shock waves (3.63) may be stated as

$$v_k^* - \bar{v}_k = a\left(\sqrt{\frac{\rho_k^*}{\bar{\rho}_k}} - \sqrt{\frac{\bar{\rho}_k}{\rho_k^*}}\right), \quad \rho_k^* > \bar{\rho}_k. \tag{3.114}$$

The Mach number[3],

$$M = \frac{v}{a}, \tag{3.115}$$

where a is the constant speed of sound in the fluid (2.30), may be used to simplify Equation (3.113) and (3.114)

$$M_k^* - \bar{M}_k = \ln\left(\frac{\rho_k^*}{\bar{\rho}_k}\right), \quad \rho_k^* \leq \bar{\rho}_k, \tag{3.116}$$

$$M_k^* - \bar{M}_k = \left(\sqrt{\frac{\rho_k^*}{\bar{\rho}_k}} - \sqrt{\frac{\bar{\rho}_k}{\rho_k^*}}\right), \quad \rho_k^* > \bar{\rho}_k. \tag{3.117}$$

As solutions to generalized Riemann problems are weak solutions, an entropy condition is needed. The condition is strongly linked to the applied conservation law, just as the coupling conditions are.

Earlier, in Section 3.2.2, an entropy - entropy flux pair for the isothermal Euler equations was derived from the energy equation (2.18), together with the expressions for total energy (2.4), internal energy (2.5) and the

[3]Notice that the Mach number definition here is somewhat different from standard notation. Usually Mach numbers are only expressed as positive values. However, in the present work it is found convenient to use both positive and negative numbers such that subsonic flow is defined to be in the range $M \in \langle -1, 1 \rangle$.

isothermal pressure law (2.30). The obtained entropy flux function (3.88) is applied as entropy condition in the corresponding generalized Riemann problem [13]

$$\sum_{k=1}^{N} A_k \rho_k^* v_k^* \left(\frac{1}{2} \left(v_k^* \right)^2 + a^2 \left(\ln \left(\frac{\rho_k^*}{\rho_0} \right) + 1 \right) \right) \leq 0. \tag{3.118}$$

The condition states that energy may not be produced at a junction. Due to conservation of mass (3.109), the equation may be simplified to

$$\sum_{k=1}^{N} A_k \rho_k^* v_k^* \left(\frac{1}{2} \left(v_k^* \right)^2 + a^2 \ln \left(\rho_k^* \right) \right) \leq 0. \tag{3.119}$$

For the isentropic Euler equations, the entropy flux function may be also be derived from the energy equation, when the γ-pressure law (2.27) is inserted instead of the isothermal pressure law [17, Sec. 7.4]

$$\sum_{k=1}^{N} A_k v_k^* \left(\rho_k^* \left(\left(\frac{k_p}{\gamma - 1} \rho_k^{*\gamma - 1} + C \right) + \frac{1}{2} v_k^{*2} \right) + k_p \rho_k^{*\gamma} \right) \leq 0. \tag{3.120}$$

By conservation of mass at the junction (3.109) the entropy condition of network models based on the isentropic Euler equations may be stated as

$$\sum_{k=1}^{N} A_k \rho_k^* v_k^* \left(\frac{k_p \gamma}{\gamma - 1} \rho_k^{*\gamma - 1} + \frac{1}{2} v_k^{*2} \right) \leq 0. \tag{3.121}$$

The main question is then which momentum related coupling constant, $\mathcal{H}$ (3.110), should be applied. This is the main topic of this thesis. It has been investigated in Paper II to Paper V, found in Appendix C to F. The literature survey results presented in the next chapter will as well to a great extent be centred on this question.

"To get to know, to discover, to publish – this is the destiny of a scientist."

François Arago

4

Modelling Approaches for Junction Flow

The flow of single- and two-phase fluids in junctions is present in many different applications. Accordingly, there exists a wide range of mathematical problem descriptions in the literature. Table 4.1 presents an overview of some relevant journal papers, showing that models have been derived for several conservation laws and that the junction itself is modelled at different detail levels.

Single phase models are used for applications like gas flow in pipe networks [30, 34, 40, 42, 43], safety considerations in nuclear power plants [21, 37, 55], flow and pressure wave considerations in combustion engines [9, 27, 36, 41–43] and blood flow [34].

For two-phase flows, the prediction of phase separation is an important parameter. One such application is presented by Margaris [33], where the separation effect in a T-junction is considered in the context of gas-liquid transport pipelines and sub-sea separation.

In the present chapter, the aim is to present some of the proposed modelling approaches applied in the literature during the last decades. An overview of the derived network models, where the junction is treated as a single point and wave equations are applied, will be given in Section 4.1. Further, examples of more geometry specific models, where volume and/or

full geometry is considered, will be given in Section 4.2.

4.1. Network Theory in the Literature

4.1.1. Network models for 2×2 conservation laws

Banda et al. [2, 3] derived an early mathematical model for fluid flow in junctions, applied to the isothermal Euler equations. They introduced the use of half-Riemann problems and the restrictions on velocities of waves connecting the boundary - and initial conditions of each pipe section. However, as the model was heavily based on network models for traffic flow [25], the description of the generalized Riemann problem differs from the one presented in Section 3.3 and in Paper II (Appendix C) to Paper IV (Appendix E).

The model was based on two sets of pipe sections connected at a junction; the first set, δ_j^-, contained all pipe sections with axis direction towards the junction, the second set, δ_j^+, contained the pipe sections with axis direction away from the junction. This was combined with the assumption of positive flow velocity in all pipe sections at all times. As a consequence the flow direction was given a priori.

The overall problem was described as a maximisation problem with total mass flux as object function. The problem was subject to several constraints, in particular conservation of mass at the junction and upper bounds on the mass flux at the boundary of each pipe section. The upper limits were referred to as supply and demand functions, which were given by the wave equations and the constraint of non-positive or non-negative wave velocity.

Banda et al. [2] presented results for the momentum related coupling constant of equal pressure. In particular, numerical density and velocity profiles were presented for four different cases, for junctions connecting two and three pipe sections.

Banda et al. [3] compared the restriction of equal pressure at all boundaries to the one of subsonic flow at the boundaries of all pipe sections in δ_j^+. Numerical results were presented for five different cases for junctions connecting two and three pipe sections. In some of the cases, the fluid speed of sound was assumed to vary among the pipe sections.

Herty and Seaïd [24] performed numerical simulations on a two-dimensional domain. The averaged results were compared with analytical results given by the network model presented by Banda et al. [2]. The comparison was performed for two different flow configurations in a T-junction. In the first case there were one ingoing and two outgoing flows. In the second, there

		Single point	Volume	Geometry dependent	
					T-junction
Single - phase	Scalar conservation equations	Boutine et al. [6]			
	Isothermal Euler equations	Banda and Herty [1] Banda et al. [2] Banda et al. [3] Herty and Seaïd [24]			
	Isentropic Euler equations	Colombo et al. [12] Colombo and Garavello [13] Colombo and Garavello [14] Garavello [20]			
	Other conservation laws for mass and linear momentum	Brouwer et al. [7] Herty et al. [22] Marušić-Paloka [34]	Kiuchi [30] Osiadacz [40]		
	Euler equations	Chalons et al. [10] Colombo and Marcellini [15] Colombo and Mauri [16] Herty [23]	Greyvenstein [21]	Hong and Kim [27] Pearson et al. [41]	Chalet and Chesse [9]
	Other conservation laws for mass, linear momentum and energy	Brouwer et al. [7]		William-Louis et al. [56]	Naeimi et al. [36] Naik-Nimbalkar et al. [37] Pérez-García et al. [42] Pérez-García et al. [43] Walker et al. [55]
Two - phase	Drift-flux model	Banda et al. [4] Banda et al. [5] Ngnotchouye [39]			
	Other models				Margaris [33] Vist [54]

Table 4.1.: Modelling approaches and relevant scientific papers

were two ingoing and one outgoing flow. In both cases the flow direction in the main branch was equal.

For each of the flow configurations, one flow parameter was varied while the other parameters were held constant. Velocity and density of the first pipe section were chosen as variable flow parameters and two corresponding sets of results were obtained. The results showed that the numerical and theoretical results followed a similar trend. However, the second flow configuration yielded significant differences in the results which were explained by the effect of the geometry on the two-dimensional flow. It was therefore concluded that for this flow configuration, flow- and geometry dependent pressure loss coefficients would be beneficial.

Banda and Herty [1] included a network model for the isothermal Euler equations in a dynamic compressor optimisation model. The pipe sections were divided into incoming and outgoing sets, and the coupling conditions of conservation of mass and equal pressure were applied. The flow velocities were restricted to non-negative values only. The network model was used as a small scale model, providing detailed flow description. In the optimisation process, a less detailed model was used for the extensive calculations while the small scale model was used to verify the estimated derivatives of the objective function.

Colombo and Garavello [13] considered the isentropic Euler equations and formulated the generalized Riemann problem at a junction using an entropy constraint to select the physical solutions. The axis direction of all pipe sections were from the junction and outwards, and the flow velocities could be both positive and negative. The momentum flux was suggested as the preferred momentum related coupling constant. Using this constant, the overall problem was proved well-posed as it was continuously dependent on the initial data of a three pipe junction. If the overall model applied pressure as momentum related coupling constant, it was seen to fail this criterion.

The uniqueness of solutions to the generalized Riemann problem was proved for the special case of initial conditions that are perturbed states of stationary solutions to the problem. The proof is based on the implicit function theorem. Similar results were provided for the Cauchy problem by Colombo and Garavello [14].

Colombo et al. [12] presented a unified approach for 2×2 conservation laws. For the isentropic Euler equations, numerical results were provided for three different test cases and both pressure and momentum flux were considered as momentum related coupling constants. The initial conditions

were obtained by perturbing states that were steady solutions to both models. The cases were set up such that one or more shock waves propagated from a pipe section and into the junction, and the resulting waves were reported. In the last test case, the two coupling constants were seen to yield fundamentally different waves as momentum flux yielded a rarefaction wave while pressure resulted in a shock wave in one of the pipe sections.

Herty et al. [22] presented a network model and numerical results for a conservation law derived from the isothermal Euler equations. The derived set of equations was based on the neglect of inertia and gravity effects, both justifiable simplifications for gas flow in pipelines. Brouwer et al. [7] also applied relevant simplification for friction dominated gas flow in networks and presented network results for two different conservation laws. The first law consisted of mass and momentum conservation equations, the second law also included conservation of energy.

4.1.2. Network models for the Euler equations

A network model for the Euler equations was derived by Colombo and Mauri [16]. The coupling conditions included conservation of mass and energy at the junction and the entropy condition was based on the thermodynamical entropy function for the conservation law. Existence and uniqueness of solutions were considered for the general case when linear momentum was not conserved, and for the special case for which conservation could be assumed. Both the Riemann – and the Cauchy problems were investigated, and the considered conditions included subsonic as well as supersonic flow conditions. In the case of Riemann problems and special conditions for which conservation of linear momentum could be assumed, the existence of a unique solution was proved for initial data which were perturbations of stationary solutions. The proof was given for the case of one pipe section with outgoing flow and ingoing flow in the remaining $N - 1$ pipe sections.

Numerical results for two different network models were presented by Herty [23]. The considered models were based on the work of Colombo and Mauri [16], but in addition to momentum flux, pressure was also considered as momentum related coupling constant. The well-posedness of the last model was proved by a similar approach as used by Colombo and Mauri [16]. The numerical results were compared to corresponding two dimensional simulation results. It was concluded that the comparison did not give any indication whether momentum flux or pressure is the most appropriate momentum related coupling constant. In general, the values obtained

by the network – and two dimensional models were of the same order. Hence it was concluded that the both the suggested coupling constants are close to the "correct" one.

Chalons et al. [10] and Colombo and Marcellini [15] considered the coupling conditions for the Euler equations at the special condition of a junction connecting two pipe sections. Chalons et al. [10] presented results for the case where in each section, different equations describe the pressure as a function of density and specific internal energy. Three different set of coupling conditions were investigated and an overview over possible solutions to the coupled Riemann problem was provided. For scalar conservation laws, a similar study was presented by Boutine et al. [6]. They considered the coupling of a left and a right state, with different flux functions, both assumed to be C^1. The main application for this kind of coupling conditions is when multiple modelling scales are used to describe for example flow conditions.

Colombo and Marcellini [15] focused on the coupling of two sections with different cross sectional area, and how this may be expanded to the case of fluid flow in a duct with varying cross-sectional area. The results were derived under the important assumption that the area profile had a bounded total variation. By imposing three conditions on the set of coupling conditions, a well posedness result on the network model was stated. Four different sets of conditions were considered. The first set is valid when the change of cross-sectional area is a smooth function. Two of the sets included the well known approach of using momentum flux and pressure as coupling constant, respectively. The last set was based upon the conservation of linear momentum and the momentum related coupling condition therefore accounted for the difference in cross-sectional area. Each of the sets were seen to fulfil the three conditions established.

4.1.3. Network models for the drift-flux model

Banda et al. [4] and Banda et al. [5] presented results for the drift-flux model under the assumption of isothermal flow with equal gas and liquid flow velocities. Banda et al. [4] assumed further that the two phases had equal speed of sound. Conservation of mass for each of the two phases were applied as coupling conditions, as well as momentum flux as momentum related coupling constant. The well-posedness of perturbed initial data was proved in a similar manner as by Colombo and Mauri [16], and numerical results were presented for junctions connecting three and four pipe sections, respectively.

Banda et al. [5] expanded the theoretical results to the more general case of unequal speed of sound in the two phases. Numerical results for a junction with three connected pipe sections were also provided. These numerical results, together with a more extended description of the theoretical results were presented by Ngnotchouye [39].

4.2. Geometry-based models and other approaches describing junction flow

Marušić-Paloka [34] derived a matched asymptotic expansion describing velocity and pressure for incompressible flow described by the Navier-Stokes equations. The expansion was based on the assumptions that the flow was described as Poiseuille flow far from the junction and as Leray's flow close to the junction. The Poiseuille flow is described for the case of continuous pressure in the junction point.

This first approach does not consider the geometry of the junction. In the following, examples of more geometry-based models will be given. One common approach is to consider the total volume of the junction. Based on the sum of mass-fluxes at the junction, the junction pressure may be estimated. Such models were presented by Osiadacz [40], Kiuchi [30] and Greyvenstein [21]. Hong and Kim [27] used normal vector information derived from the full geometry of the junction along with its volume in order to calculate the junction cell state variables. The normal vectors were as well applied in the calculation of the one dimensional momentum fluxes at the pipe-junction boundaries.

An obvious approach for studying flow conditions in junctions is to apply a three-dimensional simulation model for the calculation of the pipe-junction boundary conditions. For many applications this is considered too computationally costly, and thus discarded. Pearson et al. [41] used a two-dimensional simulation model in order to estimate the shock-wave propagation through a three-pipe junction. The results were compared against schlieren images and measured pressure-time histories. It was concluded that the pressure-loss characteristics of the junction was predicted sufficiently accurately by a fairly coarse mesh. This enabled the use of such a model within an engine manifold simulation tool, where it was used in combination with one-dimensional gas dynamic models.

Walker et al. [55] performed three-dimensional CFD calculations for a T-type junction where the side branch was connected at an angle of 90°.

The aim of the work was to improve the CFD model that was used to evaluate the mixing of coolant flows with different properties in nuclear plants. Numerical results were provided for three different turbulence models and were compared against experimental data. The comparison showed that all the numerical results underestimated the turbulent mixing and the turbulent momentum transport downstream of the junction. Therefore, measured profiles were more uniform than the calculated ones. An improved correspondence between experimental and calculated results was obtained by altering a specific parameter in one of the turbulence models.

Naik-Nimbalkar et al. [37] also evaluated the predicted thermal mixing in a 90° T-type junction. The calculations were performed using a three-dimensional, steady state CFD model and the results were compared to experimental data. It was concluded that a good agreement was observed.

The method of characteristics is a well known technique for solving partial differential equations [49, 56]. William-Louis et al. [56] applied the method in an iterative manner considering all pairs of one inlet- and one outlet flow consecutively in each iteration. For each pair, the flow condition was solved by applying the method of characteristics, while also accounting for conservation of mass at the junction and equal specific stagnation enthalpy of all outgoing flows. Additionally, geometry dependent pressure loss coefficients were used in order to determine the loss of stagnation pressure. These were taken from the incompressible theory. The calculations were performed until a set of convergence criteria was met.

Pressure loss coefficients have been derived for compressible flows by for example Chalet and Chesse [9], Pérez-García et al. [42, 43] and Naeimi et al. [36]. Chalet and Chesse [9] considered T-type junction where the first and third pipe section are directly connected, while the second pipe was connected at an angle, δ. They expressed their pressure loss coefficient as

$$K = \frac{\left(\frac{1}{2}\rho v^2 + p\right)_{\text{us pipe}} - \left(\frac{1}{2}\rho v^2 + p\right)_{\text{ds pipe}}}{\left(\frac{1}{2}\rho v^2 + p\right)_{\text{com pipe}}}, \tag{4.1}$$

where p is the static pressure, "us" and "ds" denotes up and down stream, respectively, and "com" denotes common. In total there are six different flow configurations in a junction that connects three pipe sections. For each configuration, the pressure loss coefficient was calculated from numerical results provided by a three-dimensional simulation model run in Fluent. The coefficient was seen to be a function of the connection angle, δ, and

area ratio, $\Phi = {}^{A_1}/_{A_2}$. The first and third pipe section were of equal cross-sectional area.

An experimental set up was used in order to compare measured pressure profiles to numerical results obtained by the aid of two different pressure loss coefficients. The coefficients considered were the one recently derived and an alternative model earlier presented in the literature. The experiments were performed for $\delta = 45°$ and were conducted by measuring pressure near the pipe-junction interfaces as a pressure wave entered the system. The comparison showed that the alternative model did not perform as well as the recently derived one. This was assumed to be caused by the fact that the first one was based on steady and not transient flow conditions. Pressure loss coefficients for Y-type junctions were also considered numerically.

Pérez-García et al. [42] considered a 90° T-type junction. The loss coefficient was defined as

$$K = \frac{p^*_{0,\text{us pipe}} - p^*_{0,\text{ds pipe}}}{(p^*_0 - p^*)_{\text{com pipe}}}, \tag{4.2}$$

when using the same notation as Chalet and Chesse [9]. $p_{0,j}$ is the stagnation pressure in pipe section j and p_j is the static pressure. The notation p^* indicates that the pressure has been extrapolated to the geometrical junction under the constraint that the frictional losses had been subtracted from the total energy losses. This was achieved by applying an adiabatic, compressible steady one-dimensional flow model. The pressure loss coefficient was reported for the parameters mass flow rate ratio between the branches, q, and extrapolated Mach number in the common branch, $M^*_{\text{com pipe}}$. The Mach number dependence for the selected pressure loss coefficient was however seen to be weak.

Naeimi et al. [36] also presented numerically obtained pressure loss coefficients on the form of (4.2). However, they related the total pressure drop in the direction of total mass flow to the extrapolated dynamic pressure in the common branch

$$K = \frac{\left(\frac{1}{2}\rho v^2 + p\right)_{\text{us pipe}} - \left(\frac{1}{2}\rho v^2 + p\right)_{\text{ds pipe}}}{(p^*_0 - p^*)_{\text{com pipe}}}. \tag{4.3}$$

A T-type junction with fixed geometry was considered, and the results were compared against experimental results reported in the literature. In general, a good agreement was reported.

An alternative coefficient, named "Linking between branches coefficient" was presented by Pérez-García et al. [43]. It was defined as

$$\hat{K}_j = \frac{\frac{p^*_{0,\text{com pipe}}}{p^*_{\text{com pipe}}} - 1}{\frac{p^*_{0,j}}{p^*_j}}, \tag{4.4}$$

when stated in a similar notation as above. Based on numerical results, it was found that the coefficient could be expressed on the form

$$\hat{K}_j = s\left(M^*_{\text{com pipe}}\right)^m (1+q)^{n-1}, \tag{4.5}$$

where s, m and n were parameters obtained by a least minimum square fit procedure.

Using the new coefficient, the numerical and experimental results from Pérez-García et al. [42] were compared. The comparison showed a good agreement between experimental data and numerical results.

When two-phase flows are considered, the distribution of the two phases between the connected pipe sections is an additional phenomenon which needs to be modelled. This is a complex phenomenon, and a full overview over the different modelling approaches will therefore not be attempted. Rather, two different works, provided by Vist [54] and Margaris [33] will be given as examples.

Vist [54] investigated the distribution of two-phase flows in the manifold of a compact heat exchanger. Experimental data were compared to the numerical results from a mathematical model which treated the manifold as a set of T-type junctions in series. Here, pressure losses were modelled according to the proposed method by Saba and Lahey [48] and the flow in each pipe section was treated as one-dimensional. Three different two-phase distribution models were implemented. Two models modelled the best and worst case scenarios of uniform and separated distribution, respectively. The third approach applied a set of correlations derived from the experimental data. Inlet vapour fraction, mass flow rate and heat load for each pipe section were compared, and the uniform distribution assumption was seen to yield the largest deviation from the experimental data. The model was used to investigate the consequences of two-phase maldistribution between parallel passes in compact heat exchangers. In particular, the reduction of heat exchanger capacity was reported.

Margaris [33] developed a model for phase distribution and pressure drop through a 90° T-type junction. Having a vertical side branch, separation

of the gas and liquid phases was sought. Experimental data were provided mainly for stratified and slug flow conditions in the horizontal pipe section. The data were compared with the numerical results. The mathematical model was based on the assumption of isothermal flow in the junction, and the flow within each pipe section was modelled as one-dimensional. Conservation of mass, momentum and energy was accounted for, as well as the vena contracta area of the vertical branch. The void fraction of the horizontal, common pipe section was calculated based on the identified flow patterns within the section. The comparison showed satisfactory results and the model was seen useful as it could easily be incorporated into one-dimensional multiphase flow codes.

"Science knows only one commandment - contribute to science."

Bertolt Brecht

5 Introduction to Scientific Papers

5.1. Paper I - An Improved Roe Solver for the Drift-Flux Two-Phase Flow Model

Authors: Gunhild Allard Reigstad and Tore Flåtten
Presented at the 8th International Conference on CFD in Oil & Gas, Metallurgical and Process Industries, 21-23 June 2011, Trondheim, Norway

The work presented in this first paper used the Roe solver derived by Flåtten and Munkejord [19] as a starting point. The solver is based upon the construction of a Roe matrix, $\widehat{\boldsymbol{A}}$, such that the non-linear hyperbolic conservation law (3.6) may be estimated by the aid of the locally linearised system

$$\frac{\partial \widehat{\boldsymbol{U}}}{\partial t} + \widehat{\boldsymbol{A}} \frac{\partial \widehat{\boldsymbol{U}}}{\partial x} = 0, \tag{5.1}$$

see for example [19, 31, 45, 46]. $\widehat{\boldsymbol{A}}$ must fulfil three conditions, where the condition which requires the most concern is

$$\widehat{\boldsymbol{A}}_{i-1/2} \left(\boldsymbol{Q}_{\mathrm{i}} - \boldsymbol{Q}_{\mathrm{i}-1} \right) = \boldsymbol{f} \left(\boldsymbol{Q}_{\mathrm{i}} \right) - \boldsymbol{f} \left(\boldsymbol{Q}_{\mathrm{i}-1} \right). \tag{5.2}$$

Here $\boldsymbol{Q}_{\mathrm{i}}$ and $\boldsymbol{Q}_{\mathrm{i}-1}$ are the vectors containing the discrete conserved variables for two neighbour grid cells and $\boldsymbol{f}$ is the vector of flux functions.

Flåtten and Munkejord [19] derived a Roe matrix that contained two different expressions for averaged velocities

$$\tilde{v_\ell} = \frac{\sqrt{m_\ell^{\mathrm{L}}} v_\ell^{\mathrm{L}} + \sqrt{m_\ell^{\mathrm{R}}} v_\ell^{\mathrm{R}}}{\sqrt{m_\ell^{\mathrm{L}}} + \sqrt{m_\ell^{\mathrm{R}}}}, \quad \tilde{v_{\mathrm{g}}} = \frac{\sqrt{m_{\mathrm{g}}^{\mathrm{L}}} v_{\mathrm{g}}^{\mathrm{L}} + \sqrt{m_{\mathrm{g}}^{\mathrm{R}}} v_{\mathrm{g}}^{\mathrm{R}}}{\sqrt{m_{\mathrm{g}}^{\mathrm{L}}} + \sqrt{m_{\mathrm{g}}^{\mathrm{R}}}} \tag{5.3}$$

and

$$\hat{v_\ell} = \frac{1}{2}\left(v_\ell^{\mathrm{L}} + v_\ell^{\mathrm{L}}\right), \quad \hat{v_{\mathrm{g}}} = \frac{1}{2}\left(v_{\mathrm{g}}^{\mathrm{L}} + v_{\mathrm{g}}^{\mathrm{L}}\right). \tag{5.4}$$

The indexes ℓ and g denotes liquid and gas phase, respectively. In the present paper, the derivation of the averaged parameters was changed such that only the standard Roe-averaged velocities (5.3) were applied.

With the Roe matrix defined, the numerical implementation of the Roe scheme along with simulation results were presented. The first case presented the results of a Riemann problem, where the speed of sound is different for the two phases. The derived profiles were reasonable, and indicated that the implementation had been correctly performed.

The second case consisted of a volume fraction profile that initially was shaped as a Gauss curve and that moved with the fluid velocity. The test case was used to estimate the accuracy of the implemented model. As expected, the numerical scheme without a limiter approached a convergence order of 1. The scheme that applied the MC limiter (see [31, 46]) approached a convergence order of 2.

CPU time consumption was also evaluated by performing a comparison against the FORCE scheme. This scheme is regarded as the optimal among the three point centred difference schemes, a group of schemes considered as easy and convenient to implement. The comparison showed that the Roe scheme was far more efficient in terms of CPU time requirement for a given numerical error.

The final case consisted of varying in-flow conditions in a pipe section, where the outlet pressure was kept constant and wall friction was accounted for. The results were seen to correspond well with the ones presented by Flåtten and Munkejord [19].

My contribution The process of establishing the present paper served as my introduction to CFD models and numerical solvers. This was one of my motivations for choosing to program the simulation model from scratch. Into this model I implemented the improved Roe matrix which was derived by Tore Flåtten. He also helped me with the selection of test cases and as I

processed the simulation results. The conference paper was mainly written by me.

5.2. Paper II - Coupling Constants and the Generalized Riemann Problem for Isothermal Junction Flow

Authors: Gunhild A. Reigstad, Tore Flåtten, Nils Erland Haugen and Tor Ytrehus
Submitted to Journal of Hyperbolic Differential Equations, September 2013

The present work investigated junction flow where the flow in each pipe section is modelled by the isothermal Euler equations and where all pipe sections connected at a junction have equal cross-sectional areas. The earlier proposed momentum related coupling constants of momentum flux and pressure were considered, and Bernoulli invariant was launched as an alternative expression. Earlier, Colombo and Garavello [13] had investigated the well-posedness of a similar network formulation that was derived for the isentropic Euler equations. This was performed by considering the continuous dependence on initial data and the stability of solutions to problems with initial conditions that were obtained by perturbation of steady solutions [13].

In the present work, we investigated the existence and uniqueness of solutions in the entire subsonic region. The region was in addition precisely defined. The investigation showed that if one did not consider the entropy condition, solutions exist and are unique within the subsonic region if the coupling constant is a monotone function of the constructed state variables. Momentum flux, pressure and Bernoulli invariant were all seen to fulfil this requirement.

The entropy condition was then evaluated for the case of three pipe sections connected at a junction. It was proved that only Bernoulli invariant as coupling constant yield physical solutions for all subsonic flow conditions. Both momentum flux and pressure yield unphysical solutions for certain ranges of flow velocities. In particular, there is a duality between the two constants. If pressure yield a physical solution for a certain flow condition, momentum flux yield an unphysical solution, and opposite. Bernoulli invariant implicitly yields energy conservation at each junction and hence the solutions are physical.

The choice of the Bernoulli invariant as momentum related coupling constant was made with a twofold motivation. First, we seek to describe ideal, reversible junction flow in order to apply a similar approach as what is done for the fluid flow within each pipe section. This flow is described by a conservation law, which describes ideal flow, together with irreversible factors like wall friction that are added as source terms. For such ideal junction flow, the concept of uninterrupted streamlines is valid and the choice of a streamline invariant like the Bernoulli invariant natural.

Second, the Bernoulli invariant is derived from an equation describing conservation of mechanical energy valid for smooth flows. The equation is found by applying the three-dimensional momentum conservation equation together with the equation describing conservation of mass. Therefore it may be argued that some of the information on the momentum equations, which is three-dimensional for junctions, is contained within the Bernoulli invariant.

My contribution Network theory was fairly unknown to me and my co-authors as we began our work. I therefore initiated the investigation by performing an extensive literature study in order to obtain an understanding of the underlying mathematical theory. The study showed that both pressure and momentum flux were applied as momentum related coupling constant. Together with Tore Flåtten, I investigated the consequences of applying the two different coupling constants. This revealed the finding that both models did not fully respect the entropy principle for relevant flow conditions.

The proposition of using Bernoulli invariant was reached after intensive discussions with the co-authors, combining insights from physics, mathematics and engineering.

The final scientific paper was written by me, based on calculations performed by me and Tore Flåtten. The latter contributed with an outline of the proof for existence and uniqueness for the case of momentum flux as coupling constant, and also provided the background information on the Bernoulli invariant derivation. I generalized and structured the results. In particular the proof for existence and uniqueness was re-written to account for pressure, momentum flux and Bernoulli invariant as coupling constant. In addition I derived the proofs related to the entropy considerations for the junction with three connected pipe sections.

5.3. Paper III - Numerical Network Models and Entropy Principles for Isothermal Junction Flow

Author: Gunhild A. Reigstad
Accepted by Networks and Heterogeneous Media, December 2013

The focus of the present work was the numerical implementation of the isothermal network model and simulation results for selected test cases. However, some theoretical investigations were as well presented. First, the proof of existence and uniqueness of solutions was expanded to the case of junctions connecting pipe sections with different cross-sectional areas. Second, two requirements on the momentum related coupling constant were derived. The requirements must be fulfilled if the network model is to correctly predict the solution of the standard Riemann problem.

For the numerical implementation, great care had to be taken in order to ensure numerical conservation of mass at the junction. This was obtained by applying the Godunov flux at the pipe-junction interface. The flow within each pipe section was calculated by the Roe scheme with high order correction terms.

Simulation results were presented for two different network layouts. The closed configuration, shown in Figure 5.1, and a symmetric branch-tree layout shown in Figure 5.2.

For the closed configuration, two different sets of initial data were considered. Each of the simulation results were investigated in terms of total energy. Since there were no energy sources within the system and shock waves were propagating in the pipe sections, we expected that total energy should decrease. Analytical expressions for total energy under the assumption of energy conservation at the junctions were derived and applied in the analysis of short-term simulation results. The comparison showed that for the first set of initial data, pressure as momentum related coupling constant yielded an unphysical solution, while the solution from the model which applied momentum flux was physical. For the second set of initial data, the opposite was the case; for these initial conditions momentum flux yielded the unphysical solution. As expected, Bernoulli invariant yielded physical solutions for both sets of initial data.

In addition to short-term simulation results, long-term results were provided. For these, no analytical profiles were available. However, the influence of the unphysical solutions were observed as non-monotonically decreasing energy profiles.

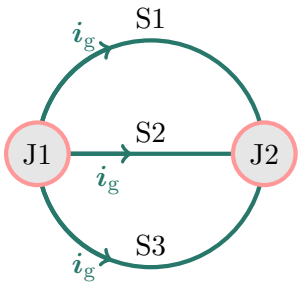

(a) Principal diagram

(b) Relation between the global axis, i_g, and the local axis, i_l, used by the network model.

Figure 5.1.: Closed network configuration

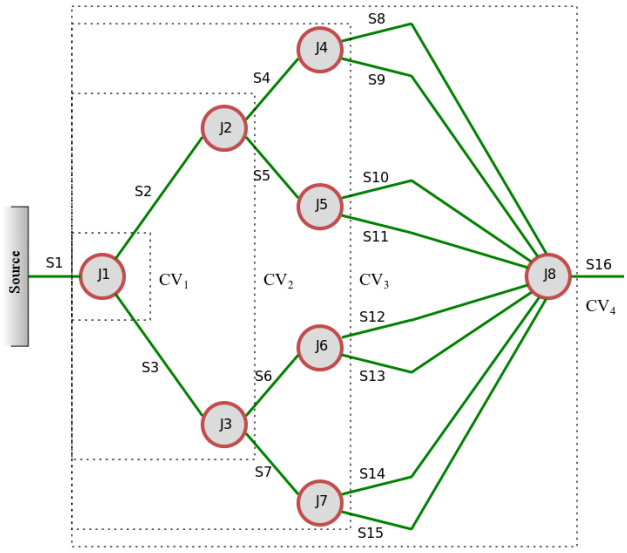

Figure 5.2.: Symmetric branch-tree layout

Steady state flow conditions were evaluated for the symmetrical branch-tree case. In this case, the pipe network was connected to a source of constant pressure and the outlet pressure of the last pipe section was held constant. Two different sets of pipe sections were considered. In the first, all pipe sections were of equal cross-sectional area. In the second, the cross-sectional area of each of the pipe sections with outgoing flows were half of the area of the pipe section with ingoing flow. For the first set of pipe sections, the influence of energy production in some of the junctions was seen for the model that used momentum flux as momentum related coupling constant. Pressure as coupling constant yielded energy dissipation in the same junctions and Bernoulli invariant yielded energy conservation. For the second set of pipe sections, energy conservation was observed in all junctions, for all three models. An analytical approach was used to verify this result.

My contribution The symmetric branch-tree layout was suggested by Tore Flåtten. Otherwise, the content of the paper was derived and written by me. As for the other papers, Tore Flåtten contributed with valuable suggestions for improvements of the written paper. Especially the content on numerical conservation of mass at the junctions was greatly improved by his comments. In the first version of the paper he was therefore the second author. However, as a part of the review process he chose to withdraw as he found that his contributions did not warrant co-authorship.

5.4. Paper IV - Numerical Investigation of Network Models for Isothermal Junction Flow

Authors: Gunhild A. Reigstad and Tore Flåtten
Extended version of paper submitted to the ENUMATH 2013 Proceedings Volume (Springer), November 2013

Numerical results for two different junction layouts were presented. The first consisted of one junction connecting five pipe sections. The case demonstrated the suitability of the modelling approach for junctions connecting several pipe sections. The entropy condition was evaluated based on the numerical results, and energy production was seen to occur in the results from the models that applied pressure and momentum flux as momentum related coupling constant. Bernoulli invariant yielded energy conservation

in the junction.

The second case consisted of the closed configuration shown in Figure 5.1 together with a third set of initial conditions. The numerical results showed that for the second pipe section (S2), pressure and momentum flux as coupling constants yielded fundamentally different wave solutions as pressure yielded two rarefaction waves and momentum flux yielded two shock waves. By applying the same energy evaluation as in the previous paper [45], the numerical results from both models were seen to be unphysical. Bernoulli invariant yielded a physical solution and predicted two rarefaction waves to enter the second pipe section.

My contribution In general, this paper was developed and written by me, with helpful suggestions from Tore Flåtten.

5.5. Paper V - Existence and Uniqueness of Solutions to the Generalized Riemann Problem for Isentropic Flow

Author: Gunhild A. Reigstad
To be submitted

The solutions to network models that are based on the isentropic Euler equations were investigated in this paper. The analysis was based upon the results in paper II and III and considered the application of the three coupling constants pressure, momentum flux and Bernoulli invariant. For monotone momentum related coupling constants and subsonic initial conditions, subsonic solutions to the generalized Riemann problem were proved to be unique. The region where subsonic initial conditions yield subsonic solutions was also identified. Further, pressure, momentum flux and Bernoulli invariant were shown to be monotone.

As for network models based on the isothermal Euler equations, the entropy condition applied for isentropic flows states that unphysical solutions are characterised by energy production in a junction. In the present paper, the relevant expression was derived from the isentropic Euler equations. Further, the condition was applied in an investigation of the presence of entropic solutions for the three different models. It was proved that network models which use Bernoulli invariant as momentum related coupling

constant conserves energy at a junction in the general case of N connected pipe sections of different cross-sectional area.

A test case consisting of three pipe sections of equal cross-sectional area connected at a junction was used to show that pressure yields unphysical solutions whenever there are two incoming flows and one outgoing flow. This is identical to what was shown for the same test case when the isothermal Euler equations was applied as conservation law. For momentum flux as coupling constant, a single set of subsonic initial conditions were provided for the same test case. The corresponding solution was shown to be unphysical.

It was therefore concluded that for network models based on the isentropic Euler equations, only Bernoulli invariant yields physically sound solutions for all subsonic flow conditions.

My contribution The paper was mainly derived and written by me. Tore Flåtten provided the proofs in Lemma 4 and Lemma 5, and introduced their application in Lemma 7 and Lemma 8.

Further work Before the paper is submitted, it is the aim to extend the analysis of physically sound solutions for momentum flux as coupling constant such that ranges of subsonic solutions are considered, rather than a single set.

"Kant, discussing the various modes of perception by which the human mind apprehends nature, concluded that it is specially prone to see nature through mathematical spectacles. Just as a man wearing blue spectacles would see only a blue world, so Kant thought that, with our mental bias, we tend to see only a mathematical world."

Sir James Jeans

6 Conclusions and Outlook

This thesis has considered the mathematical description of fluid flow in junctions that connect two or more pipe sections, also known as network models. The work has mainly focused on models derived for the isothermal Euler equations and for the isentropic Euler equations.

Both an analytic and a numerical approach have been applied. In the numerical implementation, the approximate Riemann solver of Roe was used to calculate the fluid flow within each pipe section. The results of an improved Roe solver for the drift-flux model has thus as well been reported, as a first step towards numerical simulations on network models based on the drift-flux formulation.

In the following, the main observations on network models for the isentropic and isothermal Euler equations will be given. This will be followed by an outlook on future work.

6.1. Conclusions

The main focus of the present work has been the proper selection of the momentum related coupling constant expression. This is the second coupling condition used in the considered network models, and it is needed in order to close the set of equations. The first condition describes conservation of mass at the junction. A literature survey showed that both momentum

flux and pressure were commonly used as coupling constant. In the present work, Bernoulli invariant was launched as an alternative.

The performed investigation has mainly concerned the existence and uniqueness of solutions and the existence of physically sound solutions within the subsonic region. Sets of initial conditions that belong to this region are subsonic and have subsonic solutions. The establishment of a general numerical implementation of network models has also been an important task.

A theoretical analysis on the isothermal Euler equations revealed three conditions on the momentum related coupling constant:

1. $\mathcal{H}(\rho, \rho v)$ must be a monotone function of ρ for ρv constant
2. $\mathcal{H}(\rho, \rho v)$ must be a symmetric function of ρv, that is $\mathcal{H}(\rho, \rho v) = \mathcal{H}(\rho, -\rho v)$
3. In the subsonic region, $\mathcal{H}_k^*(\rho_k^*; \bar{\rho}_k, \bar{v}_k)$ should be a monotone coupling constant, that is, a monotone function of ρ_k^*

The two first conditions are mandatory if the network model is to predict the analytical solution of the standard Riemann problem. Note that the notation of the coupling constant used here is only used in this context. In general, the constant is expressed as $\mathcal{H}(\rho, v)$.

In the present work, uniqueness of solutions has been proved for momentum related coupling constants that are monotone and hence fulfils the third condition. The coupling constant of this condition is expressed as a function of density alone. Alternatively it may be expressed as a function of the velocity or Mach number alone. The expression includes the wave equation that relates the density of the constructed state, ρ^*, to the corresponding velocity, v^*, and the initial condition in the pipe section, $(\bar{\rho}, \bar{v})$. The proof is only valid for sets of initial conditions that belong to the subsonic region.

The investigation showed that the three constants, pressure, momentum flux and Bernoulli invariant all fulfil the three conditions.

The existence of solutions was proved by showing the existence of a unique solution to the mass conservation constraint (3.109) within the range of coupling constant values that would yield subsonic solutions in all connected pipe sections. Sets of initial conditions, for which there does not exist such a solution, will have a sonic or supersonic solution in at least one pipe section. Such a set of initial conditions does therefore not belong to the subsonic region.

As a result, existence and uniqueness have been proved for network models that apply pressure, momentum flux or Bernoulli invariant as momentum

related coupling constant, for sets of initial conditions that belong to the subsonic region.

An entropy condition commonly applied in the literature, was used in order to eliminate unphysical solutions and thus to investigate the existence of physical solutions within the entire subsonic region. The condition states that unphysical solutions are characterised by the presence of energy production in a junction. An analysis was performed for a junction that connects three pipe sections of equal cross-sectional area. The results showed that neither pressure nor momentum flux as coupling constant yields physically sound solutions for all subsonic flow conditions at the pipe-junction interfaces. In particular, a duality was observed. In the flow range where pressure yields physical solutions, momentum flux yields unphysical solutions, and opposite. Bernoulli invariant was proved to yield physical solutions in the general case of a junction that connects N pipe sections of different cross-sectional area.

The Bernoulli invariant was suggested as momentum related coupling constant since it is constant along a streamline. As the flow in each pipe section is modelled as ideal, by neglecting friction and heat conduction, the goal has been to model junction flow as ideal too. Consequently, the flow should be characterised by uninterrupted streamlines. The invariant may as well be assumed to contain some of the information of the three-dimensional momentum conservation, which describes the junction flow. This is due to the fact that it is found from the equation for conservation of mechanical energy in smooth flows, an equation which may be derived from the three-dimensional momentum conservation law together with the equation describing conservation of mass.

The numerical implementation was performed in order to derive a general implementation of network models, where an arbitrary numerical scheme may be applied for the flow within each pipe section. It was found that special care had to be taken in order to ensure numerical conservation of mass at the junction. In the present work this was achieved by applying the Godunov flux at the pipe-junction interface.

The theoretical description of junction flows is a fairly new field, and so there seems to be no standard benchmark test cases. Hence, in the present work three different network layouts were established and numerical results have been provided for six different test cases. The physical soundness of all the solutions has been evaluated by means of the entropy condition. It was found that all the numerical test case results supported the conclusion of the theoretical analysis; that only Bernoulli invariant as momentum related

coupling constant yields physical solutions for all sets of initial data that belong to the subsonic region.

Network models based on the isentropic Euler equations were analytically investigated in a similar manner as for isothermal flow. First, without considering the physical validity, proofs of the existence and uniqueness of solutions were derived. As for isothermal flow, the proofs are restricted to monotone momentum related coupling constants and sets of initial conditions that belong to the subsonic region. Further, it was proved that the three alternative coupling constants; pressure, momentum flux and Bernoulli invariant, all fulfil the monotonicity constraint.

Second, the entropy condition was applied in an investigation of the physical validity of the solutions. For Bernoulli invariant it was proved that the corresponding network model conserves energy at the junction. Its solutions are therefore physically sound for all subsonic flow conditions at the pipe-junction interfaces.

The test case consisting of three pipe sections of equal cross-sectional area connected at a junction was used to investigate the network models that include pressure and momentum flux as coupling constants, respectively. For pressure, the network model was seen to have unphysical solutions whenever there are two incoming and one outgoing flow. For momentum flux, a set of initial conditions that belongs to the subsonic region was provided. The corresponding solution was seen to be unphysical.

It may therefore be concluded that Bernoulli invariant is the only momentum related coupling constant which yields physical solutions for all sets of initial conditions that belong to the subsonic region. The conclusion is valid for network models based on the isothermal and the isentropic Euler equations, respectively.

6.2. Outlook

Network models applicable for heat exchanger flow calculations demand features not yet derived. The relevant conservation law for such a numerical model will consist of at least three equations, and in general analytic wave equations and eigenvalues will not be available. This introduces at least two challenges:

1. The solution of a standard Riemann problem consists of as many waves as there are equations in the conservation law. That is, three or more

waves. This means that the constructed state and the initial condition must be connected by two or more waves in at least one of the pipe sections connected at the junction. It is important to obtain a good understanding of which pipe sections that should be modelled in this manner. Primarily it will have a direct consequence for the assumptions made about the physical principles of the flow. However, it also affects the number of coupling conditions needed to obtain a closed system. In some cases it seems necessary to add an additional coupling condition for pipe sections with outgoing flow.

2. With no analytic wave equations, a fully numerical approach is needed. That is, an entirely numerical procedure for the calculation of the constructed states must be developed.

A suitable development path could be to first derive a well understood network model for the one dimensional Euler equations accounting for mass, momentum and energy. For this conservation law, the challenges related to the wave composition stated above is valid since the wave of the second family may have positive or negative speed at subsonic conditions. Hence it is not obvious which pipe sections that should have their constructed and initial states connected by waves of the second and third wave families and which that should have waves of the third family only. The needed investigation of the physical principles that apply will hopefully be applicable to more complex conservation laws as well.

We are also in need of a fully numerical procedure for junction-pipe boundary calculations and it seems suitable to perform the first derivation for the Euler equations. Corresponding numerical results may then be compared to analytically based boundary conditions. The derived numerical procedure could then be extended to network calculations where analytic wave equations are not available.

Bibliography

[1] Mapundi K. Banda and Michael Herty. Towards a space mapping approach to dynamic compressor optimization of gas networks. *Optimal control applications and methods*, 32:253–269, 2011.

[2] Mapundi K. Banda, Michael Herty, and Axel Klar. Gas flow in pipeline networks. *Networks and heterogeneous media*, 1(1):41–56, 2006.

[3] Mapundi K. Banda, Michael Herty, and Axel Klar. Coupling conditions for gas networks governed by the isothermal euler equations. *Networks and heterogeneous media*, 1(2):295–314, 2006.

[4] Mapundi K. Banda, Michael Herty, and Jean-Medard T. Ngnotchouye. Towards a mathematical analysis for drift-flux multiphase flow models in networks. *SIAM J. Sci. Computing*, 31(6):4633–4653, 2010.

[5] Mapundi K. Banda, Michael Herty, and Jean-Medard T. Ngnotchouye. Coupling drift-flux models with unequal sonic speeds. *Mathematical and Computational Applications*, 15(4):574–584, 2010.

[6] Benjamin Boutine, Christophe Chalons, and Pierre-Arnaud Raviart. Existence result for the coupling problem of two scalar conservation laws with riemann initial data. *Mathematical Models and Methods in Applied Sciences*, 20(10):1859–1898, 2010.

[7] Jens Brouwer, Ingenuin Gasser, and Michael Herty. Gas pipeline models revisited: model hierarchies, nonisothermal models, and simulations of networks. *Multiscale Model. Simul.*, 9(2):601–623, 2011.

[8] Jr C. H. Edwards and David E. Penney. *Elementarly linear algebra.* PRENTICE HALL, 1988.

[9] David Chalet and Pascal Chesse. Fluid dynamic modeling of junctions in internal combustion engine inlet and exhaust systems. *Journal of Thermal Science*, 19(5):410–418, 2010.

[10] Christophe Chalons, Pierre-Arnaud Raviart, and Nicolas Seguin. The interface coupling of the gas dynamics equations. *Quarterly of applied mathematics*, 66(4):659–705, 2008.

[11] Bernardo Cockburn, Claes Johnson, Chi-Wang Shu, and Eitan Tadmor. *Advanced Numerical Approximation of Nonlinear Hyperbolic Equations*. Springer, 1998. ISBN 3-540-64977-8.

[12] R. M. Colombo, M. Herty, and V. Sachers. On 2×2 conservation laws at a junction. *SIAM J. Math. Anal.*, 40(2):605–622, 2008.

[13] Rinaldo M. Colombo and Mauro Garavello. A well posed Riemann problem for the p-system at a junction. *Networks and heterogeneous media*, 1(3):495 – 511, 2006.

[14] Rinaldo M. Colombo and Mauro Garavello. On the cauchy problem for the p-system at a junction. *SIAM J. Math. Anal.*, 39(5):1456–1471, 2008.

[15] Rinaldo M. Colombo and Francesca Marcellini. Coupling conditions for the 3×3 euler system. *Networks and heterogeneous media*, 5(4): 675–690, 2010.

[16] Rinaldo M. Colombo and Cristina Mauri. Euler system for compressible fluids at a junction. *Journal of Hyperbolic Differential Equations*, 5(3): 547–568, 2008.

[17] Constantine M. Dafermos. *Hyperbolic conservation laws in continuum physics*. Springer, 3 edition, 2010.

[18] Steinar Evje and Tore Flåtten. On the wave structure of two-phase flow models. *SIAM Journal on Applied Mathematics*, 67(2):487–511, 2007.

[19] Tore Flåtten and Svend Tollak Munkejord. The approximate Riemann solver of Roe applied to a drift-flux two-phase flow model. *ESAIM Mathematical Modelling and Numerical Analysis*, 40:735–764, 2006.

[20] M. Garavello. A review of conservation laws on networks. *Networks and heterogeneous media*, 5(3):565–581, 2010.

[21] G. P. Greyvenstein. An implicit method for the analysis of transient flows in pipe networks. *International Journal for Numerical Methods in Engineering*, 53:1127–1143, 2002.

[22] M. Herty, J. Mohring, and V. Sachers. A new model for gas flow in pipe networks. *Mathematical Methods in the Applied Sciences*, 33(7): 845–855, 2010.

[23] Michael Herty. Coupling conditions for networked systems of Euler equations. *SIAM J. Sci. Comput.*, 30(3):1596–1612, 2008.

[24] Michael Herty and Mohammed Seaïd. Simulation of transient gas flow at pipe-to-pipe intersections. *International Journal for Numerical Methods in Fluids*, 56:485–506, 2008.

[25] Helge Holden and Nils Henrik Risebro. A mathematical model of traffic flow on a network of unidirectional roads. *SIAM Journal on Mathematical Analysis*, 26(4):999–1017, July 1995.

[26] Helge Holden and Nils Henrik Risebro. *Front tracking for hyperbolic conservation laws*. Springer, 2 edition, 2007.

[27] Seok Woo Hong and Chongam Kim. A new finite volume method on junction coupling and boundary treatment for flow network system analyses. *International journal for numerical methods in fluids*, 65: 707–742, 2011.

[28] Ji-Hyun Hwang, Myung-Il Roh, and Kyu-Yeul Lee. Determination of the optimal operating conditions of the dual mixed refrigerant cycle for the LNG FPSO topside liquefaction process. *Computers and Chemical Engineering*, 49:25–36, 2013.

[29] S. Kakac and B. Bon. A review of two-phase flow dynamic instabilities in tube boiling systems. *International journal of heat and mass transfer*, 51:399–433, 2008.

[30] Tatsuhiko Kiuchi. An implicit method for transient gas flows in pipe networks. *Int. J. Heat and Fluid Flow*, 15(5):378–383, 1994.

[31] Randall J. LeVeque. *Finite volume methods for hyperbolic problems*. Cambridge University Press, 6 edition, 2007.

[32] H. W. Liepmann and A. Roshko. *Elements of gasdynamics*. John Wiley & Sons, Inc., 4 edition, July 1962.

[33] Dionissios P. Margaris. T-junction separation modelling in gas-liquid two-phase flow. *Chemical engineering and processing*, 46(2):150–158, 2007.

[34] Eduard Marušić-Paloka. Fluid flow through a network of thin pipes. *Comptes Rendus de l'Académie des Sciences - Series {IIB} - Mechanics*, 329(2):103 – 108, 2001.

[35] Michael J. Moran and Howard N. Shapiro. *Fundamentals of Engineering Thermodynamics*. John Wiley & Sons Ltd, 3 edition, 1998. SI version.

[36] Hessamedin Naeimi, Davood Domiry Ganji, Mofid Gorji, Ghasem Javadirad, and Mojtaba Keshavarz. A parametric design of compact exhaust manifold junction in heavy duty diesel engine using computational fluid dynamics codes. *Thermal Science*, 15(4):1023–1033, 2011.

[37] V.S. Naik-Nimbalkar, A.W. Patwardhan, I. Banerjee, G. Padmakumar, and G. Vaidyanathan. Thermal mixing in t-junctions. *Chemical Engineering Science*, 65(22):5901 – 5911, 2010.

[38] Shahrooz Abbasi Nezhad, Bezhan Shabani, and Majid Soleimani. Thermodynamic analysis of liquefied natural gas (LNG) production cycle in apci process. *Journal of Thermal Sciences*, 21(6):564–571, 2012.

[39] Jean Medard Tchoukouegno Ngnotchouye. *Conservation laws models in networks and multiscale flow optimization*. PhD thesis, University of Kwazulu-Natal, 2011.

[40] A. Osiadacz. Simulation of transient gas flows in networks. *International journal for numerical methods in fluids*, 4:13–24, 1984.

[41] R. J. Pearson, M. D. Bassett, P. Batten, and D. E. Winterbone. Two-dimensional simulation of wave propagation in a three-pipe junction. *J. Eng. Gas Turbines Power*, 122(4):549–555, October 2000.

[42] J. Pérez-García, E. Sanmiguel-Rojas, J. Hernández-Grau, and A. Viedma. Numerical and experimental investigations on internal compressible flow at T-type junctions. *Experimental Thermal and Fluid Science*, 31:61–74, 2006.

[43] J. Pérez-García, E. Sanmiguel-Rojas, and A. Viedma. New coefficient to characterize energy losses in compressible flow at t-junctions. *Applied Mathematical Modelling*, 34(12):4289 – 4305, 2010.

[44] Jostein Pettersen, Arne M. Bredesen, and Petter Nekså. Research on natural gas liquefaction technology for the Hammmerfest LNG plant. In *Cryogenics and Refrigeration, Proceedings of ICCR'2008*, pages 43–51. Science Press Beijing, 2008.

[45] Gunhild A. Reigstad. Numerical netwok models and entropy principles for isothermal junction flow. *Accepted by Networks and Heterogeneous Media*, 2013.

[46] Gunhild A. Reigstad and Tore Flåtten. An improved Roe solver for the drift-flux two-phase flow model. In *8th International Conference on CFD in Oil & Gas, Metallurgical and Process Industries*, number CFD11-129. SINTEF/NTNU, Trondheim, Norway, June 2011.

[47] Matthieu Rolland, Béatrice Fischer, Gilles Ferschneider, and Thierry Gauthier. Modelling of the fluid distribution in a parallel PFHE arrangement for the Liquefin LNG process. In *Compact Heat Exchangers and Enhancement Technology for the Process Industries*, pages 453–459. Begell House, 2003. Proceedings of the Fourth International Conference on Compact Heat Exchangers and Enhancement Technology for the Process Industries.

[48] Nematollah Saba and Richard T Lahey, Jr. The analysis of phase separation phenomena in branching conduits. *International Journal of Multiphase Flow*, 10(1):1 – 20, 1983.

[49] Scott A. Sarra. The Method of Characteristics & Conservation Laws. *Journal of Online Mathematics and its Applications*, 2003. URL `http://www.maa.org/node/115396`.

[50] G. Skaugen, G. A. Gjøvåg, P. Nekså, and P. E. Wahl. Use of sophisticated heat exchanger simulation models for investigation of possible design and operational pitfalls in LNG processes. *Journal of Natural Gas Science and Engineering*, 2(5):235–243, 2010.

[51] Pavel Ŝolin. *Partiel Differential Equations and the Finite Element Method*. John Wiley & Sons, Inc, 2006.

[52] Eitan Tadmor. Entropy functions for symmetric systems of conservation laws. *Journal of mathematical analysis and applications*, 122: 355–359, 1987.

[53] Eleuterio F. Toro. *Riemann sovers and numerical methods for fluid dynamics*. Springer, 3 edition, 2009.

[54] Sivert Vist. Two-phase flow distribution in heat exchanger manifolds. Dr.ing-thesis 2004:01, Norwegian University of Science and Technology, NTNU, 2004.

[55] C. Walker, A. Manera, B. Niceno, M. Simiano, and H.-M. Prasser. Steady-state rans-simulations of the mixing in a t-junction. *Nuclear Engineering and Design*, 240(9):2107 – 2115, 2010.

[56] M J P William-Louis, A Ould-El-Hadrami, and C Tournier. On the calculation of the unsteady compressible flow through an n-branch junction. *Proceedings of the Institution of Mechanical Engineers, Part C: Journal of Mechanical Engineering Science*, 212(1):49–56, 1998.

A

Calculation of shock wave relations

In Section 3.1.3, the Rankine-Hugoniot condition (3.45) was used to derive a relation between the left and the right states of a shock wave

$$v_{\mathcal{R}} = v_{\mathcal{L}} \pm \sqrt{\frac{k\left(\rho_{\mathcal{R}} - \rho_{\mathcal{L}}\right)\left(\rho_{\mathcal{R}}^{\gamma} - \rho_{\mathcal{L}}^{\gamma}\right)}{\rho_{\mathcal{R}}\rho_{\mathcal{L}}}}. \tag{A.1}$$

The corresponding wave speed may be written as

$$s = v_{\mathcal{L}} \pm \frac{1}{\left(\rho_{\mathcal{R}} - \rho_{\mathcal{L}}\right)} \sqrt{\frac{\rho_{\mathcal{R}}}{\rho_{\mathcal{L}}} k\left(\rho_{\mathcal{R}} - \rho_{\mathcal{L}}\right)\left(\rho_{\mathcal{R}}^{\gamma} - \rho_{\mathcal{L}}^{\gamma}\right)}. \tag{A.2}$$

For each wave family, $j = \{1, 2\}$, one of the following combinations is correct

a) $(\rho_{\mathcal{R}} - \rho_{\mathcal{L}}) > 0$ and $+$

b) $(\rho_{\mathcal{R}} - \rho_{\mathcal{L}}) > 0$ and $-$

c) $(\rho_{\mathcal{R}} - \rho_{\mathcal{L}}) < 0$ and $+$

d) $(\rho_{\mathcal{R}} - \rho_{\mathcal{L}}) < 0$ and $-$

Here $+$ and $-$ refer to the sign within (A.1) and (A.2).

The correct combination is identified as being the only combination that satisfies one of the inequalities of the Lax entropy conditions (3.51)

$$\lambda_j \left(\boldsymbol{U}_{\mathcal{R}} \right) < s_j < \lambda_j \left(\boldsymbol{U}_{\mathcal{L}} \right). \tag{A.3}$$

In the following, the calculations which lead to the conclusions presented in Section 3.1.3 will be shown. Two lemmas that are presented in Paper V (Appendix F) will be important in these calculations. Thus, for the completeness of this appendix, we will re-state them first.

Lemma 1. *Consider* $x \in \langle 0, 1 \rangle$ *and* $\gamma > 1$. *Then*

$$\frac{\gamma}{1 - x^{\gamma}} \geq \frac{1}{1 - x}. \tag{A.4}$$

Proof. Consider the function

$$q\left(x, \gamma\right) = \frac{1}{\gamma} \left(1 - x^{\gamma}\right). \tag{A.5}$$

Then

$$q\left(1, \gamma\right) = 0 \tag{A.6}$$

and

$$q'\left(x, \gamma\right) = -x^{\gamma - 1}. \tag{A.7}$$

It then follows from the Taylor's formula that

$$q\left(x, \gamma\right) = q\left(1, \gamma\right) + q'\left(z, \gamma\right)\left(x - 1\right), \tag{A.8}$$

for some number $z \in \langle x, 1 \rangle$. Hence

$$q\left(x, \gamma\right) = z^{\gamma - 1}\left(1 - x\right) \leq 1 - x, \tag{A.9}$$

which proves (A.4). □

Lemma 2. *Consider* $x \in \langle 0, 1 \rangle$ *and* $\gamma > 1$. *Then*

$$\frac{x^{-\gamma} - 1}{\gamma} \geq \frac{1}{x} - 1. \tag{A.10}$$

Proof. Consider the function

$$q\left(u, \gamma\right) = u^{\gamma} - 1, \tag{A.11}$$

where

$$u = \frac{1}{x}. \tag{A.12}$$

Then

$$q\left(1, \gamma\right) = 0 \tag{A.13}$$

and

$$q'\left(u, \gamma\right) = \gamma u^{\gamma - 1}. \tag{A.14}$$

It then follows from the Taylor's formula that

$$q\left(u, \gamma\right) = q\left(1, \gamma\right) + q'\left(z, \gamma\right)\left(u - 1\right), \tag{A.15}$$

for some number $z \in \langle 1, u \rangle$. Hence

$$q\left(u, \gamma\right) = \gamma z^{\gamma - 1}\left(u - 1\right) \geq \gamma\left(u - 1\right). \tag{A.16}$$

Insertion of (A.12) into (A.16) proves (A.10). □

Then we continue by considering a shock wave of the first family.

A.1. Shock waves of the first family

When the wave is of the first family, Equation (A.3) becomes

$$v_{\mathcal{R}} - \sqrt{k\gamma\rho_{\mathcal{R}}^{\gamma-1}} < v_{\mathcal{L}} \pm \frac{1}{\left(\rho_{\mathcal{R}} - \rho_{\mathcal{L}}\right)}\sqrt{\frac{\rho_{\mathcal{R}}}{\rho_{\mathcal{L}}} k\left(\rho_{\mathcal{R}} - \rho_{\mathcal{L}}\right)\left(\rho_{\mathcal{R}}^{\gamma} - \rho_{\mathcal{L}}^{\gamma}\right)} < v_{\mathcal{L}} - \sqrt{k\gamma\rho_{\mathcal{L}}^{\gamma-1}}. \tag{A.17}$$

From previous experience, we consider the second inequality

$$\pm \frac{1}{\left(\rho_{\mathcal{R}} - \rho_{\mathcal{L}}\right)}\sqrt{\frac{\rho_{\mathcal{R}}}{\rho_{\mathcal{L}}} k\left(\rho_{\mathcal{R}} - \rho_{\mathcal{L}}\right)\left(\rho_{\mathcal{R}}^{\gamma} - \rho_{\mathcal{L}}^{\gamma}\right)} < -\sqrt{k\gamma\rho_{\mathcal{L}}^{\gamma-1}}. \tag{A.18}$$

It is obvious that the combinations a) and d) violate the inequality. Hence, they are not considered further.

Combination 1b) For this combination, we have

$$\begin{aligned}
-\frac{1}{(\rho_{\mathcal{R}}-\rho_{\mathcal{L}})}\sqrt{\frac{\rho_{\mathcal{R}}}{\rho_{\mathcal{L}}}k\left(\rho_{\mathcal{R}}-\rho_{\mathcal{L}}\right)\left(\rho_{\mathcal{R}}^{\gamma}-\rho_{\mathcal{L}}^{\gamma}\right)} &< -\sqrt{k\gamma\rho_{\mathcal{L}}^{\gamma-1}},\\
\frac{1}{(\rho_{\mathcal{R}}-\rho_{\mathcal{L}})}\sqrt{\frac{\rho_{\mathcal{R}}}{\rho_{\mathcal{L}}}k\left(\rho_{\mathcal{R}}-\rho_{\mathcal{L}}\right)\left(\rho_{\mathcal{R}}^{\gamma}-\rho_{\mathcal{L}}^{\gamma}\right)} &> \sqrt{k\gamma\rho_{\mathcal{L}}^{\gamma-1}},\\
\sqrt{\frac{\rho_{\mathcal{R}}}{\rho_{\mathcal{L}}}k\frac{\left(\rho_{\mathcal{R}}^{\gamma}-\rho_{\mathcal{L}}^{\gamma}\right)}{\left(\rho_{\mathcal{R}}-\rho_{\mathcal{L}}\right)}} &> \sqrt{k\gamma\rho_{\mathcal{L}}^{\gamma-1}},\\
\sqrt{\frac{\left(\left(\frac{\rho_{\mathcal{R}}}{\rho_{\mathcal{L}}}\right)^{\gamma}-1\right)}{1-\frac{\rho_{\mathcal{L}}}{\rho_{\mathcal{R}}}}} &> \sqrt{\gamma}.
\end{aligned} \tag{A.19}$$

Since $\rho_{\mathcal{R}} > \rho_{\mathcal{L}}$, we set

$$x_{1b} = \frac{\rho_{\mathcal{L}}}{\rho_{\mathcal{R}}}, \quad x_{1b} \in \langle 0, 1\rangle. \tag{A.20}$$

Consequently, the inequality may be written as

$$\sqrt{\frac{1}{x_{1b}\left(\frac{1}{x_{1b}}-1\right)}} > \sqrt{\frac{\gamma}{\left(\frac{1}{x_{1b}}\right)^{\gamma}-1}}. \tag{A.21}$$

From Lemma 2 we have that

$$\frac{\gamma}{x_{1b}^{-\gamma}-1} \leq \frac{1}{\frac{1}{x_{1b}}-1}. \tag{A.22}$$

Thus since

$$\sqrt{\frac{1}{x_{1b}}} > 1, \tag{A.23}$$

$$\sqrt{\frac{\gamma}{x_{1b}^{-\gamma}-1}} \leq \sqrt{\frac{1}{\frac{1}{x_{1b}}-1}} < \sqrt{\frac{1}{\frac{1}{x_{1b}}-1}}\sqrt{\frac{1}{x_{1b}}}. \tag{A.24}$$

This proves that (A.21) holds.

Combination 1c) For this combination, we have

$$\begin{aligned}
\frac{1}{(\rho_{\mathcal{R}}-\rho_{\mathcal{L}})}\sqrt{\frac{\rho_{\mathcal{R}}}{\rho_{\mathcal{L}}}k\,(\rho_{\mathcal{L}}-\rho_{\mathcal{R}})\,(\rho_{\mathcal{L}}^{\gamma}-\rho_{\mathcal{R}}^{\gamma})} &< -\sqrt{k\gamma\rho_{\mathcal{L}}^{\gamma-1}},\\
\frac{1}{(\rho_{\mathcal{L}}-\rho_{\mathcal{R}})}\sqrt{\frac{\rho_{\mathcal{R}}}{\rho_{\mathcal{L}}}k\,(\rho_{\mathcal{L}}-\rho_{\mathcal{R}})\,(\rho_{\mathcal{L}}^{\gamma}-\rho_{\mathcal{R}}^{\gamma})} &> \sqrt{k\gamma\rho_{\mathcal{L}}^{\gamma-1}},\\
\sqrt{\frac{\rho_{\mathcal{R}}}{\rho_{\mathcal{L}}}k\frac{(\rho_{\mathcal{L}}^{\gamma}-\rho_{\mathcal{R}}^{\gamma})}{(\rho_{\mathcal{L}}-\rho_{\mathcal{R}})}} &> \sqrt{k\gamma\rho_{\mathcal{L}}^{\gamma-1}},\\
\sqrt{\frac{\left(1-\left(\frac{\rho_{\mathcal{R}}}{\rho_{\mathcal{L}}}\right)^{\gamma}\right)}{\frac{\rho_{\mathcal{L}}}{\rho_{\mathcal{R}}}-1}} &> \sqrt{\gamma}.
\end{aligned} \tag{A.25}$$

As $\rho_{\mathcal{L}} > \rho_{\mathcal{R}}$, we denote

$$x_{1c} = \frac{\rho_{\mathcal{R}}}{\rho_{\mathcal{L}}}, \quad x_{1c} \in \langle 0, 1\rangle, \tag{A.26}$$

such that the inequality may be written as

$$\sqrt{\frac{1-x_{1c}^{\gamma}}{\gamma}} > \sqrt{\frac{1}{x_{1c}}\,(1-x_{1c})}. \tag{A.27}$$

Since

$$\sqrt{\frac{1}{x_{1c}}} > 1, \tag{A.28}$$

we have that

$$\sqrt{\frac{1-x_{1c}^{\gamma}}{\gamma}} > \sqrt{\frac{1}{x_{1c}}\,(1-x_{1c})} > \sqrt{1-x_{1c}}. \tag{A.29}$$

This clearly contradicts Lemma 1, which states that

$$\frac{1}{\gamma}\,(1-x_{1c}^{\gamma}) \leq 1-x_{1c}. \tag{A.30}$$

Conclusion Combination b) is the only possible solution for a shock wave of the first family. Hence

$$v_{\mathcal{R}} = v_{\mathcal{L}} - \sqrt{\frac{k\,(\rho_{\mathcal{R}}-\rho_{\mathcal{L}})\,(\rho_{\mathcal{R}}^{\gamma}-\rho_{\mathcal{L}}^{\gamma})}{\rho_{\mathcal{R}}\rho_{\mathcal{L}}}}, \quad \rho_{\mathcal{R}} > \rho_{\mathcal{L}} \tag{A.31}$$

and

$$s_1 = v_{\mathcal{L}} - \frac{1}{(\rho_{\mathcal{R}}-\rho_{\mathcal{L}})}\sqrt{\frac{\rho_{\mathcal{R}}}{\rho_{\mathcal{L}}}k\,(\rho_{\mathcal{R}}-\rho_{\mathcal{L}})\,(\rho_{\mathcal{R}}^{\gamma}-\rho_{\mathcal{L}}^{\gamma})}. \tag{A.32}$$

A.2. Shock waves of the second family

When the wave is of the second family, Equation (A.3) becomes

$$v_{\mathcal{R}}+\sqrt{k\gamma\rho_{\mathcal{R}}^{\gamma-1}} < v_{\mathcal{L}}\pm\frac{1}{(\rho_{\mathcal{R}}-\rho_{\mathcal{L}})}\sqrt{\frac{\rho_{\mathcal{R}}}{\rho_{\mathcal{L}}}k\,(\rho_{\mathcal{R}}-\rho_{\mathcal{L}})\,(\rho_{\mathcal{R}}^{\gamma}-\rho_{\mathcal{L}}^{\gamma})} < v_{\mathcal{L}}+\sqrt{k\gamma\rho_{\mathcal{L}}^{\gamma-1}}. \tag{A.33}$$

From experience, we consider the first inequality

$$v_{\mathcal{L}} \pm \sqrt{\frac{k\,(\rho_{\mathcal{R}}-\rho_{\mathcal{L}})\,(\rho_{\mathcal{R}}^{\gamma}-\rho_{\mathcal{L}}^{\gamma})}{\rho_{\mathcal{R}}\rho_{\mathcal{L}}}} + \sqrt{k\gamma\rho_{\mathcal{R}}^{\gamma-1}} < v_{\mathcal{L}} \pm \frac{1}{(\rho_{\mathcal{R}}-\rho_{\mathcal{L}})}\sqrt{\frac{\rho_{\mathcal{R}}}{\rho_{\mathcal{L}}}k\,(\rho_{\mathcal{R}}-\rho_{\mathcal{L}})\,(\rho_{\mathcal{R}}^{\gamma}-\rho_{\mathcal{L}}^{\gamma})}, \tag{A.34}$$

or, simplified

$$\sqrt{k\gamma\rho_{\mathcal{R}}^{\gamma-1}} \pm \sqrt{\frac{k\,(\rho_{\mathcal{R}}-\rho_{\mathcal{L}})\,(\rho_{\mathcal{R}}^{\gamma}-\rho_{\mathcal{L}}^{\gamma})}{\rho_{\mathcal{R}}\rho_{\mathcal{L}}}} < \pm\frac{1}{(\rho_{\mathcal{R}}-\rho_{\mathcal{L}})}\sqrt{\frac{\rho_{\mathcal{R}}}{\rho_{\mathcal{L}}}k\,(\rho_{\mathcal{R}}-\rho_{\mathcal{L}})\,(\rho_{\mathcal{R}}^{\gamma}-\rho_{\mathcal{L}}^{\gamma})}. \tag{A.35}$$

The inequality is clearly violated by combination c), and therefore this alternative is discarded.

Combination 2a) For this combination we have

$$\sqrt{k\gamma\rho_{\mathcal{R}}^{\gamma-1}}+\sqrt{\frac{k\,(\rho_{\mathcal{R}}-\rho_{\mathcal{L}})\,(\rho_{\mathcal{R}}^{\gamma}-\rho_{\mathcal{L}}^{\gamma})}{\rho_{\mathcal{R}}\rho_{\mathcal{L}}}} < \frac{1}{(\rho_{\mathcal{R}}-\rho_{\mathcal{L}})}\sqrt{\frac{\rho_{\mathcal{R}}}{\rho_{\mathcal{L}}}k\,(\rho_{\mathcal{R}}-\rho_{\mathcal{L}})\,(\rho_{\mathcal{R}}^{\gamma}-\rho_{\mathcal{L}}^{\gamma})}, \tag{A.36}$$

which may be re-formulated to

$$\begin{aligned}\sqrt{k\gamma\rho_{\mathcal{R}}^{\gamma-1}}\left(1+\sqrt{\frac{1}{\gamma}\frac{1}{\rho_{\mathcal{R}}^{\gamma}}\frac{(\rho_{\mathcal{R}}-\rho_{\mathcal{L}})\,(\rho_{\mathcal{R}}^{\gamma}-\rho_{\mathcal{L}}^{\gamma})}{\rho_{\mathcal{L}}}}\right) &< \sqrt{\frac{\rho_{\mathcal{R}}}{\rho_{\mathcal{L}}}k\frac{\rho_{\mathcal{R}}^{\gamma}-\rho_{\mathcal{L}}^{\gamma}}{\rho_{\mathcal{R}}-\rho_{\mathcal{L}}}},\\ 1+\sqrt{\frac{1}{\gamma}\left(\frac{\rho_{\mathcal{R}}}{\rho_{\mathcal{L}}}-1\right)\left(1-\left(\frac{\rho_{\mathcal{L}}}{\rho_{\mathcal{R}}}\right)^{\gamma}\right)} &< \sqrt{\frac{1}{\gamma}\frac{\rho_{\mathcal{R}}}{\rho_{\mathcal{L}}}\frac{1-\left(\frac{\rho_{\mathcal{L}}}{\rho_{\mathcal{R}}}\right)^{\gamma}}{1-\frac{\rho_{\mathcal{L}}}{\rho_{\mathcal{R}}}}}.\end{aligned} \tag{A.37}$$

Since $\rho_{\mathcal{R}} > \rho_{\mathcal{L}}$, we set

$$x_{2a} = \frac{\rho_{\mathcal{L}}}{\rho_{\mathcal{R}}}, \quad x_{2a} \in \langle 0, 1\rangle. \tag{A.38}$$

Equation (A.37) may then be written as

$$1+\sqrt{\frac{1}{\gamma}\left(\frac{1}{x_{2a}}-1\right)(1-x_{2a}^{\gamma})}<\sqrt{\frac{1}{\gamma}\frac{1}{x_{2a}}\frac{1-x_{2a}^{\gamma}}{1-x_{2a}}}. \tag{A.39}$$

Further simplifications gives

$$\begin{aligned}\sqrt{\frac{1}{\gamma}\frac{1-x_{2a}^{\gamma}}{x_{2a}}}\left(\sqrt{\frac{1}{1-x_{2a}}}-\sqrt{1-x_{2a}}\right)>&1,\\ \sqrt{\frac{1}{\gamma}(1-x_{2a}^{\gamma})}>&\sqrt{\frac{1-x_{2a}}{x_{2a}}}.\end{aligned} \tag{A.40}$$

As

$$\sqrt{\frac{1}{x_{2a}}}>1, \tag{A.41}$$

we have that combination a) is feasible if

$$\sqrt{\frac{1}{\gamma}(1-x_{2a}^{\gamma})}>\sqrt{\frac{1-x_{2a}}{x_{2a}}}>\sqrt{1-x_{2a}}. \tag{A.42}$$

However, this contradicts Lemma 1, which states that

$$\sqrt{\frac{1}{\gamma}(1-x_{2a}^{\gamma})}\leq\sqrt{1-x_{2a}}. \tag{A.43}$$

Therefore, combination a) is seen to violate the inequality (A.36).

Combination 2b) For this combination we have

$$\begin{aligned}\sqrt{k\gamma\rho_{\mathcal{R}}^{\gamma-1}}-\sqrt{\frac{k(\rho_{\mathcal{R}}-\rho_{\mathcal{L}})(\rho_{\mathcal{R}}^{\gamma}-\rho_{\mathcal{L}}^{\gamma})}{\rho_{\mathcal{R}}\rho_{\mathcal{L}}}}\\ <-\frac{1}{(\rho_{\mathcal{R}}-\rho_{\mathcal{L}})}\sqrt{\frac{\rho_{\mathcal{R}}}{\rho_{\mathcal{L}}}k(\rho_{\mathcal{R}}-\rho_{\mathcal{L}})(\rho_{\mathcal{R}}^{\gamma}-\rho_{\mathcal{L}}^{\gamma})}.\end{aligned} \tag{A.44}$$

The inequality may be rewritten as

$$\begin{aligned}\sqrt{k\gamma\rho_{\mathcal{R}}^{\gamma-1}}\left(1-\sqrt{\frac{1}{\gamma}\frac{1}{\rho_{\mathcal{R}}^{\gamma}}\frac{(\rho_{\mathcal{R}}-\rho_{\mathcal{L}})(\rho_{\mathcal{R}}^{\gamma}-\rho_{\mathcal{L}}^{\gamma})}{\rho_{\mathcal{L}}}}\right)<&-\sqrt{\frac{\rho_{\mathcal{R}}}{\rho_{\mathcal{L}}}k\frac{\rho_{\mathcal{R}}^{\gamma}-\rho_{\mathcal{L}}^{\gamma}}{\rho_{\mathcal{R}}-\rho_{\mathcal{L}}}},\\ 1-\sqrt{\frac{1}{\gamma}\left(\frac{\rho_{\mathcal{R}}}{\rho_{\mathcal{L}}}-1\right)\left(1-\left(\frac{\rho_{\mathcal{L}}}{\rho_{\mathcal{R}}}\right)^{\gamma}\right)}<&-\sqrt{\frac{1}{\gamma}\frac{\rho_{\mathcal{R}}}{\rho_{\mathcal{L}}}\frac{1-\left(\frac{\rho_{\mathcal{L}}}{\rho_{\mathcal{R}}}\right)^{\gamma}}{1-\frac{\rho_{\mathcal{L}}}{\rho_{\mathcal{R}}}}}.\end{aligned} \tag{A.45}$$

Since $\rho_{\mathcal{R}} > \rho_{\mathcal{L}}$, we set

$$x_{2b} = \frac{\rho_{\mathcal{L}}}{\rho_{\mathcal{R}}}, \quad x_{2b} \in \langle 0, 1 \rangle. \tag{A.46}$$

Equation (A.45) may then be written as

$$1 - \sqrt{\frac{1}{\gamma}\left(\frac{1}{x_{2b}} - 1\right)(1 - x_{2b}^{\gamma})} < -\sqrt{\frac{1}{\gamma}\frac{1}{x_{2b}}\frac{1 - x_{2b}^{\gamma}}{1 - x_{2b}}}, \tag{A.47}$$

or, by further simplifications

$$\begin{aligned} \sqrt{\frac{1}{\gamma}\frac{1 - x_{2b}^{\gamma}}{x_{2b}}}\left(\sqrt{1 - x_{2b}} - \sqrt{\frac{1}{1 - x_{2b}}}\right) &> 1, \\ -\sqrt{\frac{x_{2b}}{\gamma}\frac{1 - x_{2b}^{\gamma}}{1 - x_{2b}}} &> 1. \end{aligned} \tag{A.48}$$

This proves that combination b) is unfeasible.

Combination 2d) For this combination we have

$$\begin{aligned} \sqrt{k\gamma\rho_{\mathcal{R}}^{\gamma-1}} - \sqrt{\frac{k\left(\rho_{\mathcal{L}} - \rho_{\mathcal{R}}\right)\left(\rho_{\mathcal{L}}^{\gamma} - \rho_{\mathcal{R}}^{\gamma}\right)}{\rho_{\mathcal{R}}\rho_{\mathcal{L}}}} \\ < -\frac{1}{\left(\rho_{\mathcal{R}} - \rho_{\mathcal{L}}\right)}\sqrt{\frac{\rho_{\mathcal{R}}}{\rho_{\mathcal{L}}}k\left(\rho_{\mathcal{L}} - \rho_{\mathcal{R}}\right)\left(\rho_{\mathcal{L}}^{\gamma} - \rho_{\mathcal{R}}^{\gamma}\right)}. \end{aligned} \tag{A.49}$$

The inequality may also be written as

$$\begin{aligned} \sqrt{k\gamma\rho_{\mathcal{R}}^{\gamma-1}}\left(1 - \sqrt{\frac{1}{\gamma\rho_{\mathcal{R}}^{\gamma}}\frac{\left(\rho_{\mathcal{L}} - \rho_{\mathcal{R}}\right)\left(\rho_{\mathcal{L}}^{\gamma} - \rho_{\mathcal{R}}^{\gamma}\right)}{\rho_{\mathcal{L}}}}\right) &< \sqrt{\frac{\rho_{\mathcal{R}}}{\rho_{\mathcal{L}}}k\frac{\rho_{\mathcal{L}}^{\gamma} - \rho_{\mathcal{R}}^{\gamma}}{\rho_{\mathcal{L}} - \rho_{\mathcal{R}}}}, \\ 1 - \sqrt{\frac{1}{\gamma}\left(1 - \frac{\rho_{\mathcal{R}}}{\rho_{\mathcal{L}}}\right)\left(\left(\frac{\rho_{\mathcal{L}}}{\rho_{\mathcal{R}}}\right)^{\gamma} - 1\right)} &< \sqrt{\frac{1}{\gamma}\frac{\rho_{\mathcal{R}}}{\rho_{\mathcal{L}}}\frac{\left(\frac{\rho_{\mathcal{L}}}{\rho_{\mathcal{R}}}\right)^{\gamma} - 1}{\frac{\rho_{\mathcal{L}}}{\rho_{\mathcal{R}}} - 1}}. \end{aligned} \tag{A.50}$$

As $\rho_{\mathcal{R}} < \rho_{\mathcal{L}}$, we set

$$x_{2d} = \frac{\rho_{\mathcal{R}}}{\rho_{\mathcal{L}}}, \quad x_{2d} \in \langle 0, 1 \rangle. \tag{A.51}$$

Equation (A.50) may then be stated as

$$1 - \sqrt{\frac{1}{\gamma}\left(1 - x_{2d}\right)\left(\left(\frac{1}{x_{2d}}\right)^{\gamma} - 1\right)} < \sqrt{\frac{1}{\gamma}x_{2d}\frac{\left(\frac{1}{x_{2d}}\right)^{\gamma} - 1}{\frac{1}{x_{2d}} - 1}}, \tag{A.52}$$

or

$$\sqrt{\frac{1}{\gamma}\left(\left(\frac{1}{x_{2d}}\right)^{\gamma}-1\right)}\left(\sqrt{(1-x_{2d})}+\sqrt{\frac{x_{2d}^2}{1-x_{2d}}}\right)-1>0. \tag{A.53}$$

From Lemma 2 we have that

$$\frac{x_{2d}^{-\gamma}-1}{\gamma}\geq\frac{1}{x_{2d}}-1. \tag{A.54}$$

Therefore

$$\begin{aligned}
&\sqrt{\frac{1}{\gamma}\left(\left(\frac{1}{x_{2d}}\right)^{\gamma}-1\right)}\left(\sqrt{(1-x_{2d})}+\sqrt{\frac{x_{2d}^2}{1-x_{2d}}}\right)-1\\
&\qquad\geq\sqrt{\left(\frac{1}{x_{2d}}-1\right)}\left(\sqrt{(1-x_{2d})}+\sqrt{\frac{x_{2d}^2}{1-x_{2d}}}\right)-1\\
&\qquad=\frac{1-\sqrt{x_{2d}}}{\sqrt{x_{2d}}}\\
&\qquad>0,\quad \text{since } x_{2d}\in\langle 0,1\rangle.
\end{aligned} \tag{A.55}$$

Therefore (A.53), and consequently (A.49), is seen to hold.

Conclusion Combination d) is the only possible solution for a shock wave of the second family. Hence

$$v_{\mathcal{R}}=v_{\mathcal{L}}-\sqrt{\frac{k\,(\rho_{\mathcal{R}}-\rho_{\mathcal{L}})\,(\rho_{\mathcal{R}}^{\gamma}-\rho_{\mathcal{L}}^{\gamma})}{\rho_{\mathcal{R}}\rho_{\mathcal{L}}}},\quad \rho_{\mathcal{R}}<\rho_{\mathcal{L}}. \tag{A.56}$$

and

$$s_2=v_{\mathcal{L}}-\frac{1}{(\rho_{\mathcal{R}}-\rho_{\mathcal{L}})}\sqrt{\frac{\rho_{\mathcal{R}}}{\rho_{\mathcal{L}}}k\,(\rho_{\mathcal{R}}-\rho_{\mathcal{L}})\,(\rho_{\mathcal{R}}^{\gamma}-\rho_{\mathcal{L}}^{\gamma})}. \tag{A.57}$$

B

Paper I - An Improved Roe Solver for the Drift-Flux Two-Phase Model

Authors: Gunhild Allard Reigstad and Tore Flåtten

Presented at the 8^{th} *International Conference on CFD in Oil & Gas, Metallurgical and Process Industries, 21-23 June 2011, Trondheim, Norway*

8th International Conference on CFD in Oil & Gas, Metallurgical and Process Industries
SINTEF/NTNU, Trondheim NORWAY
21-23 June 2011

CFD11-129

AN IMPROVED ROE SOLVER FOR THE DRIFT-FLUX TWO-PHASE FLOW MODEL

Gunhild Allard REIGSTAD[1], **Tore FLÅTTEN**[2*]

[1]NTNU Department of Energy and Process Engineering, 7491 Trondheim, NORWAY

[2]SINTEF Energy Research, 7465 Trondheim, NORWAY

* E-mail: tore.flatten@sintef.no

ABSTRACT

This paper concerns the numerical solution of a hyperbolic system of conservation laws describing two-phase flow in a pipeline. The selected model is a one dimensional drift-flux model consisting of two mass conservation equations, one momentum conservation equation and one slip function relating the velocities of each phase. The approximate Riemann solver of Roe (1981) is used due to its robustness and relative simplicity, and an improved Roe solver compared with the one shown in Flåtten and Munkejord (2006) is presented. Along with the model, some relevant numerical examples are presented to illustrate the accuracy and robustness of the method.

Keywords: Multiphase pipe flow, Drift-flux model, Roe scheme
.

NOMENCLATURE

Greek Symbols

α_k	Volume fraction, $[-]$.
β	Wave strength, $[-]$.
Δx	Grid length, $[m]$.
ε	Minimum gas volume fraction in the moving Gauss curve, $[-]$.
Φ	Slip relation, $[m/s]$.
η	Dynamic viscosity, $[Pa\,s]$.
κ	Compressibility parameter, $[m^5/kg\,s^2]$.
λ	Eigenvalue of the flux Jacobi matrix, $[m/s]$.
μ	Position of initial maximum point in the moving Gauss cuve, $[m]$.
μ_g	Partial derivative of slip relation with respect to gas volumetric mass, $[m^4/kg\,s]$.
μ_ℓ	Partial derivative of slip relation with respect to liquid volumetric mass, $[m^4/kg\,s]$.
μ_v	Partial derivative of slip relation with respect to gas phase velocity, $[-]$.
θ	Measure of the smoothness of a characteristic component of the solution, $[-]$.
ρ_k	Mass density, $[kg/m^3]$.
$\breve{\rho}$	Pseudo mass, $[kg/m^3]$.
σ	Deviation in the moving Gauss curve, $[m]$.
ζ	Partial derivative of slip relation with respect to liquid phase velocity, $[-]$.

Latin Symbols

$\boldsymbol{A}(\boldsymbol{q})$	Flux Jacobi matrix.
$\widehat{\boldsymbol{A}}_{i-1/2}$	Linearised Roe matrix.
$\mathscr{A}^{\pm}\boldsymbol{\Delta Q}_{i-1/2}$	Fluctuations.
c	Speed of sound, $[m/s]$.
$\mathscr{E}$	Measure of error in numerical calculation, $[-]$.
$\boldsymbol{f}(\boldsymbol{q})$	Vector of fluxes.
F_w	Wall friction momentum source, $[kg/m^2\,s^2]$.
$\widetilde{\boldsymbol{F}}$	Higher-order correction flux.
I_k	Volumetric momentum, $[kg/m^2\,s]$.
K	Constant used in the Zuber-Findlay slip relation, $[-]$.
m_k	Volumetric mass, $[kg/m^3]$.
n	Convergence order, $[-]$.
p	Pressure, common for both phases, $[Pa]$.
$\boldsymbol{q}$	Vector containing the conserved variables.
$\boldsymbol{Q}_i$	Vector containing the discrete conserved variables.
$\boldsymbol{r}$	Right eigenvector.
$\boldsymbol{R}$	Right eigenvector matrix.
$\boldsymbol{s}(\boldsymbol{q})$	Vector of sources.
s	Wave speed, $[m/s]$.
S	Variable used in the Zuber-Findlay slip relation, $[m/s]$.
v_k	Velocity, $[m/s]$.
$\mathscr{W}$	Wave.

Sub/superscripts

0	Indicator of reference state.
g	Gas phase.
i	Cell index.
k	Indicator of phase, l=liquid, g=gas.
ℓ	Liquid phase.
L	Grid on the left hand side of a grid interface.
p	Wave number.
R	Grid on the right hand side of a grid interface.

INTRODUCTION

The selected pipe flow model for two phase flows has many applications, including oil and gas transport, nuclear engineering, CO_2 capture and storage and the modelling of heat

exchangers. The numerical solution is obtained using an approximate Riemann solver of Roe (1981). This is a convenient upwind finite volume method due to its robustness and relative simplicity. The solver is also easily extended to second-order accuracy for smooth solutions through the wave-limiter approach of LeVeque (2007). The use of a finite volume method ensures that physically conserved variables are also numerically conserved.

The parameter vector approach suggested by Roe (1981) to obtain the solver requires a certain level of algebraic simplicity of the equation system. The slip relation and the thermodynamic closure relations in a drift-flux model generally have a complex structure which makes the approach unfeasible.

Toumi and Caruge (1998) used a weak formulation of the approximate Riemann solver of Roe in order to overcome this challenge. In this approach the Jacobian matrix is made dependent on a smooth path linking the left and right states of a grid interface in addition to the states themselves. The Roe solver was applied on a three-dimensional drift-flux model. Romate (1997) established a matrix satisfying the Roe conditions by a numerical approach . Based on an intermediate condition dependent on the left and right states, the Jacobian matrix was identified and its eigenvalues and eigenvectors were calculated. The Jacobian matrix was then represented by the eigenvector matrix, its inverse and the matrix containing the eigenvalues of the Jacobian matrix along its diagonal. By modifying the diagonal matrix, the Roe conditions could be satisfied.

In a previous work (Flåtten and Munkejord, 2006), an alternative approach for constructing an analytical Roe solver for the drift-flux model was presented. Herein, the problem was divided into a convective and a pressure part, allowing us to treat the Roe-averaging of the slip relation and the thermodynamic density relations as separate problems. However, the approach required the introduction of two separate Roe-averages of the velocities of each phase.

In the current paper, the approach has been improved such that there are unique Roe-averages for the phase velocities. Along with the improved method, numerical examples relevant for industrial challenges related to multiphase pipeline transport are presented. These illustrate the accuracy and robustness of the method.

THE DRIFT-FLUX MODEL

The drift-flux model consists of two equations for conservation of mass, one for each phase, and one equation for the conservation of total momentum as shown in equations (1) to (4).

$$\frac{\partial \boldsymbol{q}}{\partial t} + \frac{\partial \boldsymbol{f}(\boldsymbol{q})}{\partial x} = \boldsymbol{s}(\boldsymbol{q}) \tag{1}$$

$$\boldsymbol{q} = \begin{bmatrix} \rho_\mathrm{g}\alpha_\mathrm{g} \\ \rho_\ell\alpha_\ell \\ \rho_\mathrm{g}\alpha_\mathrm{g}v_\mathrm{g} + \rho_\ell\alpha_\ell v_\ell \end{bmatrix} = \begin{bmatrix} m_\mathrm{g} \\ m_\ell \\ I_\mathrm{g} + I_\ell \end{bmatrix} \tag{2}$$

$$\boldsymbol{f}(\boldsymbol{q}) = \begin{bmatrix} \rho_\mathrm{g}\alpha_\mathrm{g}v_\mathrm{g} \\ \rho_\ell\alpha_\ell v_\ell \\ \rho_\mathrm{g}\alpha_\mathrm{g}v_\mathrm{g}^2 + \rho_\ell\alpha_\ell v_\ell^2 + p \end{bmatrix} = \begin{bmatrix} I_\mathrm{g} \\ I_\ell \\ I_\mathrm{g}v_\mathrm{g} + I_\ell v_\ell + p \end{bmatrix} \tag{3}$$

$$\boldsymbol{s}(\boldsymbol{q}) = \begin{bmatrix} 0 \\ 0 \\ -F_\mathrm{w} \end{bmatrix} \tag{4}$$

The volume fractions satisfy:

$$\alpha_\ell + \alpha_\mathrm{g} = 1 \tag{5}$$

Thermodynamic submodel

The drift-flux model presented above is based on the assumption of isentropic and isothermal flow. Hence dynamic mass and energy transfer between the phases are neglected. A result of this assumption is that the pressure may be found as:

$$p = p(\rho_\ell) = p(\rho_\mathrm{g}) \tag{6}$$

Thus, the thermodynamic model relates the phase density to the common pressure according to equation (7).

$$\rho_\mathrm{k} = \rho_{\mathrm{k},0} + \frac{p - p_{\mathrm{k},0}}{c_\mathrm{k}^2} \tag{7}$$

The variables $p_{\mathrm{k},0}$ and c_k^2 are defined in equation (8) and (9) respectively.

$$p_{\mathrm{k},0} = p(\rho_{\mathrm{k},0}) \tag{8}$$

$$c_\mathrm{k}^2 \equiv \frac{\partial p}{\partial \rho_\mathrm{k}}(p_{\mathrm{k},0}) \tag{9}$$

For convenience, the model is implemented in the form of equation (10), where the variable ρ_k^0 is defined by equation (11)

$$p_\mathrm{k} = c_\mathrm{k}^2(\rho_\mathrm{k} - \rho_\mathrm{k}^0) \tag{10}$$

$$\rho_\mathrm{k}^0 = \rho_{\mathrm{k},0} - \frac{p_{\mathrm{k},0}}{c_\mathrm{k}^2} \tag{11}$$

Hydrodynamic submodel

In addition to the equations (1) to (4), an equation relating the liquid and gas velocities to each other is needed. The slip relation is defined as $\Phi = v_\mathrm{g} - v_\ell$, and in general it is presented on the form:

$$v_\mathrm{g} - v_\ell = \Phi(m_\mathrm{g}, m_\ell, v_\mathrm{g}) \tag{12}$$

In the present work, two different slip relations are implemented, the no slip relation, eq. (13), and the Zuber-Findlay slip relation, eq. (14).

$$\Phi = 0 \tag{13}$$

$$\Phi = \frac{(K-1)v_\mathrm{g} + S}{K\alpha_\ell} \tag{14}$$

The Zuber-Findlay slip relation is valid for slug and bubbly flow regimes, and K and S are flow dependent constants. The models are implemented because of their simplicity. However, as the slip relation for the various flow regimes may be far more complex, use of the analytic expression for the slip relation is avoided in the derived Roe averages used in this work.

THE ROE NUMERICAL SCHEME

If the flux functions are smooth in all independent variables such that the partial derivatives exists, the equation system in equation (1) may be written in a quasi-linear form as in equation (15).

$$\frac{\partial \boldsymbol{q}}{\partial t} + \boldsymbol{A}(\boldsymbol{q})\frac{\partial \boldsymbol{q}}{\partial x} = \boldsymbol{s}(\boldsymbol{q}) \tag{15}$$

The Roe scheme is based upon a replacement of the Jacobi matrix $\boldsymbol{A}$, with a matrix $\widehat{\boldsymbol{A}}$ containing averaged values for each grid interface. Hence the non-linear system is approximated by a locally linearised system:

$$\frac{\partial \hat{\boldsymbol{q}}}{\partial t} + \widehat{\boldsymbol{A}}_{\mathrm{i}-1/2}\frac{\partial \hat{\boldsymbol{q}}}{\partial x} = \boldsymbol{s}(\hat{\boldsymbol{q}}) \tag{16}$$

In Flåtten and Munkejord (2006), the Jacobian matrix, $\boldsymbol{A}$, was derived as:

$$\mathbf{A} = \frac{1}{\check{\rho}}\begin{bmatrix} m_{\mathrm{g}}m_\ell\mu_{\mathrm{g}} + \zeta m_\ell v_{\mathrm{g}} & m_{\mathrm{g}}m_\ell\mu_\ell - m_{\mathrm{g}}v_\ell & m_{\mathrm{g}} \\ -(m_{\mathrm{g}}m_\ell\mu_{\mathrm{g}} + \zeta m_\ell v_{\mathrm{g}}) & m_{\mathrm{g}}v_\ell - m_{\mathrm{g}}m_\ell\mu_\ell & \zeta m_\ell \\ a_{31} & a_{32} & a_{33} \end{bmatrix} \tag{17}$$

where

$$\begin{aligned} a_{31} =& \kappa\check{\rho}\rho_\ell + 2m_{\mathrm{g}}m_\ell\mu_{\mathrm{g}}(v_{\mathrm{g}} - v_\ell) + (\zeta m_\ell - m_{\mathrm{g}})v_{\mathrm{g}}^2 \\ & - 2\zeta m_\ell v_{\mathrm{g}} v_\ell \qquad (18) \\ a_{32} =& \kappa\check{\rho}\rho_{\mathrm{g}} + 2m_{\mathrm{g}}m_\ell\mu_\ell(v_{\mathrm{g}} - v_\ell) \\ & - (\zeta m_\ell - m_{\mathrm{g}})v_\ell^2 - 2m_{\mathrm{g}}v_{\mathrm{g}}v_\ell \qquad (19) \\ a_{33} =& 2(m_{\mathrm{g}}v_{\mathrm{g}} + \zeta m_\ell v_\ell) \qquad (20) \end{aligned}$$

The variables μ_{g}, μ_ℓ and μ_{v} are partial derivatives of the slip function with respect to gas volumetric mass, liquid volumetric mass and gas phase velocity respectively (see eq. (21) to eq. (23)). ζ is the partial derivative of the gas velocity with respect to liquid velocity (see eq. (24)).

$$\mu_{\mathrm{g}} = \left(\frac{\partial \Phi}{\partial m_{\mathrm{g}}}\right)_{m_\ell, v_{\mathrm{g}}} \tag{21}$$

$$\mu_\ell = \left(\frac{\partial \Phi}{\partial m_\ell}\right)_{m_{\mathrm{g}}, v_{\mathrm{g}}} \tag{22}$$

$$\mu_{\mathrm{v}} = \left(\frac{\partial \Phi}{\partial v_{\mathrm{g}}}\right)_{m_{\mathrm{g}}, m_\ell} \tag{23}$$

$$\zeta = \left(\frac{\partial v_\ell}{\partial v_{\mathrm{g}}}\right)_{m_{\mathrm{g}}, m_\ell} \tag{24}$$

The pseudo mass $\check{\rho}$ is defined as:

$$\check{\rho} = m_{\mathrm{g}} + \zeta m_\ell \tag{25}$$

κ is defined as:

$$\kappa = \frac{1}{(\partial_{\mathrm{p}}\rho_{\mathrm{g}})\rho_\ell\alpha_{\mathrm{g}} + (\partial_{\mathrm{p}}\rho_\ell)\rho_{\mathrm{g}}\alpha_\ell} \tag{26}$$

In accordance with the Jacobian matrix, the linearised matrix, $\widehat{\boldsymbol{A}}$, is defined as:

$$\widehat{\boldsymbol{A}} = \frac{1}{\hat{\check{\rho}}}\begin{bmatrix} \hat{a}_{11} & \hat{a}_{12} & \hat{m}_{\mathrm{g}} \\ -\hat{a}_{11} & -\hat{a}_{12} & \hat{\zeta}\hat{m}_\ell \\ \hat{a}_{31} & \hat{a}_{32} & \hat{a}_{33} \end{bmatrix} \tag{27}$$

where

$$\begin{aligned} \hat{a}_{11} =& \hat{m}_{\mathrm{g}}\hat{m}_\ell\hat{\mu}_{\mathrm{g}} + \hat{\zeta}\hat{m}_\ell\hat{v}_{\mathrm{g}} \qquad (28) \\ \hat{a}_{12} =& \hat{m}_{\mathrm{g}}\hat{m}_\ell\hat{\mu}_\ell - \hat{m}_{\mathrm{g}}\hat{v}_\ell \qquad (29) \\ \hat{a}_{31} =& \hat{\kappa}\hat{\check{\rho}}\hat{\rho}_\ell + 2\hat{m}_{\mathrm{g}}\hat{m}_\ell\hat{\mu}_{\mathrm{g}}(\hat{v}_{\mathrm{g}} - \hat{v}_\ell) + (\hat{\zeta}\hat{m}_\ell - \hat{m}_{\mathrm{g}})\hat{v}_{\mathrm{g}}{}^2 \\ & - 2\hat{\zeta}\hat{m}_\ell\hat{v}_{\mathrm{g}}\hat{v}_\ell \qquad (30) \\ \hat{a}_{32} =& \hat{\kappa}\hat{\check{\rho}}\hat{\rho}_{\mathrm{g}} + 2\hat{m}_{\mathrm{g}}\hat{m}_\ell\hat{\mu}_\ell(\hat{v}_{\mathrm{g}} - \hat{v}_\ell) - (\hat{\zeta}\hat{m}_\ell - \hat{m}_{\mathrm{g}})\hat{v}_\ell{}^2 \\ & - 2\hat{m}_{\mathrm{g}}\hat{v}_{\mathrm{g}}\hat{v}_\ell \qquad (31) \\ \hat{a}_{33} =& 2(\hat{m}_{\mathrm{g}}\hat{v}_{\mathrm{g}} + \hat{\zeta}\hat{m}_\ell\hat{v}_\ell) \qquad (32) \end{aligned}$$

The $\widehat{\boldsymbol{A}}_{\mathrm{i}-1/2}$ matrix has to fulfil three conditions :

Condition 1 $\widehat{\boldsymbol{A}}_{\mathrm{i}-1/2}$ *must be diagonalisable and have real eigenvalues*

Condition 2 $\widehat{\boldsymbol{A}}_{\mathrm{i}-1/2} \to \boldsymbol{f}'(\bar{\boldsymbol{q}})$ *as* $\boldsymbol{Q}_{\mathrm{i}-1}, \boldsymbol{Q}_{\mathrm{i}} \to \bar{\boldsymbol{q}}$

Condition 3 $\widehat{\boldsymbol{A}}_{\mathrm{i}-1/2}(\boldsymbol{Q}_{\mathrm{i}} - \boldsymbol{Q}_{\mathrm{i}-1}) = \boldsymbol{f}(\boldsymbol{Q}_{\mathrm{i}}) - \boldsymbol{f}(\boldsymbol{Q}_{\mathrm{i}-1})$

Condition 1 ensures that system (16) is hyperbolic. Condition 2 is required in order for the method to be consistent with the original conservation law. The last condition is proposed based on a desire of having $\mathscr{W}^p$ as an eigenvector of $\widehat{\boldsymbol{A}}_{\mathrm{i}-1/2}$ if the states $\boldsymbol{Q}_{\mathrm{i}-1}$ and $\boldsymbol{Q}_{\mathrm{i}}$ are connected by a single wave $\mathscr{W}^p = \boldsymbol{Q}_{\mathrm{i}} - \boldsymbol{Q}_{\mathrm{i}-1}$ in the true Riemann solution. For the particular expressions for fluctuations selected in this work (see eq. (71)), it will also guarantee that the numerical method is conservative. (LeVeque, 2007)

According to Theorem 2 in Flåtten and Munkejord (2006), the Roe matrix system can be divided into sub-systems in order to simplify the derivation of the averaged variables. The selected sub-systems are:

Equations for conservation of mass

$$\widehat{\boldsymbol{A}}_{\mathrm{m}} = \frac{1}{\hat{\check{\rho}}}\begin{bmatrix} \hat{m}_{\mathrm{g}}\hat{m}_\ell\hat{\mu}_{\mathrm{g}} + \hat{\zeta}\hat{m}_\ell\hat{v}_{\mathrm{g}} & \hat{m}_{\mathrm{g}}\hat{m}_\ell\hat{\mu}_\ell - \hat{m}_{\mathrm{g}}\hat{v}_\ell & \hat{m}_{\mathrm{g}} \\ -(\hat{m}_{\mathrm{g}}\hat{m}_\ell\hat{\mu}_{\mathrm{g}} + \hat{\zeta}\hat{m}_\ell\hat{v}_{\mathrm{g}}) & \hat{m}_{\mathrm{g}}\hat{v}_\ell - \hat{m}_{\mathrm{g}}\hat{m}_\ell\hat{\mu}_\ell & \hat{\zeta}\hat{m}_\ell \\ 0 & 0 & 0 \end{bmatrix} \tag{33}$$

$$\boldsymbol{f}_{\mathrm{m}}(\boldsymbol{q}) = \begin{bmatrix} m_{\mathrm{g}}v_{\mathrm{g}} \\ m_\ell v_\ell \\ 0 \end{bmatrix} \tag{34}$$

with the corresponding equation for Roe condition 3:

$$\widehat{\boldsymbol{A}}_{\mathrm{m}}(\boldsymbol{Q}^{\mathrm{R}} - \boldsymbol{Q}^{\mathrm{L}}) = \boldsymbol{f}_{\mathrm{m}}(\boldsymbol{Q}^{\mathrm{R}}) - \boldsymbol{f}_{\mathrm{m}}(\boldsymbol{Q}^{\mathrm{L}}) \tag{35}$$

In equation (35), the condition in cell i is labelled with R as it is on the right hand side of the cell interface. Similarly the condition in cell (i-1) is labelled with L. This notation will be used in the rest of this section.

Equations for conservation of momentum

Gas momentum convection

$$\widehat{\boldsymbol{A}}_{\mathrm{g}} = \frac{1}{\hat{\tilde{\rho}}} \begin{bmatrix} 0 & 0 & 0 \\ 0 & 0 & 0 \\ \hat{a}_{\mathrm{g},31} & \hat{a}_{\mathrm{g},32} & 2\hat{m}_{\mathrm{g}}\hat{v}_{\mathrm{g}} \end{bmatrix} \tag{36}$$

$$\boldsymbol{f}_{\mathrm{g}}(\boldsymbol{q}) = \begin{bmatrix} 0 \\ 0 \\ m_{\mathrm{g}} v_{\mathrm{g}}^2 \end{bmatrix} \tag{37}$$

where

$$\hat{a}_{\mathrm{g},31} = 2\hat{m}_{\mathrm{g}}\hat{m}_{\ell}\hat{v}_{\mathrm{g}}\hat{\mu}_{\mathrm{g}} + (\hat{\zeta}\hat{m}_{\ell} - \hat{m}_{\mathrm{g}})\hat{v}_{\mathrm{g}}{}^2 \tag{38}$$

$$\hat{a}_{\mathrm{g},32} = 2\hat{m}_{\mathrm{g}}\hat{m}_{\ell}\hat{v}_{\mathrm{g}}\hat{\mu}_{\ell} - 2\hat{m}_{\mathrm{g}}\hat{v}_{\mathrm{g}}\hat{v}_{\ell} \tag{39}$$

The Roe condition number 3 for the gas momentum conservation equations is expressed as:

$$\widehat{\boldsymbol{A}}_{\mathrm{g}}(\boldsymbol{Q}^{\mathrm{R}} - \boldsymbol{Q}^{\mathrm{L}}) = \boldsymbol{f}_{\mathrm{g}}(\boldsymbol{Q}^{\mathrm{R}}) - \boldsymbol{f}_{\mathrm{g}}(\boldsymbol{Q}^{\mathrm{L}}) \tag{40}$$

Liquid momentum convection

$$\widehat{\boldsymbol{A}}_{\mathrm{l}} = \frac{1}{\hat{\tilde{\rho}}} \begin{bmatrix} 0 & 0 & 0 \\ 0 & 0 & 0 \\ \hat{a}_{\mathrm{l},31} & \hat{a}_{\mathrm{l},32} & 2\hat{\zeta}\hat{m}_{\ell}\hat{v}_{\ell} \end{bmatrix} \tag{41}$$

$$\boldsymbol{f}_{\mathrm{l}}(\boldsymbol{q}) = \begin{bmatrix} 0 \\ 0 \\ m_{\ell} v_{\ell}^2 \end{bmatrix} \tag{42}$$

where

$$\hat{a}_{\mathrm{l},31} = -(2\hat{m}_{\mathrm{g}}\hat{m}_{\ell}\hat{v}_{\ell}\hat{\mu}_{\mathrm{g}} + 2\hat{\zeta}\hat{m}_{\ell}\hat{v}_{\mathrm{g}}\hat{v}_{\ell}) \tag{43}$$

$$\hat{a}_{\mathrm{l},32} = -(2\hat{m}_{\mathrm{g}}\hat{m}_{\ell}\hat{v}_{\ell}\hat{\mu}_{\ell} + (\hat{\zeta}\hat{m}_{\ell} - \hat{m}_{\mathrm{g}})\hat{v}_{\ell}{}^2) \tag{44}$$

The 3rd Roe condition expressed as:

$$\widehat{\boldsymbol{A}}_{\mathrm{l}}(\boldsymbol{Q}^{\mathrm{R}} - \boldsymbol{Q}^{\mathrm{L}}) = \boldsymbol{f}_{\mathrm{l}}(\boldsymbol{Q}^{\mathrm{R}}) - \boldsymbol{f}_{\mathrm{l}}(\boldsymbol{Q}^{\mathrm{L}}) \tag{45}$$

Pressure terms

$$\widehat{\boldsymbol{A}}_{\mathrm{p}} = \begin{bmatrix} 0 & 0 & 0 \\ 0 & 0 & 0 \\ \hat{\kappa}\hat{\rho}_{\ell} & \hat{\kappa}\hat{\rho}_{\mathrm{g}} & 0 \end{bmatrix} \tag{46}$$

$$\boldsymbol{f}_{\mathrm{p}}(\boldsymbol{q}) = \begin{bmatrix} 0 \\ 0 \\ p \end{bmatrix} \tag{47}$$

with Roe condition number 3 expressed as:

$$\widehat{\boldsymbol{A}}_{\mathrm{p}}(\boldsymbol{Q}^{\mathrm{R}} - \boldsymbol{Q}^{\mathrm{L}}) = \boldsymbol{f}_{\mathrm{p}}(\boldsymbol{Q}^{\mathrm{R}}) - \boldsymbol{f}_{\mathrm{p}}(\boldsymbol{Q}^{\mathrm{L}}) \tag{48}$$

Derivation of averaged parameters

Derivation of $\hat{\alpha}_{\ell}$, $\hat{\alpha}_{\mathrm{g}}$, $\hat{\rho}_{\ell}$ and $\hat{\rho}_{\mathrm{g}}$

The averaged volume fractions, $\hat{\alpha}_{\ell}$, $\hat{\alpha}_{\mathrm{g}}$, and densities, $\hat{\rho}_{\ell}$ and $\hat{\rho}_{\mathrm{g}}$, are found from the Roe condition 3 applied on the pressure sub-system, eq. (48). As in Flåtten and Munkejord (2006), $\hat{\kappa}$ is set equal to

$$\hat{\kappa} = \frac{1}{(\widehat{\partial_{\mathrm{p}}\rho_{\mathrm{g}}})\hat{\rho}_{\ell}\hat{\alpha}_{\mathrm{g}} + (\widehat{\partial_{\mathrm{p}}\rho_{\ell}})\hat{\rho}_{\mathrm{g}}\hat{\alpha}_{\ell}} \tag{49}$$

This leads to the equation

$$\frac{\hat{\rho}_{\ell}(m_{\mathrm{g}}^{\mathrm{R}} - m_{\mathrm{g}}^{\mathrm{L}}) + \hat{\rho}_{\mathrm{g}}(m_{\ell}^{\mathrm{R}} - m_{\ell}^{\mathrm{L}})}{(\widehat{\partial_{\mathrm{p}}\rho_{\mathrm{g}}})\hat{\rho}_{\ell}\hat{\alpha}_{\mathrm{g}} + (\widehat{\partial_{\mathrm{p}}\rho_{\ell}})\hat{\rho}_{\mathrm{g}}\hat{\alpha}_{\ell}} = p^{\mathrm{R}} - p^{\mathrm{L}} \tag{50}$$

For $\widehat{\partial_{\mathrm{p}}\rho_{\mathrm{k}}}$ the expression suggested by Flåtten and Munkejord (2006) is used:

$$\widehat{\partial_{\mathrm{p}}\rho_{\mathrm{k}}} = \begin{cases} \frac{\rho_{\mathrm{k}}^{\mathrm{R}} - \rho_{\mathrm{k}}^{\mathrm{L}}}{p^{\mathrm{R}} - p^{\mathrm{L}}} & p^{\mathrm{R}} \neq p^{\mathrm{L}} \\ (\partial_{\mathrm{p}}\rho_{\mathrm{k}})^{\mathrm{L}} & p^{\mathrm{R}} = p^{\mathrm{L}} \end{cases} \tag{51}$$

Entering the expression for $\widehat{\partial_{\mathrm{p}}\rho_{\mathrm{k}}}$ into equation (50), the requirement for the averaged variables can be expressed as:

$$\begin{aligned} &\hat{\rho}_{\ell}(m_{\mathrm{g}}^{\mathrm{R}} - m_{\mathrm{g}}^{\mathrm{L}}) + \hat{\rho}_{\mathrm{g}}(m_{\ell}^{\mathrm{R}} - m_{\ell}^{\mathrm{L}}) \\ &= \hat{\rho}_{\mathrm{g}}\hat{\alpha}_{\ell}(\rho_{\ell}^{\mathrm{R}} - \rho_{\ell}^{\mathrm{L}}) + \hat{\rho}_{\ell}\hat{\alpha}_{\mathrm{g}}(\rho_{\mathrm{g}}^{\mathrm{R}} - \rho_{\mathrm{g}}^{\mathrm{L}}) \end{aligned} \tag{52}$$

This equation is satisfied by arithmetic averages for volume fractions and densities:

$$\hat{\alpha}_{\ell} = \frac{1}{2}(\alpha_{\ell}^{\mathrm{L}} + \alpha_{\ell}^{\mathrm{R}}) \tag{53}$$

$$\hat{\alpha}_{\mathrm{g}} = \frac{1}{2}(\alpha_{\mathrm{g}}^{\mathrm{L}} + \alpha_{\mathrm{g}}^{\mathrm{R}}) \tag{54}$$

$$\hat{\rho}_{\ell} = \frac{1}{2}(\rho_{\ell}^{\mathrm{L}} + \rho_{\ell}^{\mathrm{R}}) \tag{55}$$

$$\hat{\rho}_{\mathrm{g}} = \frac{1}{2}(\rho_{\mathrm{g}}^{\mathrm{L}} + \rho_{\mathrm{g}}^{\mathrm{R}}) \tag{56}$$

Here, it was used that:

$$m_{\mathrm{k}} = \rho_{\mathrm{k}}\alpha_{\mathrm{k}} \tag{57}$$

Derivation of $\hat{\mu}_{\mathrm{g}}$, $\hat{\mu}_{\ell}$ and $\hat{\mu}_{\mathrm{v}}$

In Flåtten and Munkejord (2006), the derivation of averaged volumetric masses and velocities from the set of equations in (35) resulted in the criteria:

$$\hat{\mu}_{\mathrm{g}}(m_{\mathrm{g}}^{\mathrm{R}} - m_{\mathrm{g}}^{\mathrm{L}}) + \hat{\mu}_{\ell}(m_{\ell}^{\mathrm{R}} - m_{\ell}^{\mathrm{L}}) + \hat{\mu}_{\mathrm{v}}(v_{\mathrm{g}}^{\mathrm{R}} - v_{\mathrm{g}}^{\mathrm{L}}) = \Phi^{\mathrm{R}} - \Phi^{\mathrm{L}} \tag{58}$$

In the Roe scheme presented here we will use this as a starting point. Hence the averages derived in Flåtten and Munkejord (2006) may be kept:

$$\hat{\mu}_{\mathrm{g}} = \begin{cases} \frac{\Phi(m_{\mathrm{g}}^{\mathrm{R}}, m_{\ell}^{\mathrm{L}}, v_{\mathrm{g}}^{\mathrm{L}}) - \Phi(m_{\mathrm{g}}^{\mathrm{L}}, m_{\ell}^{\mathrm{L}}, v_{\mathrm{g}}^{\mathrm{L}})}{m_{\mathrm{g}}^{\mathrm{R}} - m_{\mathrm{g}}^{\mathrm{L}}} & \text{for} \quad m_{\mathrm{g}}^{\mathrm{L}} \neq m_{\mathrm{g}}^{\mathrm{R}} \\ \mu_{\mathrm{g}}(m_{\mathrm{g}}^{\mathrm{L}}, m_{\ell}^{\mathrm{L}}, v_{\mathrm{g}}^{\mathrm{L}}) & \text{for} \quad m_{\mathrm{g}}^{\mathrm{L}} = m_{\mathrm{g}}^{\mathrm{R}} \end{cases} \tag{59}$$

$$\hat{\mu}_{\ell} = \begin{cases} \frac{\Phi(m_{\mathrm{g}}^{\mathrm{R}}, m_{\ell}^{\mathrm{R}}, v_{\mathrm{g}}^{\mathrm{L}}) - \Phi(m_{\mathrm{g}}^{\mathrm{R}}, m_{\ell}^{\mathrm{L}}, v_{\mathrm{g}}^{\mathrm{L}})}{m_{\ell}^{\mathrm{R}} - m_{\ell}^{\mathrm{L}}} & \text{for} \quad m_{\ell}^{\mathrm{L}} \neq m_{\ell}^{\mathrm{R}} \\ \mu_{\ell}(m_{\mathrm{g}}^{\mathrm{R}}, m_{\ell}^{\mathrm{L}}, v_{\mathrm{g}}^{\mathrm{L}}) & \text{for} \quad m_{\ell}^{\mathrm{L}} = m_{\ell}^{\mathrm{R}} \end{cases} \tag{60}$$

$$\hat{\mu}_{\mathrm{v}} = \begin{cases} \frac{\Phi(m_{\mathrm{g}}^{\mathrm{R}}, m_{\ell}^{\mathrm{R}}, v_{\mathrm{g}}^{\mathrm{R}}) - \Phi(m_{\mathrm{g}}^{\mathrm{R}}, m_{\ell}^{\mathrm{R}}, v_{\mathrm{g}}^{\mathrm{L}})}{v_{\mathrm{g}}^{\mathrm{R}} - v_{\mathrm{g}}^{\mathrm{L}}} & \text{for} \quad v_{\mathrm{g}}^{\mathrm{L}} \neq v_{\mathrm{g}}^{\mathrm{R}} \\ \mu_{\mathrm{v}}(m_{\mathrm{g}}^{\mathrm{R}}, m_{\ell}^{\mathrm{R}}, v_{\mathrm{g}}^{\mathrm{L}}) & \text{for} \quad v_{\mathrm{g}}^{\mathrm{L}} = v_{\mathrm{g}}^{\mathrm{R}} \end{cases} \tag{61}$$

Derivation of $\hat{m}_{\mathrm{g}}$,$\hat{m}_{\ell}$, $\hat{v}_{\mathrm{g}}$ and $\hat{v}_{\ell}$

Inserting (58) into the first row of the equation system (35) gives the following condition:

$$\begin{aligned} \hat{m}_{\mathrm{g}}\hat{m}_{\ell}\left(\hat{\zeta}(v_{\mathrm{g}}^{\mathrm{R}} - v_{\mathrm{g}}^{\mathrm{L}}) - (v_{\ell}^{\mathrm{R}} - v_{\ell}^{\mathrm{L}})\right) + \hat{\zeta}\hat{m}_{\ell}\hat{v}_{\mathrm{g}}\left(m_{\mathrm{g}}^{\mathrm{R}} - m_{\mathrm{g}}^{\mathrm{L}}\right) \\ - \hat{m}_{\mathrm{g}}\hat{v}_{\ell}\left(m_{\ell}^{\mathrm{R}} - m_{\ell}^{\mathrm{L}}\right) + \hat{m}_{\mathrm{g}}\left(m_{\ell}^{\mathrm{R}}v_{\ell}^{\mathrm{R}} - m_{\ell}^{\mathrm{L}}v_{\ell}^{\mathrm{L}}\right) \\ = \hat{\zeta}\hat{m}_{\ell}\left(m_{\mathrm{g}}^{\mathrm{R}}v_{\mathrm{g}}^{\mathrm{R}} - m_{\mathrm{g}}^{\mathrm{L}}v_{\mathrm{g}}^{\mathrm{L}}\right) \end{aligned} \tag{62}$$

A second equation is found by adding the equations for Roe condition 3 for the gas and liquid momentum, eq. (40) and eq. (45), and using equation (58):

$$\begin{aligned}
&2\hat{m}_g\hat{m}_\ell(\hat{v_g}-\hat{v}_\ell)\left(\hat{\xi}(v_g^R-v_g^L)-(v_\ell^R-v_\ell^L)\right)\\
&\quad+\left((\hat{\xi}\hat{m}_\ell-\hat{m}_g)\hat{v_g}^2-2\hat{\xi}\hat{m}_\ell\hat{v}_g\hat{v}_\ell\right)\left(m_g^R-m_g^L\right)\\
&\quad-\left((\hat{\xi}\hat{m}_\ell-\hat{m}_g)\hat{v}_\ell^2+2\hat{m}_g\hat{v}_g\hat{v}_\ell\right)\left(m_\ell^R-m_\ell^L\right)\\
&\quad+2\left(\hat{m}_g\hat{v}_g+\hat{\xi}\hat{m}_\ell\hat{v}_\ell\right)\left(m_g^Rv_g^R+m_\ell^Rv_\ell^R-m_g^Lv_g^L-m_\ell^Lv_\ell^L\right)\\
&=\left(\hat{m}_g+\hat{\xi}\hat{m}_\ell\right)\left(m_g^R(v_g^R)^2+m_\ell^R(v_\ell^R)^2-m_g^L(v_g^L)^2-m_\ell^L(v_\ell^L)^2\right)
\end{aligned} \tag{63}$$

By inserting (62) into (63), the equation may be simplified to:

$$\begin{aligned}
&\hat{v_g}^2\left(m_g^R-m_g^L\right)-2\hat{v_g}\left(m_g^Rv_g^R-m_g^Lv_g^L\right)+m_g^R(v_g^R)^2-m_g^L(v_g^L)^2\\
&+\hat{v}_\ell^2\left(m_\ell^R-m_\ell^L\right)-2\hat{v}_\ell\left(m_\ell^Rv_\ell^R-m_\ell^Lv_\ell^L\right)+m_\ell^R(v_\ell^R)^2-m_\ell^L(v_\ell^L)^2=0
\end{aligned} \tag{64}$$

The equation may be satisfied by the averages:

$$\hat{v_g}=\frac{\sqrt{m_g^L}v_g^L+\sqrt{m_g^R}v_g^R}{\sqrt{m_g^L}+\sqrt{m_g^R}} \tag{65}$$

and

$$\hat{v}_\ell=\frac{\sqrt{m_\ell^L}v_\ell^L+\sqrt{m_\ell^R}v_\ell^R}{\sqrt{m_\ell^L}+\sqrt{m_\ell^R}}. \tag{66}$$

By reformulating equation (62) to:

$$\begin{aligned}
&\hat{\xi}\hat{m}_\ell\left(\hat{m}_g(v_g^R-v_g^L)+\hat{v_g}\left(m_g^R-m_g^L\right)-\left(m_g^Rv_g^R-m_g^Lv_g^L\right)\right)\\
&-\hat{m}_g\left(\hat{m}_\ell(v_\ell^R-v_\ell^L)+\hat{v}_\ell\left(m_\ell^R-m_\ell^L\right)-\left(m_\ell^Rv_\ell^R-m_\ell^Lv_\ell^L\right)\right)=0
\end{aligned} \tag{67}$$

it is seen that the conservation of mass is satisfied by the averages:

$$\hat{m}_g=\sqrt{m_g^Lm_g^R}, \tag{68}$$

$$\hat{m}_\ell=\sqrt{m_\ell^Lm_\ell^R} \tag{69}$$

when $\hat{v_g}$ and $\hat{v}_\ell$ are given by eq. (65) and (66).

NUMERICAL ALGORITHM

The numerical algorithm is similar to the one selected in Flåtten and Munkejord (2006). It is based on Godunov's method, applied on non-linear systems and with the use of limiters in order to increase the accuracy of smooth solutions (LeVeque, 2007):

$$\begin{aligned}
\boldsymbol{Q}_i^{n+1}=\boldsymbol{Q}_i^n&-\frac{\Delta t}{\Delta x}(\mathscr{A}^-\boldsymbol{\Delta Q}_{i+1/2}+\mathscr{A}^+\boldsymbol{\Delta Q}_{i-1/2})\\
&-\frac{\Delta t}{\Delta x}(\widetilde{\boldsymbol{F}}_{i+1/2}-\widetilde{\boldsymbol{F}}_{i-1/2})+\Delta t\,\boldsymbol{s}(\boldsymbol{Q}_i^n)
\end{aligned} \tag{70}$$

The source term has here been added on the right hand side of the equation for simplicity reasons. This will make the overall algorithm first order accurate. Using e.g. a Strang splitting algorithm to handle this term would increase the overall order of accuracy to two.
The fluctuations $\mathscr{A}^\pm\boldsymbol{\Delta Q}_{i-1/2}$ are found as:

$$\mathscr{A}^\pm\boldsymbol{\Delta Q}_{i-1/2}=\sum_{p=1}^{m}(s_{i-1/2}^p)^\pm\mathscr{W}_{i-1/2}^p \tag{71}$$

where

$$(s_{i-1/2}^p)^+=\max(0,s_{i-1/2}^p) \tag{72}$$

$$(s_{i-1/2}^p)^-=\min(0,s_{i-1/2}^p) \tag{73}$$

$$s_{i-1/2}^p=\hat{\lambda}_{i-1/2}^p \tag{74}$$

As mentioned earlier, the selected fluctuations will give a conservative method due to condition 3. (LeVeque, 2007)
The waves, $\mathscr{W}_{i-1/2}^p$, may be calculated from the eigenvectors of the Roe matrix $\widehat{\boldsymbol{A}}_{i-1/2}$:

$$\boldsymbol{Q}_i-\boldsymbol{Q}_{i-1}=\sum_{p=1}^{m}\mathscr{W}_{i-1/2}^p=\sum_{p=1}^{m}\beta_{i-1/2}^p\hat{\boldsymbol{r}}_{i-1/2}^p \tag{75}$$

$$\boldsymbol{\beta}_{i-1/2}=\widehat{\boldsymbol{R}}_{i-1/2}^{-1}(\boldsymbol{Q}_i-\boldsymbol{Q}_{i-1}) \tag{76}$$

The correction flux is defined in equation (77) with the limited wave $\widetilde{\mathscr{W}}_{i-1/2}^p$ defined as in equation (78).

$$\widetilde{\boldsymbol{F}}_{i-1/2}=\frac{1}{2}\sum_{p=1}^{m}|s_{i-1/2}^p|\left(1-\frac{\Delta t}{\Delta x}|s_{i-1/2}^p|\right)\widetilde{\mathscr{W}}_{i-1/2}^p \tag{77}$$

$$\widetilde{\mathscr{W}}_{i-1/2}^p=\phi(\theta_{i-1/2}^p)\mathscr{W}_{i-1/2}^p \tag{78}$$

$$\theta_{i-1/2}^p=\frac{\mathscr{W}_{I-1/2}^p\cdot\mathscr{W}_{i-1/2}^p}{\mathscr{W}_{i-1/2}^p\cdot\mathscr{W}_{i-1/2}^p} \tag{79}$$

where

$$I=\begin{cases}i-1 & s_{i-1/2}^p\geq 0\\ i+1 & s_{i-1/2}^p<0\end{cases} \tag{80}$$

The monotonized central-difference limiter (MC limiter), eq. (81), was chosen.

$$\phi(\theta)=\max(0,\min((1+\theta)/2,2,2\theta)) \tag{81}$$

NUMERICAL RESULTS

The numerical results from three different cases are presented. All cases are simulated with a CFL number of 0.5. (CFL $=\max_j|\lambda_j|\frac{\Delta t}{\Delta x}$. λ_j is the j-th eigenvalue of the Jacobian matrix, $\boldsymbol{A}$, Δt is the length of the time step and Δx is the size of the grid cells.) The phase velocities are related by the no-slip relation in the two first cases. In the third case, the Zuber-Findlay slip relation is used. This is also the only case where wall friction is included. In the two first cases the friction is neglected, e.g. $F_w=0$.

Table 1: Initial data for the Riemann problem

Quantity	Symbol (unit)	L	R
Volumetric mass:			
Phase 1	m_1	3.17123	2.70708
Phase 2	m_2	3.38324	4.0434
Total volumetric momentum	I_1+I_2	3.71816	3.5629

Table 2: Equation of state parameters for the Riemann problem

	Phase 1	Phase 2
ρ_o^k	0.0	0.0
Sonic speeds, c_k		
Case 1: $c_1 = c_2$	$\sqrt{6}$	$\sqrt{6}$
Case 2: $c_1 < c_2$	1	4
Case 2: $c_1 > c_2$	4	1

Case: A Riemann problem

The case is found in Banda *et al.* (2010) and has initial data with a single discontinuity. A no-slip relation is assumed for the gas and liquid velocities and the simulation is performed in a tube that is 2m long. Initial data and parameters related to the equation of state are shown in table 1 and table 2 respectively. The case results are shown for three different assumptions on the sonic speeds of the two phases. In the first simulation, the sonic speeds are set equal. In the following two simulations they differ.

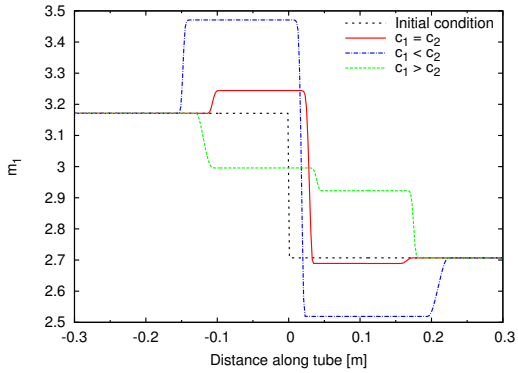

Figure 1: Riemann problem - Phase 1 volumetric mass

The results at $t = 0.06$s are presented in figure 1 to figure 4. The discontinuity is initially positioned at $x = 0$m and for clarity, the figure only shows the section of the tube containing waves. The simulation is run with 1000 grid cells.
Compared to the results in Banda *et al.* (2010), the waves have similar shapes and the results seem reasonable. However, the position of the wave-fronts and the amplitudes of the momentum waves differ. The largest differences are seen for the two cases $a_1^2 > a_2^2$ and $a_1^2 < a_2^2$. For these cases, the pressure levels presented in the article are wrong compared to the published initial data. It seems therefore that the authors of the article have presented results for the two cases that do not correspond with the data they provide. This is most likely the reason for the discrepancies that are observed.

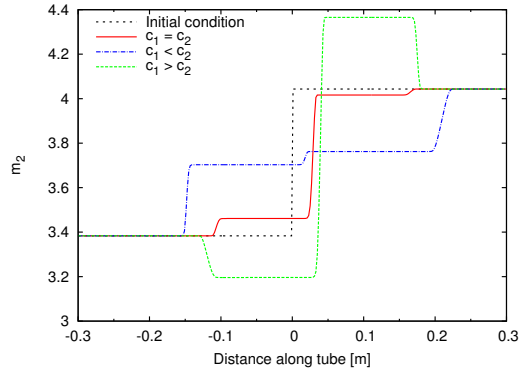

Figure 2: Riemann problem - Phase 2 volumetric mass

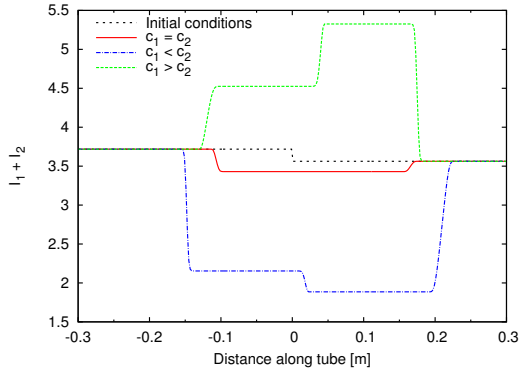

Figure 3: Riemann problem - Total volumetric momentum

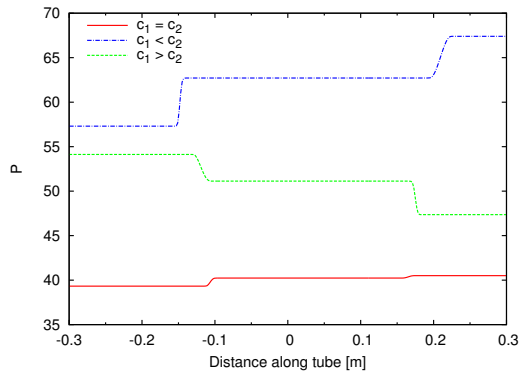

Figure 4: Riemann problem - Pressure

Table 3: Initial data for the moving Gauss curve

Quantity	Symbol (unit)	
Gas volume fraction	α_g(-)	$\alpha_{g,0}$
Pressure	p (kPa)	100
Gas velocity	v_g (m/s)	100
Liquid velocity	v_ℓ (m/s)	100

Table 4: Equation of state parameters for the moving Gauss curve case

	c_k (m/s)	ρ_o^k (kg/m^3)
Gas (g)	$\sqrt{10^5}$	0
Liquid (l)	1000	1000

Case: Moving Gauss curve - Investigation of model accuracy

The convergence order of smooth solutions has been verified using a constructed test case found in Munkejord *et al.* (2009). The initial volume fraction profile in a 12 meter long tube is according to equation (82), and it is moving along the tube with the speed of the liquid and vapour.

$$\alpha_{g,0} = (1-2\varepsilon)\exp\left(-\frac{(x-\mu)^2}{2\sigma^2}\right)+\varepsilon \qquad (82)$$

where $\varepsilon = 1\times10^{-12}$, $\mu = 6$m and $\sigma = 0.42$m.
The simulation is run for 0.03 seconds with periodic boundary conditions. As seen in table 3, the fluid velocity in the pipe is 100 m/s. Hence at the end of the simulation time, the analytical solution is a volume fraction profile which is symmetric around $x = 9$m. This is shown as the analytical result in figure 5 and figure 6. The parameters presented in table 4 were used in the equation of state for the simulation.
The results presented in figure 5 and figure 6 illustrate the differences in the results introduced by the MC limiter. The main difference is the accuracy obtained when using the MC limiter, even for a fairly low number of grid cells. This is the main reason for the focus on the very small region in figure 6. The figures also show that while the original simulation is symmetric around $x = 9$m, the results from the simulation with limiter are nonsymmetrical. This is due to the nature of the limiter method (Munkejord *et al.*, 2009).
The convergence order is calculated by finding the error in the calculated gas volume fraction as (Munkejord *et al.*, 2009):

$$||\mathscr{E}(\alpha_g,\Delta x)||_1 = \Delta x\sum_{\forall j}|\alpha_{g,j}-\alpha_{g,\mathrm{ref},j}| \qquad (83)$$

The error for two simulations with grid size Δx_1 and Δx_2 are then compared in order to determine the convergence order (Munkejord, 2005):

$$n = \frac{\ln[||\mathscr{E}(\alpha_g,\Delta x_2)||_1/||\mathscr{E}(\alpha_g,\Delta x_1)||_1]}{\ln[\Delta x_2/\Delta x_1]} \qquad (84)$$

Table 5 shows the estimated errors and convergence order for selected grid sizes. As expected, the numerical scheme with limiter approaches an order of 2, while the scheme without limiter approaches an order of 1.

Table 5: Convergence order calculated from simulation results

	Without limiter		With MC limiter	
Δx	$\|\|\mathscr{E}(\alpha_g)\|\|_1$	n	$\|\|\mathscr{E}(\alpha_g)\|\|_1$	n
0.015	1.109×10^{-1}		1.571×10^{-3}	
0.0075	5.852×10^{-2}	0.92	4.077×10^{-4}	1.95
0.00375	3.011×10^{-2}	0.96	1.028×10^{-4}	1.99
0.001875	1.528×10^{-2}	0.98	2.598×10^{-5}	1.98
0.0009375	7.695×10^{-3}	0.99	6.525×10^{-6}	1.99

In order to compare the performance of the Roe scheme, simulation results were also obtained using the FORCE scheme (see e.g. Toro (2009, Ch. 18.2) or Chen and Toro (2004)). Among the three-point centered difference schemes, FORCE is regarded as the optimal scheme (Chen and Toro, 2004). Simulations were run at different grid cell sizes in order to achieve an error estimate equivalent to the one obtained by

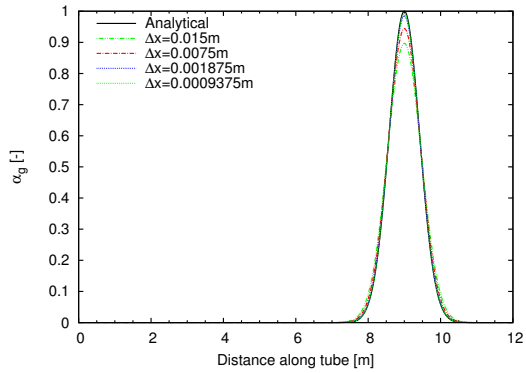

Figure 5: Gas volume fraction profile at $t = 0.03s$ - Roe scheme without limiter

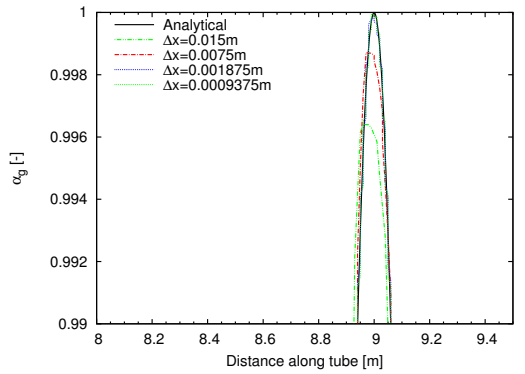

Figure 6: Gas volume fraction profile at $t = 0.03s$ - Roe scheme with MC limiter

Table 6: Comparison of CPU consumption for FORCE vs Roe numerical schemes

	$\Delta x[m]$	$\|\|\mathscr{E}(\alpha_g)\|\|_1$	CPU consumption $[s]$	Relative Error $[-]$	Relative consumption $[-]$
Roe scheme without limiter	0.015	1.109×10^{-1}	1.347×10^{2}	1	1
Roe scheme with MC limiter	0.015	1.571×10^{-3}	1.545×10^{2}	0.0142	1.147
	0.001875	1.526×10^{-1}	6.754×10	1.376	50.14
FORCE	0.001290	1.099×10^{-1}	1.415×10^{4}	0.990	105.0
	0.0009375	8.213×10^{-2}	2.677×10	0.740	198.7

Table 7: Equation of state parameters for the pipe flow problem

	c_k (m/s)	ρ_o^k (kg/m^3)
Gas (g)	$\sqrt{10^5}$	0
Liquid (l)	1000	999.9

the largest grid cell size when using the Roe scheme without limiter. For each simulation the CPU time consumption as reported from the program was registered. The results are shown in table 6. They show that for this case, the Roe scheme both with and without limiter is far more efficient regarding CPU time consumption than the FORCE scheme.

Case: Pipe flow

In the pipe flow case, a pipe which is 1000m long is initially filled with stagnant liquid at a pressure of 1bar. A small gas fraction of $\alpha_g = 1 \times 10^{-5}$ flows with a velocity corresponding to the slip relation (14). The relation is used with K as a constant of value 1.0. S is expressed as a function of the volume fraction:

$$S = S(\alpha_g) = \frac{1}{2}\sqrt{1-\alpha_g} \tag{85}$$

At the outlet boundary, the pressure is kept constant at 1bar. At the pipe inlet, the flow rate of gas and liquid are varied:

- *Inlet liquid flow rate:* increased linearly from zero to 12.0kg/s from $t = 0$s to $t = 10$s, kept constant from $t = 10$s to $t = 175$s.
- *Inlet gas flow rate:* increased linearly to 0.08kg/s from $t = 0$s to $t = 10$s, kept constant to $t = 50$s, decreased linearly to 1×10^{-8}kg/s from $t = 50$s to $t = 70$s and kept constant for the rest of the simulation until $t = 175$s.

The equation of state parameters used in the case are found in table 7. In this case, wall friction is also included. This is modelled as

$$F_w = \frac{32 v_m \eta_m}{d^2} \tag{86}$$

where v_m is the mixture velocity defined as

$$v_m = \alpha_g v_g + \alpha_\ell v_\ell \tag{87}$$

η_m is the dynamic mixture viscosity defined as

$$\eta_m = \alpha_g \eta_g + \alpha_\ell \eta_l \tag{88}$$

d is the tube diameter, set to 0.1m. The constants η_g and η_l are set to $\eta_g = 5 \times 10^{-6}$Pa s, $\eta_l = 5 \times 10^{-2}$Pa s. Results for the time $t = 175$s is presented in figure 7 to figure 10. The results correspond well with the ones presented in Flåtten and Munkejord (2006).

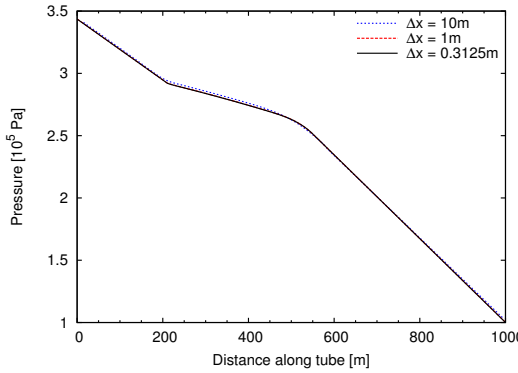

Figure 7: Pipe flow case - Pressure

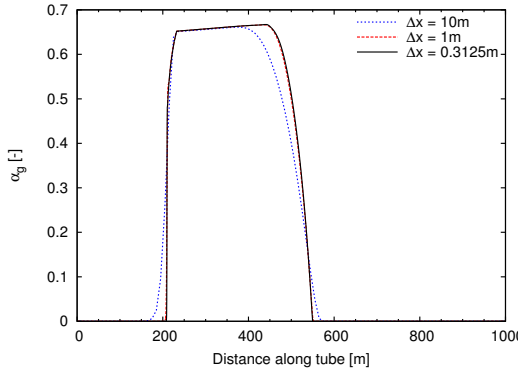

Figure 8: Pipe flow case - Gas volume fraction

CONCLUSION

A simplified analytical Roe scheme for a drift-flux, two-phase flow model is derived. The work in based on a pre-

vious work, Flåtten and Munkejord (2006), where the simplification is to introduce only one set of averaged velocities for each phase. The robustness of the scheme, and the possibility of extending to second order accuracy for smooth solutions by introducing wave-limiters are illustrated by the three different numerical examples presented.

ACKNOWLEDGEMENT

This publication is based on results from the research project Enabling low emission LNG systems, performed under the Petromaks program. The authors acknowledge the project partners; Statoil and GDF SUEZ, and the Research Council of Norway (193062/S60) for support.

REFERENCES

BANDA, M.K. *et al.* (2010). "Coupling drift-flux models with unequal sonic speeds". *Mathematical and Computational Applications*, **15(4)**, 574–584.

CHEN, G.Q. and TORO, E.F. (2004). "Centered difference schemes for nonlinear hyperbolic equations". *Journal of Hyperbolic Differential Equations*, **1(3)**, 531–566.

FLÅTTEN, T. and MUNKEJORD, S.T. (2006). "The approximate Riemann solver of Roe applied to a drift-flux two-phase flow model". *ESAIM Mathematical Modelling and Numerical Analysis*, **40**, 735–764.

LEVEQUE, R.J. (2007). *Finite volume methods for hyperbolic problems*. 6th ed. Cambridge University Press.

MUNKEJORD, S.T. (2005). *Analysis of the two-fluid model and the drift-flux model for numerical calculation of two-phase flow*. Ph.D. thesis, Norwegian University of Science and Technology.

MUNKEJORD, S.T. *et al.* (2009). "A musta scheme for a nonconservative two-fluid model". *SIAM Journal of Scientific computing*, **31(4)**, 2587–2622.

ROE, P.L. (1981). "Approximate riemann solvers, parameter vectors, and difference schemes". *Journal of Computational Physics*, **43(2)**, 357–372.

ROMATE, J.E. (1997). "An approximate riemann solver for a two-phase flow model with numerically given slip relation". *Computers & Fluids*, **27(4)**, 455 – 477.

TORO, E.F. (2009). *Riemann sovers and numerical methods for fluid dynamics*. 3rd ed. Springer.

TOUMI, I. and CARUGE, D. (1998). "An implicit second-order numerical method for three-dimensional two-phase flow calculations". *Nuclear Science and Engineering*, **130**, 213–225.

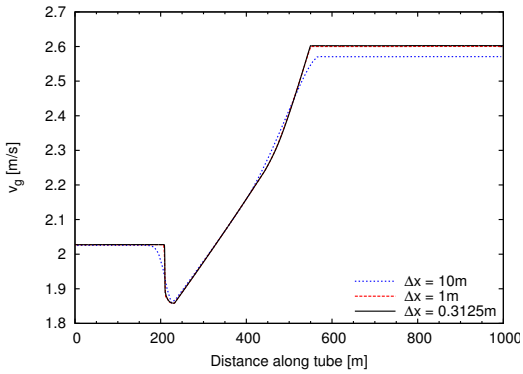

Figure 9: Pipe flow case - Gas velocity

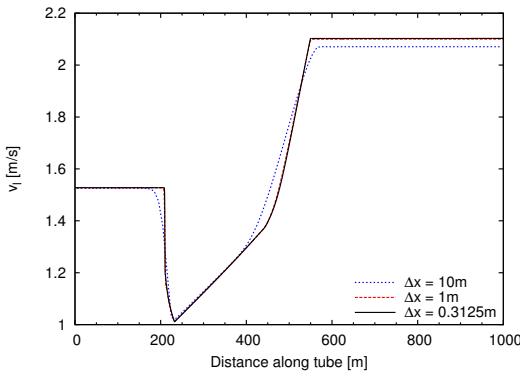

Figure 10: Pipe flow case - Liquid velocity

C

Paper II - Coupling Constants and the Generalized Riemann Problem for Isothermal Junction Flow

Authors: Gunhild A. Reigstad, Tore Flåtten, Nils Erland Haugen and Tor Ytrehus

Submitted to *Journal of Hyperbolic Differential Equations*, September 2013

Is not included due to copyright

D

Paper III - Numerical Network Models and Entropy Principles for Isothermal Junction Flow

Author: Gunhild A. Reigstad

Accepted by *Networks and Heterogeneous Media*, December 2013

Manuscript submitted to
AIMS' Journals
Volume **X**, Number **0X**, XX **200X**

doi:10.3934/xx.xx.xx.xx

pp. **X–XX**

NUMERICAL NETWORK MODELS AND ENTROPY PRINCIPLES FOR ISOTHERMAL JUNCTION FLOW

Gunhild A. Reigstad

Dept. of Energy and Process Engineering,
Norwegian University of Science and Technology (NTNU)
NO-7491 Trondheim, Norway

(Communicated by the associate editor name)

Abstract. We numerically explore network models which are derived for the isothermal Euler equations. Previously we proved the existence and uniqueness of solutions to the generalized Riemann problem at a junction under the conditions of monotone momentum related coupling constant and equal cross-sectional areas for all connected pipe sections. In the present paper we extend this proof to the case of pipe sections of different cross-sectional areas.

We describe a numerical implementation of the network models, where the flow in each pipe section is calculated using a classical high-resolution Roe scheme. We propose a numerical treatment of the boundary conditions at the pipe-junction interface, consistent with the coupling conditions. In particular, mass is exactly conserved across the junction.

Numerical results are provided for two different network configurations and for three different network models. Mechanical energy considerations are applied in order to evaluate the results in terms of physical soundness. Analytical predictions for junctions connecting three pipe sections are verified for both network configurations. Long term behaviour of physical and unphysical solutions are presented and compared, and the impact of having pipes with different cross-sectional area is shown.

1. **Introduction.** Models for networks of hyperbolic conservation laws are for example used to describe traffic flow [6,15] and fluid flow in junctions [1–3,7,10,13,16]. Gas transport in pipe networks is the most common fluid flow application, but systems of water distribution, tunnel aerodynamics, mine ventilation and gas dynamics in engines and engine manifolds have also been considered [16]. With the extension of the theory to two-phase flows, at present developed for the drift-flux model [3,4], one could as well potentially investigate flow distribution issues in e.g. heat exchangers. More advanced models would however be needed in order to account for phase change in the fluid and heat transfer to the flows.

1.1. **The network models.** A network model for fluid flow in pipes consists of a set of hyperbolic equations describing the flow in each pipe together with a set of coupling conditions. The hyperbolic conservation laws are given by

$$\frac{\partial \boldsymbol{U}_k}{\partial t} + \frac{\partial}{\partial x}\boldsymbol{F}\left(\boldsymbol{U}_k\right) = 0, \qquad k \in \{1, \dots, N\}, \tag{1}$$

2010 *Mathematics Subject Classification.* Primary: 35L65, 76N15.
Key words and phrases. gas flow, networks, junctions, isothermal Euler equations.

where in each pipe section k, we seek the solution $\boldsymbol{U}_k(x,t)$ for $t \in \mathbb{R}^+$ and $x \in \mathbb{R}^+$. It is assumed that the junction-pipe interface is positioned at $x = 0$.

The boundary conditions at each junction-pipe interface are determined by a set of coupling conditions. The conditions relate the flows in each of the N pipe sections and are closely linked to the applied conservation law (1). The coupling conditions we will be concerned with in this paper, derived for the isothermal Euler equations, are presented below in Definition 1.1. Following the approach of [8, 9], this definition of the solution to the generalized Riemann problem at the junction is set up allowing for pipe-sections of different cross-sectional areas. The coupling conditions are denoted RP1 and RP2.

Definition 1.1. A solution to the generalized Riemann problem at a junction,

$$\boldsymbol{U}_k(x,0) = \bar{\boldsymbol{U}}_k \qquad \forall k \in \{1,\dots,N\},\ x \in \mathbb{R}^+, \tag{2}$$

is a set of self-similar functions $\boldsymbol{U}_k(x,t)$ such that

RP0: For all $k \in \{1,\dots,N\}$, there exists a state

$$\boldsymbol{U}_k^*\left(\bar{\boldsymbol{U}}_1,\dots,\bar{\boldsymbol{U}}_N\right) = \lim_{x\to 0^+} \boldsymbol{U}_k(x,t) \tag{3}$$

such that $\boldsymbol{U}_k(x,t)$ is given by the restriction to $x \in \mathbb{R}^+$ of the Lax solution to the standard Riemann problem for $x \in \mathbb{R}$:

$$\begin{aligned} \frac{\partial \boldsymbol{U}_k}{\partial t} + \frac{\partial}{\partial x}\boldsymbol{F}(\boldsymbol{U}_k) &= 0, \\ \boldsymbol{U}_k(x,0) &= \begin{cases} \bar{\boldsymbol{U}}_k & \text{if } x > 0 \\ \boldsymbol{U}_k^* & \text{if } x < 0. \end{cases} \end{aligned} \tag{4}$$

RP1: Mass is conserved at the junction:

$$\sum_{k=1}^{N} A_k \rho_k^* v_k^* = 0. \tag{5}$$

RP2: There is a unique, scalar momentum related coupling constant at the junction:

$$\mathcal{H}(\rho_k^*, v_k^*) = \tilde{\mathcal{H}} \qquad \forall k \in \{1,\dots,N\}. \tag{6}$$

Equation (4) is a constructed half-Riemann problem where $\boldsymbol{U}_k^*$ is calculated using the coupling conditions (5) and (6). The two states $\bar{\boldsymbol{U}}_k$ and $\boldsymbol{U}_k^*$ are assumed to be connected by a wave with non-negative speed. For the isothermal Euler equations at subsonic conditions this implies that the states are connected by waves of the second family. A_k is the cross-sectional area of pipe k, ρ_k^* and v_k^* are density and velocity at the boundary, respectively.

To select *entropic* solutions we follow the approach of [7, 22]:

Definition 1.2. An **entropic** solution to the Riemann problem (2) is a solution satisfying the conditions RP0–RP2 as well as

RP3: Energy does not increase at the junction, i. e.

$$\sum_{k=1}^{N} A_k \rho_k^* v_k^* \left(\frac{1}{2}(v_k^*)^2 + a^2 \ln\frac{\rho_k^*}{\rho_0}\right) \leq 0, \tag{7}$$

where ρ_0 is some reference density and a is the constant fluid speed of sound, see (10).

Equation (7) is based on the mechanical energy flux function for the one-dimensional Euler equations for gas dynamics together with the isothermal pressure law [22].

We also refer to [1, 2, 7–9, 14, 22] for more details on the network theory.

1.2. **Approaches for solving a fluid network system.** The mathematical theory of compressible pipe flow in networks has mainly been developed during the last decade [1, 2, 7–9, 12]. Prior to that, and in parallel, this phenomenon has been studied from the more applied point of view.

Osiadacz [19] and Kiuchi [17] uses an equation of state for each junction. The equation is based on a finite junction volume and summation of ingoing and outgoing flows. The equations have been implemented into an implicit scheme used to simulate large pipe network systems.

Hong and Kim [16] also model the junction as a node of finite volume. However, each node is characterised by the three-dimensional Euler equations and the wall forces are accounted for. With the aid of the normal vector at each pipe-junction interface, the three-dimensional flux function is converted into one-dimensional pipe boundary conditions. Hence the model is able to account for the junction geometry. Special care is taken to ensure that the stagnation enthalpy is conserved at the boundaries, and the flow in each pipe is calculated using a modified scheme based on the approximate Riemann solver of Roe. In their paper, numerical results for several different T-junction configurations are presented. For Mach numbers less than 0.2 the results are seen to correspond well to analytic correlations that are based on the assumption of incompressible flow. It is also concluded that the model to some extent reflects the compressibility effect at higher Mach numbers.

A methodology used to estimate the total pressure loss coefficient for internal compressible flow in T-junctions was established by Perez-Garcia et al. [21]. The Reynolds Averaged Navier-Stokes equations were used to simulate the flow in a 90° T-junction, modelled in a three-dimensional computational domain. For Mach numbers larger than 0.2, pressure loss factors were found as a function of mass flow ratio and extrapolated Mach number in the common branch. The numerical results from the three-dimensional model were compared to experimental data, with a generally good agreement. However, challenges with both the experimental measurements and the numerical modelling were seen to produce deviations.

Pearson et. al. [20] compared schlieren images and pressure histories obtained from a two-dimensional numerical model against experimental results for a three-pipe junction. The three pipes constituted a 180° junction where two adjacent pipes merged into one pipe with cross-sectional area equal to the sum of the two first pipes. An approximate Roe solver was used to resolve the fluid dynamics modelled by the two-dimensional Euler equations, and adaptive grid refinement could be used. It was found that the pressure-loss characteristics of the junction could be reproduced by a model with a numerical mesh much coarser than what was needed in order to produce well resolved two-dimensional images of the wave front. Thus, the proposed numerical model was seen as a feasible sub-model for an internal combustion engine design tool. There it would be used together with one-dimensional models for gas dynamics.

Early mathematical models for gas flow in pipe networks were closely related to network models for traffic flow, building on the initial approach of Holden and Risebro [15]. Banda et al. [1, 2] describe models for the isothermal Euler equations. The pipes at the junction were divided into ingoing and outgoing pipes, and it was assumed that the velocity in each pipe always would be non-negative. It was as

well assumed that no vacuum states would appear. The problem was set up as a half-Riemann problem where the solution was found as a maximisation problem on the total mass flux at the junction. Supply and demand functions were defined and used as an important part of this problem formulation.

The additional restriction needed in order to complete the problem formulation was discussed in [2]. Two options were considered: equal pressure at the vertex and subsonic flow on all outgoing pipes. The choice of equal pressure was used in [1]. The models in [1, 2] were numerically implemented, and results from a set of test cases were presented.

A comparison between the network model proposed in [1] and results from a two-dimensional simulation model was performed by Herty and Seaïd [14]. A flow merge and a flow split configuration in a 90° T-junction were used as test cases. It was found that in both cases the trend between the results were similar. However, for the flow merge case, deviations were seen. Therefore the approach of using empirical geometry dependent pressure loss coefficients was said to be supported for this configuration.

Colombo and Garavello [7] modified the mathematical description of network models for gas flow in pipe networks and established a network model for the p-system. Flow directions in the pipe sections were no longer given a priori, and the maximisation problem was replaced by an entropy condition (Eq. (7)) in addition to the mass- and momentum related coupling conditions (Eq. (5) and (6)). The selection of momentum related coupling constant was investigated by looking at the well posedness of the Riemann problem at a junction connecting three pipes. The analysis showed that equal momentum flux gave a problem that continuously depended on the initial conditions. This was not the case when pressure was used as coupling constant.

For the network model with momentum flux as coupling constant, Colombo and Garavello [7] investigated the existence and uniqueness of solutions, and proved that it was global in time and local in the subsonic state space.

The Cauchy problem at a junction for the p-system was investigated by Colombo and Garavello [8]. Well posedness was proved for initial states that are perturbations of subsonic states that are stationary, entropic solutions to the generalized Riemann problem.

Numerical results for network models based on the p-system are presented in [9]. In particular, the pressure is modelled by the γ-law:

$$p(\rho) = p_0 \left(\frac{\rho}{\rho_0} \right)^{\gamma}, \tag{8}$$

with the parameters $\gamma = 1.4$, $p_0 = 1$ and $\rho_0 = 1$. Three different junctions were considered. They consisted of two, three and four pipes connected at the junction, respectively. In all cases the pipes connected at the junction are of different cross-sectional area. In the last case the two momentum related coupling constants considered, pressure and momentum flux, were seen to give qualitatively different results for the chosen initial data.

Brouwer et al. [5] used a friction dominated pipe model together with suitable coupling conditions in order to simulate a gas pipeline case from the Norwegian continental shelf. The pipeline network is characterised by supply and demand restrictions at a given set of locations, and the results are presented in terms of

stationary pressure distribution and throughput. The simulation results were compared to previous presented results on the same case. However, due to missing case information the comparison was rather limited.

The analysis performed in our previous work [22] was motivated by the usage of two different momentum related coupling constants; pressure and momentum flux. Network models with the two coupling constants were considered for the special case where all pipe sections have equal cross-sectional areas. Under this assumption, existence and uniqueness of entropic solutions was found to be global in time and local in the subsonic state space:

Proposition 1. *(Proposition 9 in [22]) Consider the generalized Riemann problem at a junction of N pipes with equal cross-sectional areas. With pressure or momentum flux as coupling constant (RP2), there exists a unique solution satisfying RP0–RP2 provided that the initial data belongs to the subsonic region as defined in [22]. There does not exist solutions that satisfy RP3 (entropic solutions) for all initial data in this subsonic region.*

Using the concept of ideal flow in a junction as starting point, the Bernoulli invariant was suggested as momentum related coupling constant. The invariant is derived from the conservation equation for total mechanical energy in smooth flows and is constant along streamlines. These properties are both valid for ideal flow, as such flow should be reversible and have uninterrupted streamlines.

The subsequent analysis of the network model containing Bernoulli invariant as coupling constant allowed us to prove existence and uniqueness globally both in time and in the subsonic state space:

Proposition 2. *(Proposition 10 in [22]) Consider the generalized Riemann problem at a junction of N pipes with equal cross-sectional areas. With Bernoulli invariant as coupling constant (RP2) there exists a unique entropic solution satisfying RP0-RP3 provided that the initial data belongs to the subsonic region as defined in [22].*

1.3. **Overview.** The aim of the present work is twofold: to present an appropriate numerical method for junction flow and to explore the impact of the different momentum related coupling constants numerically. As network theory is a fairly young field of research, there does not seem to be any established benchmarks which could serve as standard test cases. Therefore, we have here constructed two basic network configurations for our numerical investigations. For both of them we are able to numerically evaluate the entropy condition (7). This allows us to analyse if a solution is physical or not, even at conditions where we are not able to compare our results to analytical ones.

Before we describe the numerical method and the evaluation of results, two different issues are investigated analytically. First, the previous work performed in [22] was based on the assumption of pipe-sections of equal cross-sectional areas. In Section 2 we consider problems that are not restricted by this assumption. For monotone momentum related coupling constants, we provide a proof for the existence and uniqueness of solutions to the generalized Riemann problem in the sense of Definition 1.1.

Second, the standard Riemann problem is a well known test case with analytic solution. Formulated as a network problem, the case consists of two pipe sections of equal cross-sectional area connected at a junction. An analytical investigation of such a network configuration is presented in Section 3. The solutions of the network model and the standard Riemann problem are compared. Two conditions

on the momentum related coupling constants, which ensure that the two solutions coincide, are identified. Both pressure, momentum flux and Bernoulli invariant as coupling constant are seen to fulfil the conditions. Thus the corresponding models should all predict the analytical solution to the standard Riemann problem.

The implemented network models are presented in Section 4. The flow in each pipe section is calculated using an approximate Riemann solver of Roe, presented in Section 4.1 and Section 4.2. Section 4.3 shows how the conservative flux function at the pipe junction interface has been evaluated and set such that mass is conserved at the junction. Finally, the numerical procedure used to calculate $\boldsymbol{U}_k^*$ for each pipe section is presented in Section 4.4.

Numerical results for the first test case, a closed network consisting of three pipe sections connected at two junctions, is presented in Section 5.1. Using the total energy in the network as indicator, we show how both pressure and momentum flux as coupling constant lead to unphysical solutions for different initial conditions. We also show the long term development of the total energy as waves interact in pipe sections and at the junctions.

Steady state conditions in an open network model is presented in Section 5.2. The network consists of a symmetric branch structure where the flow in each pipe section is divided equally between two pipes at each junction. Simulations on a model where all pipes are of equal cross-sectional area verify the presence of unphysical solutions for pressure and momentum flux as coupling constant. Using the same initial conditions, but changing the cross-sectional areas such that the velocities in all pipe sections are equal, we observe no unphysical behaviour.

1.4. **The isothermal Euler equations.** In this work, we follow the approach of [1, 2, 7, 14, 17, 19] and consider one dimensional, compressible, pipe flow governed by the *isothermal* Euler equations. These consist of the isentropic Euler equations

$$\frac{\partial}{\partial t}\begin{bmatrix}\rho\\ \rho v\end{bmatrix} + \frac{\partial}{\partial x}\begin{bmatrix}\rho v\\ \rho v^2 + p(\rho)\end{bmatrix} = \begin{bmatrix}0\\ 0\end{bmatrix}, \tag{9}$$

together with a specific pressure law

$$p(\rho) = a^2\rho. \tag{10}$$

Here ρ and v are the fluid density and velocity, respectively, $p(\rho)$ is the pressure and a is the constant fluid speed of sound.

A more general formulation of (10) was considered in [7]. By an appropriate extension of the theory presented in [22], it should be possible to extend our numerical method to this more general formulation.

2. **Existence and uniqueness of solutions to the generalized Riemann problem at a junction.** A proof of uniqueness and existence of solutions to the generealized Riemann problem, as stated in Definition 1.1, was presented in [22] for the special case of equal cross-sectional areas in all pipe sections. This proof is valid for *monotone* momentum related coupling constants as defined below:

Definition 2.1. A momentum related coupling constant is **monotone** if

$$\frac{\mathrm{d}\mathcal{H}_k^*(M_k^*;\bar{\rho}_k,\bar{M}_k)}{\mathrm{d}M_k^*} > 0 \quad \text{for } M_k^* \in \langle -1, 1\rangle \tag{11}$$

for both shock waves and rarefaction waves connecting the two states $\boldsymbol{U}_k^*$ and $\bar{\boldsymbol{U}}_k$.

In Definition 2.1, $M_k^* = v_k^*/a$ is the Mach number and $\mathcal{H}_k^*$ is the coupling constant value for pipe section k. The constant is a function of ρ_k^* or M_k^* alone, because both variables may be expressed as a function of the other variable and of $\bar{\boldsymbol{U}}_k$, which is a constant state, using the appropriate wave equation [22].

Here we will extend the proof of existence and uniqueness to the case of pipe sections of different cross-sectional areas. That is, we will show that the conditions RP0 – RP2 have a unique solution that exists for all subsonic initial data when the momentum related coupling constant is monotone. The proof will extensively be based on the results found in [22].

First we state the extended definition of subsonic initial conditions:

Definition 2.2. Assume that a set $\{\bar{\boldsymbol{U}}_k\}$ of initial data is given. Assume that this set satisfies the conditions

1. $\bar{M}_k \in \langle -1, 1\rangle \quad \forall k$;
2. $\mathcal{J}(\mathcal{H}^-) < 0$, where

$$\mathcal{J}(\mathcal{H}) = \sum_{k=1}^{N} A_k \rho_k^*(\mathcal{H}) M_k^*(\mathcal{H}) = \sum_{k=1}^{N} A_k [\rho M]_k^*(\mathcal{H}) \tag{12}$$

and

$$\mathcal{H}^- = \max_k \mathcal{H}_k^*|_{\mathrm{R2}}(M_k^* = -1); \tag{13}$$

3. $\mathcal{J}(\mathcal{H}^+) > 0$, where

$$\mathcal{H}^+ = \min_k \mathcal{H}_k^*|_{\mathrm{S2}}(M_k^* = 1). \tag{14}$$

Such a set of initial data is said to belong to the **subsonic region**.

R2 and S2 denote rarefaction and shock wave of the second family, respectively. The notation indicates which of the wave equations that is used in $\mathcal{H}_k^*(M_k^*)$. Condition (1) is the obvious constraint of subsonic initial conditions in each pipe section. The two additional conditions set the limits for where the solutions are subsonic.

Then we may state the following:

Proposition 3. *Assume that the initial data $\bar{\boldsymbol{U}}_k$ belongs to the subsonic region in the sense of Definition 2.2 and that the momentum related coupling constant $\mathcal{H}$ is monotone in the sense of Definition 2.1. Then there exists a unique set of subsonic solutions satisfying RP0–RP2.*

Proof. Proposition 1 in [22] proves the uniqueness of a state $\boldsymbol{U}_k^*$ that satisfies RP0 for the conditions

1. The initial state $\bar{\boldsymbol{U}}_k$ is subsonic,
2. The momentum related coupling constant is monotone in the sense of Definition 2.1
3. The coupling constant value is given and satisfies

$$\mathcal{H}_k^*|_{R2}(M_k^* = -1) < \tilde{\mathcal{H}} < \mathcal{H}_k^*|_{S2}(M_k^* = 1). \tag{15}$$

The proof of the proposition is independent of the assumption on the cross-sectional area of each pipe section, and is hence valid for the generalized Riemann problem in the sense of Definition 1.1. As the last condition is satisfied for a set of initial data that belongs to the subsonic region, all three conditions are met. The uniqueness of a state $\boldsymbol{U}_k^*$ satisfying RP0 is thus proved.

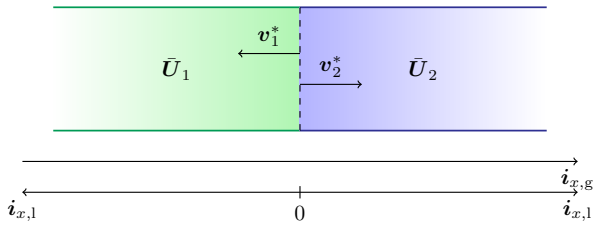

FIGURE 1. A junction with 2 connected pipes

Proposition 3 in [22] proves the uniqueness of the set of solutions $\{\boldsymbol{U}_k^*\}$ that satisfies RP0–RP2, given that the states $\boldsymbol{U}_k^*$ uniquely satisfies RP0 and that the set of solutions exist. Using the rarefaction and shock wave equations, it is proved that

$$\frac{\mathrm{d}[\rho M]_k^*}{\mathrm{d}\rho_k^*} > 0, \quad M_k^* \in \langle -1, 1 \rangle. \tag{16}$$

This implies that monotone coupling constants are as well monotone functions of the $[\rho M]_k^*$ variable. As the cross sectional area of each pipe section is a constant, we may therefore conclude that the total mass function $\mathcal{J}(\mathcal{H})$, as defined in Equation (12), is a monotonically increasing function of a monotone coupling constant, $\mathcal{H}$, in the sense of Definition 2.1. Thus Proposition 3 in [22] holds for the case of pipe sections with different cross-sectional areas.

As in [22], the definition of the subsonic region in Definition 2.2 guarantees the existence of the unique set of solutions. □

3. **The standard Riemann problem test case.** In addition to the monotonicity constraint (11), two requirements on the momentum related coupling constant are found by looking at the standard Riemann problem test case. In this test case two pipe sections of equal cross-sectional area are connected at a junction along the same axis, see Figure 1. Thus, the solution predicted by the network model must coincide with that of a Standard Riemann problem. The initial conditions in two such pipe sections are given as $\bar{\boldsymbol{U}}_1$ and $\bar{\boldsymbol{U}}_2$. Their boundary conditions at the pipe junction interfaces, Eq. (3), are $\boldsymbol{U}_1^*$ and $\boldsymbol{U}_2^*$, respectively.

The corresponding standard Riemann problem would have $\rho^{\mathrm{L}} = \bar{\rho}_1$, $v^{\mathrm{L}} = -\bar{v}_1$ and $\boldsymbol{U}^{\mathrm{R}} = \bar{\boldsymbol{U}}_2$ with a resulting intermediate state $\boldsymbol{U}^{\mathrm{m}}$. In the following we begin by identifying a set of $\{(\rho_k^*, v_k^*),\ k = 1, 2\}$, which correctly describes the intermediate state.

Lemma 3.1. *Consider isothermal flow. A network model for two pipe sections of equal cross-sectional area will predict the correct intermediate state $\boldsymbol{U}^{\mathrm{m}}$ of the corresponding standard Riemann problem if:*

$$\rho_1^* = \rho_2^* \tag{17}$$

and

$$-v_1^* = v_2^*. \tag{18}$$

That is:

$$\rho_2^* = \rho^{\mathrm{m}}, \tag{19}$$

$$v_2^* = v^{\mathrm{m}}. \tag{20}$$

Proof. The solutions to the standard Riemann problem is characterised by rarefaction and shock waves of the 1st and 2nd family (denoted R1, R2, S1 and S2):

$$R1: \quad v^{\mathrm{m}} = v^{\mathrm{L}} + a \ln \frac{\rho^{\mathrm{L}}}{\rho^{\mathrm{m}}} \tag{21}$$

$$R2: \quad v^{\mathrm{m}} = v^{\mathrm{R}} + a \ln \frac{\rho^{\mathrm{m}}}{\rho^{\mathrm{R}}} \tag{22}$$

$$S1: \quad v^{\mathrm{m}} = v^{\mathrm{L}} + a \left(\sqrt{\frac{\rho^{\mathrm{L}}}{\rho^{\mathrm{m}}}} - \sqrt{\frac{\rho^{\mathrm{m}}}{\rho^{\mathrm{L}}}} \right) \tag{23}$$

$$S2: \quad v^{\mathrm{m}} = v^{\mathrm{R}} + a \left(\sqrt{\frac{\rho^{\mathrm{m}}}{\rho^{\mathrm{R}}}} - \sqrt{\frac{\rho^{\mathrm{R}}}{\rho^{\mathrm{m}}}} \right) \tag{24}$$

In the network model, the boundary conditions are found from the equations:

$$R2_1: \quad v_1^* = \bar{v}_1 + a \ln \frac{\rho_1^*}{\bar{\rho}_1} = - \left(v^{\mathrm{L}} + a \ln \frac{\rho^{\mathrm{L}}}{\rho_1^*} \right) \tag{25}$$

$$R2_2: \quad v_2^* = \bar{v}_2 + a \ln \frac{\rho_2^*}{\bar{\rho}_2} = v^{\mathrm{R}} + a \ln \frac{\rho_2^*}{\rho^{\mathrm{R}}} \tag{26}$$

$$S2_1: \quad v_1^* = \bar{v}_1 + a \left(\sqrt{\frac{\rho_1^*}{\bar{\rho}_1}} - \sqrt{\frac{\bar{\rho}_1}{\rho_1^*}} \right) = - \left(v^{\mathrm{L}} + a \left(\sqrt{\frac{\rho^{\mathrm{L}}}{\rho_1^*}} - \sqrt{\frac{\rho_1^*}{\rho^{\mathrm{L}}}} \right) \right) \tag{27}$$

$$S2_2: \quad v_2^* = \bar{v}_2 + a \left(\sqrt{\frac{\rho_2^*}{\bar{\rho}_2}} - \sqrt{\frac{\bar{\rho}_2}{\rho_2^*}} \right) = v^{\mathrm{R}} + a \left(\sqrt{\frac{\rho_2^*}{\rho^{\mathrm{R}}}} - \sqrt{\frac{\rho^{\mathrm{R}}}{\rho_2^*}} \right) \tag{28}$$

Equation (25) to (28) are identical to Equation (21) to (24) if Equation (17) and (18) hold. Consequently Equation (19) and (20) are fulfilled. □

Next, we consider the momentum related coupling constant of the network model and identify two constraints:

Lemma 3.2. *Consider isothermal flow. The coupling conditions of a network model for two pipe sections of equal cross-sectional area reduces to the following set of equations:*

$$\rho_1^* v_1^* = - \rho_2^* v_2^*, \tag{29}$$

$$\mathcal{H}(\rho_1^*, v_1^*) = \mathcal{H}(\rho_2^*, v_2^*). \tag{30}$$

Equation (17) *and* (18) *form a unique solution to this set if and only if*

1. *$\mathcal{H}$ is a symmetric function of $\rho_k^* v_k^*$, that is*

$$\mathcal{H}(\rho_k^*, \rho_k^* v_k^*) = \mathcal{H}(\rho_k^*, -\rho_k^* v_k^*) \tag{31}$$

2. *$\mathcal{H}$ is a monotone function of ρ_k^* for constant $\rho_k^* v_k^*$, that is:*

$$\frac{\partial \mathcal{H}(\rho_k^*, \rho_k^* v_k^*)}{\partial \rho_k^*} > 0 \quad \text{or} \quad \frac{\partial \mathcal{H}(\rho_k^*, \rho_k^* v_k^*)}{\partial \rho_k^*} < 0 \quad \text{for } M_k^* \in \langle -1, 1 \rangle. \tag{32}$$

Proof. The existence of a unique relation between ρ_1^* and ρ_2^* is guaranteed by the monotonicity constraint (32). Symmetry in the $\rho_k^* v_k^*$ variable is required for Equation (17) to be a solution of the Equations (29) and (30). If one or both of the conditions are not met, Equation (17) and (18) does not form a unique solution to the Equations (29) and (30). □

Then we may state:

Proposition 4. *Consider fluid flow described by the isothermal Euler equations. A network model for two pipe sections of equal cross-sectional area, connected as in Figure 1, will correctly describe the standard Riemann problem if and only if the constraints* (31) *and* (32) *of Lemma 3.2 hold.*

Proof. Lemma 3.1 proves that if the network model predicts equal densities at the pipe-junction interfaces and velocities that are equal in absolute value and of opposite sign, then the solution will coincide with that of the standard Riemann problem. Lemma 3.2 proves that the network model will predict this kind of densities and velocities if and only if the two constraints on the momentum related coupling constant are met. □

A simple analysis, omitted here, show that pressure

$$\mathcal{H}(\rho, M) = \rho, \tag{33}$$

momentum flux

$$\mathcal{H}(\rho, M) = \rho\left(1 + M^2\right), \tag{34}$$

and Bernoulli invariant

$$\mathcal{H}(\rho, M) = \ln(\rho) + \frac{1}{2}M^2 \tag{35}$$

as momentum related coupling constant all fulfil the conditions set in Lemma 3.2. Hence they all correctly reproduce the solutions to the standard Riemann problem. Observe however that in this case, the entropy condition, RP3, is trivially satisfied. Therefore, studies involving junctions with more than two pipe sections are required if we wish to gain insight into the general entropy consistency of the various coupling constants.

4. Numerical implementation.

In this Section, we describe a numerical implementation of the network model. The approximate Riemann solver of Roe has been chosen, as it allows for easy extension to second-order accuracy for smooth solutions using the wave-limiter approach of LeVeque [18]. This approach is described in more detail in Section 4.2.

In Sections 4.3 and 4.4, we describe the boundary treatment needed to ensure that the coupling conditions are satisfied.

4.1. The approximate Riemann solver of Roe.

The set of equations governing the flow in each pipe is solved using the approximate Riemann solver of Roe [23]. The approximation is made by replacing the nonlinear problem (1) by a linearised problem at each cell interface [18]:

$$\frac{\partial \widehat{\boldsymbol{U}_k}}{\partial t} + \widehat{\boldsymbol{A}}_{i-1/2}\frac{\partial \widehat{\boldsymbol{U}_k}}{\partial x} = 0. \tag{36}$$

The Roe matrix, $\widehat{\boldsymbol{A}}_{i-1/2}$, must fulfil three conditions :

Condition 1. $\widehat{\boldsymbol{A}}_{i-1/2}$ must be diagonalisable and have real eigenvalues

Condition 2. $\widehat{\boldsymbol{A}}_{i-1/2} \to \boldsymbol{f}'(\tilde{\boldsymbol{U}})$ as $\boldsymbol{Q}_{\mathrm{i}-1}, \boldsymbol{Q}_{\mathrm{i}} \to \tilde{\boldsymbol{U}}$

Condition 3. $\widehat{\boldsymbol{A}}_{i-1/2}(\boldsymbol{Q}_i - \boldsymbol{Q}_{i-1}) = \boldsymbol{f}(\boldsymbol{Q}_i) - \boldsymbol{f}(\boldsymbol{Q}_{i-1})$

The conditions are set in order to ensure a hyperbolic system (Condition 1) that is consistent with the original conservation law (Condition 2). In addition $\mathcal{W}^p$ will be an eigenvector of $\widehat{\boldsymbol{A}}_{i-1/2}$ if the states $\boldsymbol{Q}_{i-1}$ and $\boldsymbol{Q}_i$ are connected by a single wave, $\mathcal{W}^p = \boldsymbol{Q}_i - \boldsymbol{Q}_{i-1}$, in the true Riemann solution (Condition 3). The last condition also guarantees that the selected scheme (39) is conservative [18].

For the isothermal Euler equations, the following matrix fulfils the conditions [24, Eq. (11.42) and Eq. (11.43)]:

$$\widehat{\boldsymbol{A}}_{i-1/2} = \begin{bmatrix} 0 & 1 \\ a^2 - \hat{v}^2 & 2\hat{v} \end{bmatrix}, \tag{37}$$

where

$$\hat{v} = \frac{\sqrt{\rho_i}v_i + \sqrt{\rho_{i-1}}v_{i-1}}{\sqrt{\rho_i} + \sqrt{\rho_{i-1}}}. \tag{38}$$

4.2. **Numerical algorithm.** Equation (39) describes the numerical algorithm, written on conservation form. The algorithm is based on Godunov's method, applied for non-linear systems. It contains both a conservative Roe flux, $\boldsymbol{\mathcal{F}}$, and a correction term, $\widetilde{\boldsymbol{F}}$, where the latter extends the algorithm to a high-resolutions method [18].

$$\boldsymbol{Q}_i^{n+1} = \boldsymbol{Q}_i^n - \frac{\Delta t}{\Delta x}\left(\boldsymbol{\mathcal{F}}(\boldsymbol{Q}_i^n, \boldsymbol{Q}_{i+1}^n) - \boldsymbol{\mathcal{F}}(\boldsymbol{Q}_{i-1}^n, \boldsymbol{Q}_i^n)\right) - \frac{\Delta t}{\Delta x}\left(\widetilde{\boldsymbol{F}}(\boldsymbol{Q}_i^n, \boldsymbol{Q}_{i+1}^n) - \widetilde{\boldsymbol{F}}(\boldsymbol{Q}_{i-1}^n, \boldsymbol{Q}_i^n)\right). \tag{39}$$

The conservative Roe flux is found using the Roe matrix $\widehat{\boldsymbol{A}}_{i-1/2}$:

$$\boldsymbol{\mathcal{F}}(\boldsymbol{Q}_{i-1}^n, \boldsymbol{Q}_i^n) = \frac{1}{2}(\boldsymbol{f}(\boldsymbol{Q}_i^n) + \boldsymbol{f}(\boldsymbol{Q}_{i-1}^n)) - \frac{1}{2}|\widehat{\boldsymbol{A}}_{i-1/2}|(\boldsymbol{Q}_i^n - \boldsymbol{Q}_{i-1}^n). \tag{40}$$

The matrix $|\widehat{\boldsymbol{A}}_{i-1/2}|$ is defined as [18]:

$$|\widehat{\boldsymbol{A}}_{i-1/2}| = \widehat{\boldsymbol{A}}_{i-1/2}^{+} - \widehat{\boldsymbol{A}}_{i-1/2}^{-}, \tag{41}$$

where

$$\widehat{\boldsymbol{A}}_{i-1/2}^{\pm} = \widehat{\boldsymbol{R}}_{i-1/2}\widehat{\boldsymbol{\Lambda}}_{i-1/2}^{\pm}\widehat{\boldsymbol{R}}_{i-1/2}^{-1}, \tag{42}$$

$$\widehat{\boldsymbol{\Lambda}}_{i-1/2}^{\pm} = \operatorname{diag}\left(\frac{1}{2}\left(\hat{\lambda}_{i-1/2} \pm |\hat{\lambda}_{i-1/2}|\right)\right), \tag{43}$$

and $\hat{\lambda}_{i-1/2}$ and $\widehat{\boldsymbol{R}}_{i-1/2}$ are the eigenvalues and right eigenvector matrix of $\widehat{\boldsymbol{A}}_{i-1/2}$, respectively.

The high-resolution correction terms are defined by Equation (44), where the limited wave $\widetilde{\mathcal{W}}_{i-1/2}^p$ is given by Equation (45). In this equation, each wave of the solution is modified by a limiter function $\phi(\theta)$.

$$\widetilde{\boldsymbol{F}}(\boldsymbol{Q}_{i-1}^n, \boldsymbol{Q}_i^n) = \frac{1}{2}\sum_{p=1}^{m}|s_{i-1/2}^p|\left(1 - \frac{\Delta t}{\Delta x}|s_{i-1/2}^p|\right)\widetilde{\mathcal{W}}_{i-1/2}^p. \tag{44}$$

$$\widetilde{\mathcal{W}}_{i-1/2}^p = \phi(\theta_{i-1/2}^p)\mathcal{W}_{i-1/2}^p. \tag{45}$$

In our implementation, the monotonized central-difference limiter function (MC limiter) was chosen:

$$\phi(\theta) = \max(0, \min((1+\theta)/2, 2, 2\theta)). \tag{46}$$

The ratio θ is found by:

$$\theta^p_{i-1/2} = \frac{\mathcal{W}^p_{I-1/2} \cdot \mathcal{W}^p_{i-1/2}}{\mathcal{W}^p_{i-1/2} \cdot \mathcal{W}^p_{i-1/2}}, \tag{47}$$

where the index I is defined as:

$$I = \begin{cases} i-1 & s^p_{i-1/2} \geq 0 \\ i+1 & s^p_{i-1/2} < 0 \end{cases}. \tag{48}$$

The waves, $\mathcal{W}^p_{i-1/2}$, may be calculated from the eigenvectors of the Roe matrix:

$$\boldsymbol{Q}_i - \boldsymbol{Q}_{i-1} = \sum_{p=1}^{m} \mathcal{W}^p_{i-1/2} = \sum_{p=1}^{m} \beta^p_{i-1/2} \hat{\boldsymbol{r}}^p_{i-1/2}, \tag{49}$$

where $\hat{\boldsymbol{r}}^p_{i-1/2}$ is the right eigenvector of $\widehat{\boldsymbol{A}}_{i-1/2}$ belonging to family p and

$$\boldsymbol{\beta}_{i-1/2} = \widehat{\boldsymbol{R}}^{-1}_{i-1/2}(\boldsymbol{Q}_i - \boldsymbol{Q}_{i-1}). \tag{50}$$

The wave speeds needed in Equation (44) and Equation (48) are defined as the eigenvalues belonging to the Roe matrix:

$$s^p_{i-1/2} = \hat{\lambda}^p_{i-1/2} \tag{51}$$

4.3. **The flux function at the junction boundary.** In our numerical model, all boundary conditions are managed using the ghost cell approach. We have chosen to extend the computational domain by one ghost cell at each end of a pipe section. At a boundary towards a junction, the boundary condition found from the network model, $\boldsymbol{U}^*_k$, is used to determine the ghost cell variables. By doing so, some special care must be taken about axis directions and the calculation of the flux across the boundary.

We denote the condition in cell i in the k-th pipe section at time $t = n\Delta t$ by $\boldsymbol{Q}^n_{i,k}$ and the ghost cell by $\boldsymbol{Q}^n_{\mathrm{GC},k}$. The ghost cell variables are updated according to Equation (52).

$$\boldsymbol{Q}^n_{\mathrm{GC},k} = \begin{bmatrix} \rho^*_k \\ (-1)^{j_k} \rho^*_k v^*_k \end{bmatrix}. \tag{52}$$

The variable j_k is used as an indicator of the relation between the global axis, $\boldsymbol{i}_{x,g}$, used in the numerical model and the local axis, $\boldsymbol{i}_{x,l}$, used by the network model at each junction:

$$j_k = \begin{cases} 0 & \text{if } \boldsymbol{i}_{x,g} = \boldsymbol{i}_{x,l}, \\ 1 & \text{if } \boldsymbol{i}_{x,g} = -\boldsymbol{i}_{x,l}. \end{cases} \tag{53}$$

When calculating the numerical flux across the pipe-junction boundary, it is necessary to ensure that the mass conservation coupling condition (5) is fulfilled for each junction. The selected approach is outlined below in Proposition 5.

Proposition 5. *Denote the internal grid cell which is closest to the junction boundary, $\boldsymbol{Q}^n_{\mathrm{SJ},k}$. The numerical network model will conserve the total mass if the upwind Godunov flux* (54) *is used at pipe junction interfaces:*

$$\boldsymbol{\mathcal{F}}_{\mathrm{tot}}(\boldsymbol{Q}^n_{\mathrm{GC},k}, \boldsymbol{Q}^n_{\mathrm{SJ},k}) = \begin{bmatrix} (-1)^{j_k} \rho^*_k v^*_k \\ \rho^*_k((v^*_k)^2 + a^2) \end{bmatrix}, \tag{54}$$

where

$$\boldsymbol{\mathcal{F}}_{\mathrm{tot}}(\boldsymbol{Q}^n_{\mathrm{GC},k}, \boldsymbol{Q}^n_{\mathrm{SJ},k}) = \boldsymbol{\mathcal{F}}(\boldsymbol{Q}^n_{\mathrm{GC},k}, \boldsymbol{Q}^n_{\mathrm{SJ},k}) + \widetilde{\boldsymbol{F}}(\boldsymbol{Q}^n_{\mathrm{GC},k}, \boldsymbol{Q}^n_{\mathrm{SJ},k}). \tag{55}$$

Proof. The numerical mass flux at a pipe-junction interface may be written as:

$$\boldsymbol{\mathcal{F}}_{\text{num}} = A_k \, \boldsymbol{\mathcal{F}}_{\text{tot}}(\boldsymbol{Q}^n_{\text{GC},k}, \boldsymbol{Q}^n_{\text{SJ},k})[1], \tag{56}$$

where $\boldsymbol{V}[h]$ is used as notation for the h-th element of the vector $\boldsymbol{V}$. Numerical conservation of mass at a junction is then expressed as:

$$\sum_{k\in(j_k=0)} A_k \boldsymbol{\mathcal{F}}_{\text{tot}}(\boldsymbol{Q}^n_{\text{GC},k}, \boldsymbol{Q}^n_{\text{SJ},k})[1] = \sum_{k\in(j_k=1)} A_k \boldsymbol{\mathcal{F}}_{\text{tot}}(\boldsymbol{Q}^n_{\text{GC},k}, \boldsymbol{Q}^n_{\text{SJ},k})[1]. \tag{57}$$

Using the selected flux (54), Equation (57) becomes:

$$\sum_{k\in(j_k=0)} A_k (-1)^0 \rho^*_k v^*_k = \sum_{k\in(j_k=1)} A_k (-1)^1 \rho^*_k v^*_k. \tag{58}$$

For a junction connecting N pipes this is equal to:

$$\sum_{k=1}^{N} A_k \rho^*_k v^*_k = 0, \tag{59}$$

which satisfies Equation (5). □

Remark 1. The Godunov flux (54) may be expressed as a corrected Roe flux [(40), (55)] if the correction term, $\widetilde{\boldsymbol{F}}$, is appropriately chosen. For a boundary at the left hand side of a computational domain we have:

$$\widetilde{\boldsymbol{F}}(\boldsymbol{Q}^n_{\text{GC},k}, \boldsymbol{Q}^n_{\text{SJ},k}) = \frac{1}{2}\left(\boldsymbol{f}(\boldsymbol{Q}^n_{\text{GC},k}) - \boldsymbol{f}(\boldsymbol{Q}^n_{\text{SJ},k})\right) + \frac{1}{2}|\widehat{\boldsymbol{A}}_{\text{SJ}-1/2,k}|\left(\boldsymbol{Q}^n_{\text{SJ},k} - \boldsymbol{Q}^n_{\text{GC},k}\right). \tag{60}$$

Similarly, at the right hand side of the domain the correction term is:

$$\widetilde{\boldsymbol{F}}(\boldsymbol{Q}^n_{\text{SJ},k}, \boldsymbol{Q}^n_{\text{GC},k}) = \frac{1}{2}\left(\boldsymbol{f}(\boldsymbol{Q}^n_{\text{GC},k}) - \boldsymbol{f}(\boldsymbol{Q}^n_{\text{SJ},k})\right) + \frac{1}{2}|\widehat{\boldsymbol{A}}_{\text{GC}-1/2,k}|\left(\boldsymbol{Q}^n_{\text{GC},k} - \boldsymbol{Q}^n_{\text{SJ},k}\right). \tag{61}$$

We may use Condition 3, presented in Section 4.1, and simplify Equation (60) and (61). Noticing that $\widehat{\boldsymbol{A}}_{i-1/2}$ may be written as:

$$\widehat{\boldsymbol{A}}_{i-1/2} = \widehat{\boldsymbol{A}}^+_{i-1/2} + \widehat{\boldsymbol{A}}^-_{i-1/2}, \tag{62}$$

and inserting the expression for $|\widehat{\boldsymbol{A}}_{i-1/2}|$ found in Equation (41), Equation (60) may be written as:

$$\begin{aligned}\widetilde{\boldsymbol{F}}(\boldsymbol{Q}^n_{\text{GC},k}, \boldsymbol{Q}^n_{\text{SJ},k}) &= -\frac{1}{2}\widehat{\boldsymbol{A}}_{\text{SJ}-1/2,k}\left(\boldsymbol{Q}^n_{\text{GC},k} - \boldsymbol{Q}^n_{\text{SJ},k}\right) + \frac{1}{2}|\widehat{\boldsymbol{A}}_{\text{SJ}-1/2,k}|\left(\boldsymbol{Q}^n_{\text{SJ},k} - \boldsymbol{Q}^n_{\text{GC},k}\right), \\ &= -\widehat{\boldsymbol{A}}^-_{\text{SJ}-1/2,k}\left(\boldsymbol{Q}^n_{\text{SJ},k} - \boldsymbol{Q}^n_{\text{GC},k}\right).\end{aligned} \tag{63}$$

Similarly, Equation (61) may be written as:

$$\widetilde{\boldsymbol{F}}(\boldsymbol{Q}^n_{\text{SJ},k}, \boldsymbol{Q}^n_{\text{GC},k}) = \widehat{\boldsymbol{A}}^+_{\text{GC}-1/2,k}\left(\boldsymbol{Q}^n_{\text{GC},k} - \boldsymbol{Q}^n_{\text{SJ},k}\right). \tag{64}$$

4.4. **Calculation of boundary conditions at pipe junction interfaces.** The implemented procedure calculating the boundary conditions is in accordance with the results in [22]. We consider the three different momentum related coupling constants; pressure (33), momentum flux (34) and Bernoulli invariant (35), which are all monotone in the sense of Definition 2.1 [22].

The inverted functions, density and velocity as function of the momentum related coupling constant, will depend on the appropriate wave equation. They are denoted $(\rho)_{\mathcal{R}}$,$(M)_{\mathcal{R}}$ and $(\rho)_{\mathcal{S}}$,$(M)_{\mathcal{S}}$ when rarefaction and shock wave equations are used, respectively. For a given coupling constant value, $\tilde{\mathcal{H}}$, the density, Mach number and mass flux at a pipe-junction interface may be calculated:

$$[\rho M]_k^*(\tilde{\mathcal{H}}) = \rho_k^*(\tilde{\mathcal{H}})M_k^*(\tilde{\mathcal{H}}) = \begin{cases} \rho_{\mathcal{R}}(\tilde{\mathcal{H}})M_{\mathcal{R}}(\tilde{\mathcal{H}}) & \text{if } \tilde{\mathcal{H}} < \mathcal{H}_k \\ \rho_k M_k & \text{if } \tilde{\mathcal{H}} = \mathcal{H}_k \\ \rho_{\mathcal{S}}(\tilde{\mathcal{H}})M_{\mathcal{S}}(\tilde{\mathcal{H}}) & \text{if } \tilde{\mathcal{H}} > \mathcal{H}_k. \end{cases} \tag{65}$$

Numerically, the inverted function values are found by iteration on the function

$$\mathcal{I}_{M_k^*}(\tilde{\mathcal{H}}) = \mathcal{H}_k^*\left(M_k^*\right) - \tilde{\mathcal{H}} = 0. \tag{66}$$

Here the appropriate wave equation is used to describe the relation between the conditions of the ghost cell, $\boldsymbol{Q}_{\mathrm{GC},k}^n = [\rho_k^*, \rho_k^* v_k^*]^T$, and of the nearby internal cell, $\boldsymbol{Q}_{\mathrm{SJ},k}^n = [\bar{\rho}_k, \bar{\rho}_k \bar{v}_k]^T$, which is regarded as initial condition of the pipe section.

A Newton-Raphson algorithm is used to solve (66), utilising that the derivative $d\mathcal{H}_k^*/dM_k^*$ is known. If the algorithm fails, a bisection method is used on the interval $M_k^* \in [-1, 1]$.

The total mass flux function is defined by Equation (12). Using this equation together with the inverted mass flux function (65), we calculate $\mathcal{J}(\mathcal{H}^-)$ and $\mathcal{J}(\mathcal{H}^+)$, see Equation (13) and (14). If the set of initial states, $\{\boldsymbol{Q}_{\mathrm{SJ},k}^n\}$, belong to the subsonic region in the sense of Definition 2.2, a solution may be calculated. This is done with the aid of a bisection method on the interval $\tilde{\mathcal{H}} \in [\mathcal{H}^-, \mathcal{H}^+]$.

5. Numerical results.

The impact of the selected momentum related coupling constant will be explored using two different network configurations. The first configuration, a closed system consisting of three pipes and two junctions, will be used to show how the selected constant affects the energy of the system. The second configuration, an open system of 16 pipes connected in a network, will be used to show how the coupling constant influences the steady state flow situation in the network.

In all cases, the fluid speed of sound is set to $a = 300\,\mathrm{m/s}$.

5.1. **Simulations on a closed network.** An outline of the closed network configuration is shown in Figure 2. Three pipe sections, labelled S1 to S3, each of length $L = 50\,\mathrm{m}$, are connected by two junctions. All pipe sections are assumed to have equal cross-sectional areas. The global axis direction, $\boldsymbol{i}_{\mathrm{g}}$, is set in the direction from junction J1 to junction J2, as indicated in the figure. It should be noted that for junction J2, the global axis and the local axis, $\boldsymbol{i}_{\mathrm{l}}$, that is applied by the network theory are of opposite directions, see Figure 2b.

Initially, each pipe is filled with stagnant fluid of uniform pressure, with different pressure levels in each pipe. Two different sets of initial pressures have been selected. These are shown in Table 1.

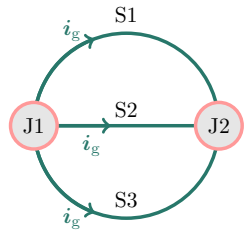

(A) Principal diagram

(B) Relation between the global axis, $\boldsymbol{i}_g$, and the local axis, $\boldsymbol{i}_l$, used by the network model.

FIGURE 2. Closed system consisting of three pipe sections and two junctions. All pipe sections are modelled as straight pipes.

Section	CS # 1		CS # 2	
	p [bar]	v [m/s]	p [bar]	v [m/s]
1	1.0	0.0	1.0	0.0
2	1.5	0.0	1.5	0.0
3	1.6	0.0	2.34	0.0

TABLE 1. Initial conditions, closed network cases

5.1.1. *Comparison of analytic and simulation results.* Grid refinement results for the two sets of initial data are shown in Figure 3 and Figure 4. The simulations were run until $T = 0.06\,\mathrm{s}$. For simplicity, only results for the first pipe-section are presented, and only for pressure as momentum related coupling constant. The results for the other coupling constants and pipe sections are however similar.

The analytical pressure- and velocity profiles, shown in the figures 3a, 3b, 4a and 4b are calculated using the wave equations for rarefaction and shock waves of the second family. If $\boldsymbol{U}_k^*$ and $\bar{\boldsymbol{U}}_k$ are connected by a rarefaction wave, Equation (67)

and (68) describe the density and velocity profiles in the pipe section.

$$\rho_k(x,t) = \begin{cases} \rho_k^* & \text{if } 0 \leq x < \lambda_2(\rho_k^*, v_k^*)t, \\ \bar{\rho} e^{\left(\frac{x-\bar{v}t}{at} - 1\right)} & \text{if } \lambda_2(\rho_k^*, v_k^*)t \leq x < \lambda_2(\bar{\rho}, \bar{v})t \ , \\ \bar{\rho} & \text{if } \lambda_2(\bar{\rho}, \bar{v})t \leq x \end{cases} \tag{67}$$

$$v_k(x,t) = \begin{cases} v_k^* & \text{if } 0 \leq x < \lambda_2(\rho_k^*, v_k^*)t, \\ \frac{x}{t} - a & \text{if } \lambda_2(\rho_k^*, v_k^*)t \leq x < \lambda_2(\bar{\rho}, \bar{v})t \ . \\ \bar{v} & \text{if } \lambda_2(\bar{\rho}, \bar{v})t \leq x \end{cases} \tag{68}$$

$$\tag{69}$$

In these equations, λ_2 is the eigenvalue of the second family:

$$\lambda_2(\rho, v) = v + a. \tag{70}$$

Equation (71) and (72) describe the profiles when the two states are connected by a shock wave.

$$\rho_k(x,t) = \begin{cases} \rho_k^* & \text{if } 0 \leq x < \left(\bar{v} + a\sqrt{\frac{\rho^*}{\bar{\rho}}}\right) t, \\ \bar{\rho} & \text{if } \left(\bar{v} + a\sqrt{\frac{\rho^*}{\bar{\rho}}}\right) t \leq x. \end{cases}, \tag{71}$$

$$v_k(x,t) = \begin{cases} v_k^* & \text{if } 0 \leq x < \left(\bar{v} + a\sqrt{\frac{\rho^*}{\bar{\rho}}}\right) t, \\ \bar{v} & \text{if } \left(\bar{v} + a\sqrt{\frac{\rho^*}{\bar{\rho}}}\right) t \leq x. \end{cases}. \tag{72}$$

Comparing analytical and numerical results, it is seen that only the lowest grid resolution leads to a significant deviation.

Figure 3c and Figure 4c present the development of total energy on a normalised form as a function of time. The numerical profiles are seen to converge towards a solution as the grid size is reduced. The exact solution, that is, the limit which the numerical results should converge to, is shown as "Analytic 1". The profile is derived as described in Observation 1 to Observation 3 and Equation (85), and relies on the condition that the two initial waves entering each pipe section have not yet interacted. This condition is satisfied at $T = 0.06\,\mathrm{s}$. The "Analytic 2" profile is derived in order to distinguish between physical and unphysical solutions. We will describe this further later in this section.

Observation 1. Each of the pipe sections shown in Figure 2 has an interface towards a junction in both ends. Denote the boundary conditions at these two pipe-junction interfaces of pipe section k, as $\boldsymbol{U}^{\mathrm{b}}_{k,\mathrm{J1}}$ and $\boldsymbol{U}^{\mathrm{b}}_{k,\mathrm{J2}}$. Note that both conditions relate to the global axis, $\boldsymbol{i}_{\mathrm{g}}$. Then, for the closed configuration shown in Figure 2 the following holds:

$$\rho^{\mathrm{b}}_{k,\mathrm{J1}} = \rho^{\mathrm{b}}_{k,\mathrm{J2}} \qquad \forall k \in 1,2,3, \tag{73}$$

$$v^{\mathrm{b}}_{k,\mathrm{J1}} = -v^{\mathrm{b}}_{k,\mathrm{J2}} \qquad \forall k \in 1,2,3. \tag{74}$$

Proof. Figure 2 shows that the two junctions with connected pipes have the same initial conditions. Hence,

$$|\boldsymbol{U}^{\mathrm{b}}_{k,\mathrm{J1}}| = |\boldsymbol{U}^{\mathrm{b}}_{k,\mathrm{J2}}| \qquad \forall k \in 1,2,3. \tag{75}$$

However, as the directions of the global axis and the local axis used by the network theory are opposite at the second junction, $J2$, the velocities are related by Equation (74). □

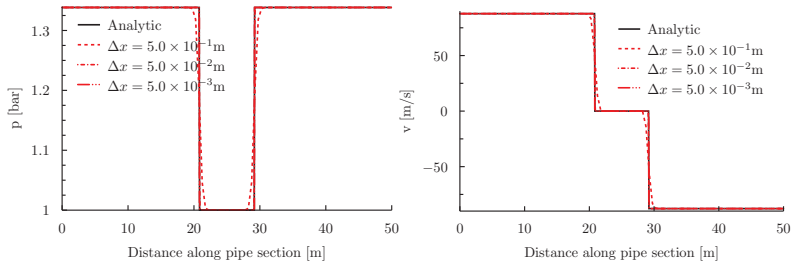

(A) Pressure - pipe section 1

(B) Velocity - pipe section 1

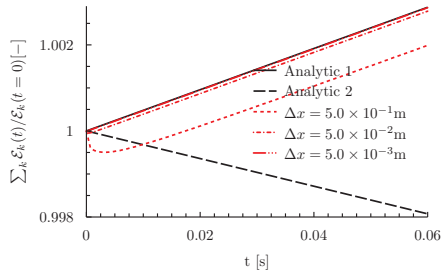

(C) Total energy relative to initial condition. The increase in total energy is due to unphysical energy production in the junctions.

FIGURE 3. CS #1, Section 1: Comparison between numerical and analytical results. ($\tilde{\mathcal{H}} = \rho$, $T = 0.06\,\mathrm{s}$)

Observation 2. Denote boundary conditions as in Observation 1 and consider the closed configuration shown in Figure 2. A pipe section containing two rarefaction waves that has not yet interacted has the following energy-content as a function of time:

$$\mathcal{E}_{k,2\times\mathrm{R2}}(t) = \mathcal{E}_k(t=0) + 2v^{\mathrm{b}}_{k,\mathrm{J1}}\rho^{\mathrm{b}}_{k,\mathrm{J1}}\left(\frac{1}{2}(v^{\mathrm{b}}_{k,\mathrm{J1}})^2 + a^2\left(\ln\left(\rho^{\mathrm{b}}_{k,\mathrm{J1}}\right)+1\right)\right)t \tag{76}$$

Proof. Energy and energy flux is an entropy entropy-flux pair for the isothermal Euler equations. [11, p. 212] Thus the entropy condition for a pipe section is given by Equation (77), with energy, E, defined by Equation (78).

$$\frac{\partial E}{\partial t} + \frac{\partial}{\partial x}(v(E+p)) \leq 0, \tag{77}$$

$$E = \frac{1}{2}\rho v^2 + \rho a^2 \ln(\rho). \tag{78}$$

In the present case, the pipe section only contains rarefaction waves. For such a smooth solution Equation (77) shows that energy is conserved:

$$\frac{\partial E_k}{\partial t} + \frac{\partial}{\partial x}\left(v_k\rho_k\left(\frac{1}{2}v_k^2 + a^2(\ln(\rho_k)+1)\right)\right) = 0. \tag{79}$$

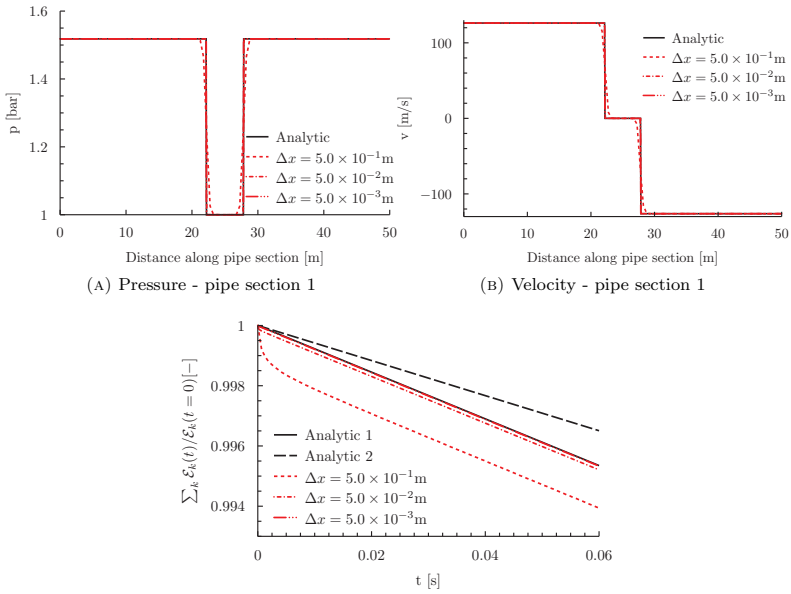

(A) Pressure - pipe section 1

(B) Velocity - pipe section 1

(C) Total energy relative to initial condition

FIGURE 4. CS #2, Section 1: Comparison between numerical and analytical results. ($\tilde{\mathcal{H}} = \rho$, $T = 0.06\,\mathrm{s}$)

Integration along the pipe section from the interface towards J1 to the interface towards J2 gives

$$\begin{aligned}
&\int_{\mathrm{J1}}^{\mathrm{J2}} \frac{\partial E_k}{\partial t}\,\mathrm{d}x + \int_{\mathrm{J1}}^{\mathrm{J2}} \frac{\partial}{\partial x}\left(v_k\rho_k\left(\frac{1}{2}v_k^2 + a^2(\ln(\rho_k)+1)\right)\right)\mathrm{d}x \\
=&\frac{\mathrm{d}\mathcal{E}_k}{\mathrm{d}t} + v^{\mathrm{b}}_{k,\mathrm{J2}}\rho^{\mathrm{b}}_{k,\mathrm{J2}}\left(\frac{1}{2}(v^{\mathrm{b}}_{k,\mathrm{J2}})^2 + a^2(\ln(\rho^{\mathrm{b}}_{k,\mathrm{J2}})+1)\right) \\
&- v^{\mathrm{b}}_{k,\mathrm{J1}}\rho^{\mathrm{b}}_{k,\mathrm{J1}}\left(\frac{1}{2}(v^{\mathrm{b}}_{k,\mathrm{J1}})^2 + a^2(\ln(\rho^{\mathrm{b}}_{k,\mathrm{J1}})+1)\right) \\
=&0.
\end{aligned} \tag{80}$$

Using the results in Observation 1 and integrating from 0 to t gives the result in equation (76). □

Observation 3. Denote boundary conditions as in Observation 1, the initial condition in the pipe as $\bar{\boldsymbol{U}}_k$ and consider the closed configuration shown in Figure 2. A pipe section containing two shock waves that have not yet interacted has the

following energy-content as a function of time:

$$\begin{aligned}&\mathcal{E}_{k,2\times \mathrm{S2}}(t)\\ =&\bar{\rho}a^2\ln(\bar{\rho})L\\ &+2a\sqrt{\frac{\rho^{\mathrm{b}}_{k,\mathrm{J1}}}{\bar{\rho}_k}}\left(\frac{1}{2}\rho^{\mathrm{b}}_{k,\mathrm{J1}}(v^{\mathrm{b}}_{k,\mathrm{J1}})^2+a^2\left(\rho^{\mathrm{b}}_{k,\mathrm{J1}}\ln(\rho^{\mathrm{b}}_{k,\mathrm{J1}})-\bar{\rho}_k\ln(\bar{\rho}_k)\right)\right)t,\end{aligned} \tag{81}$$

where L is the length of the pipe section.

Proof. Denote the speed of the shock waves emerging from the interfaces towards J1 and J2 by $s_{k,\mathrm{J1}}$ and $s_{k,\mathrm{J2}}$, respectively. Due to symmetry, the relation between the speeds may be found as:

$$s_{k,\mathrm{J1}}=-s_{k,\mathrm{J2}}=\bar{v_k}+a\sqrt{\frac{\rho^{\mathrm{b}}_{k,\mathrm{J1}}}{\bar{\rho}_k}}=a\sqrt{\frac{\rho^{\mathrm{b}}_{k,\mathrm{J1}}}{\bar{\rho}_k}}. \tag{82}$$

The final expression in (82) is obtained when taking into account that the initial velocity is zero, see Table 1.

At a given time t, the two shock waves divide the pipe section into three regions. Closest to the pipe-junction interface the conditions are given by $\boldsymbol{U}^{\mathrm{b}}_{k,\mathrm{J1}}$ and $\boldsymbol{U}^{\mathrm{b}}_{k,\mathrm{J2}}$, respectively. The mid-region is given by $\bar{\boldsymbol{U}}_k$. Total energy is found by summation of energy in each region:

$$\mathcal{E}_{k,2\times \mathrm{S2}}(t)=\bar{E}_k\left(L-s_{k,\mathrm{J1}}t+s_{k,\mathrm{J2}}t\right)+E^{\mathrm{b}}_{k,\mathrm{J1}}s_{k,\mathrm{J1}}t-E^{\mathrm{b}}_{k,\mathrm{J2}}s_{k,\mathrm{J2}}t, \tag{83}$$

where energy, E, is defined by Equation (78). Inserting the results from Observation 1 and Equation (82), we may write:

$$\mathcal{E}_{k,2\times \mathrm{S2}}(t)=\bar{E}_kL+2s_{k,\mathrm{J1}}t(E^{\mathrm{b}}_{k,\mathrm{J1}}-\bar{E}_k). \tag{84}$$

Equation (81) is found by inserting the expressions for $\bar{E}_k$, $E^{\mathrm{b}}_{k,\mathrm{J1}}$ and $s_{k,\mathrm{J1}}$ (82) into Equation (84). □

The total energy may then be found by summation:

$$\mathcal{E}_{\mathrm{An1}}(t)=\sum_{k\in R2}\mathcal{E}_{k,2\times \mathrm{R2}}(t)+\sum_{k\in S2}\mathcal{E}_{k,2\times \mathrm{S2}}(t), \tag{85}$$

where $R2$ is the subset of pipes containing rarefaction waves, and $S2$ is the subset containing shock waves.

The "Analytic 1" profile is compared with the numerical results (see Figure 3c and Figure 4c), in order to determine the appropriate grid size. The results show that only at the smallest grid size, $\Delta x = 5.0\times10^{-3}\,\mathrm{m}$, the deviation from the analytical profile is negligible. All further results presented for this configuration are therefore obtained using this grid size.

The second curve, denoted "Analytic 2", is used to determine if the numerically obtained solution is entropic in terms of Definition 1.2. These solutions are characterised by the absence of energy production in the junctions. In order to identify energy production or dissipation in the junctions, we need to account for the energy development in each of the pipe sections. Looking at the entropy condition in Equation (77) we see that pipe sections containing shock waves will have a reduced energy content as a function of time. This energy loss may be calculated as shown in Equation (86). By subtracting this loss from the total initial energy, as shown in

Equation (87), we may calculate the total energy of the system for conditions with no energy dissipation or production in the junctions.

$$\mathcal{E}_{k,d}(t) = \mathcal{E}_{k,2\times \mathrm{R2}}(t) - \mathcal{E}_{k,2\times \mathrm{S2}}(t). \tag{86}$$

$$\mathcal{E}_{\mathrm{An2}}(t) = \sum_{k=1}^{N} \left(\mathcal{E}_k(t=0) - \mathcal{E}_{k,d}(t)\right). \tag{87}$$

Entropic solutions are then characterised by:

$$\mathcal{E}_{\mathrm{An2}}(t) \geq \mathcal{E}_{\mathrm{An1}}(t) \tag{88}$$

Otherwise there is energy production in the junctions.

We use this criterion (88) to investigate the numerical results presented in Figure 3c and Figure 4c. It is clearly seen that the network model with pressure as momentum related coupling constant yields an entropic solution only for the second set of initial data. For the first set of initial data, the model predicts a condition with energy production in the junctions.

Next, we present results for all three momentum related coupling constants. Figure 5 and Figure 7 show the pressure and velocity profiles in each of the pipe sections at $T = 0.06\,\mathrm{s}$. The corresponding energy profiles are shown in Figure 6 and Figure 8. As expected, only the choice of Bernoulli invariant as momentum related coupling constant leads to energy conservation at the junctions. The duality between the two momentum related constants, pressure and momentum flux, is as well as expected [22]. For the first set of initial data, pressure as constant results in energy production at the junctions, while equal momentum flux gives energy dissipation. For the second set of initial data this is the other way around.

5.1.2. *Development of total energy as a function of time.* A second set of simulations were run until $T = 1.00\,\mathrm{s}$. Within this time-frame the first set of waves entering each pipe section interact, the resulting waves propagate out of the pipe sections and into the junctions, new waves are created and re-enter each pipe section and so forth. The resulting energy profiles for the two selected cases are shown in Figure 9. As seen, there is a net reduction of total energy for all three momentum related coupling constants. However, the profiles for pressure and momentum flux as coupling constant are not decreasing monotonically. This is due to the direction of the pipe flows. For instance we may consider the profile for pressure as coupling constant in Figure 9a. From $T = 0.00\,\mathrm{s}$ to $T \simeq 0.17\,\mathrm{s}$ there is an increase in total energy. At $T \simeq 0.17\,\mathrm{s}$ there is a significant change in the profile and the total energy is decreasing. At $T = 0.00\,\mathrm{s}$ the first set of waves enter the pipe sections. Relative to the local axis at the junctions, two pipe sections have boundary conditions with negative flow velocity, one pipe section has positive boundary velocity. As seen in Figure 3c, this implies energy production for a network model having pressure as coupling constant. At $T \simeq 0.17\,\mathrm{s}$ the second set of waves enter the pipe sections. In this set, the flow velocities are of opposite sign compared to the first set. Thus, two pipe sections have boundary conditions with positive flow velocity, one pipe section has negative boundary velocity. For the selected coupling constant this implies energy dissipation at the junctions, which explains the significant change from increasing to decreasing total energy seen in Figure 9.

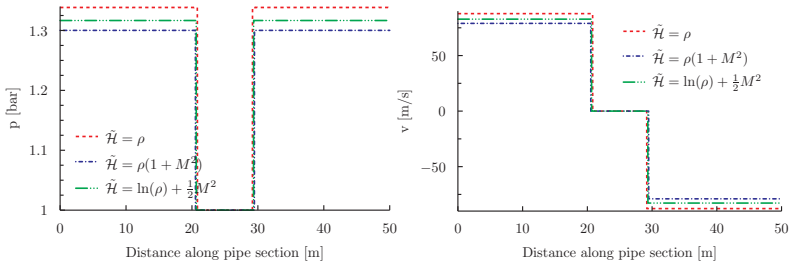

(A) Pressure - pipe section 1 (B) Velocity - pipe section 1

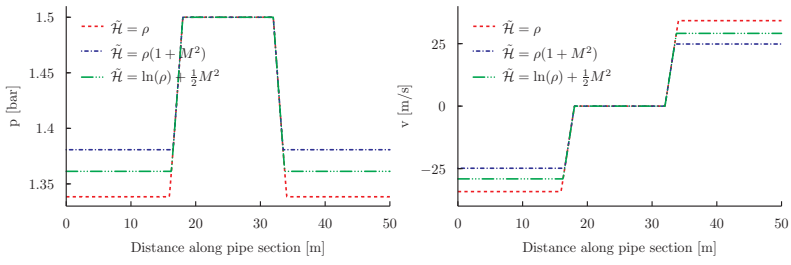

(C) Pressure - pipe section 2 (D) Velocity - pipe section 2

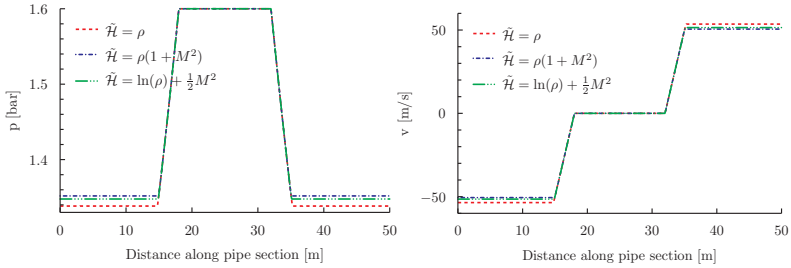

(E) Pressure - pipe section 3 (F) Velocity - pipe section 3

FIGURE 5. CS #1, Results at $T = 0.06\,\mathrm{s}$ for the three different momentum related coupling constants.

5.2. **Simulations on an open network.** An open network consisting of 16 pipe sections and eight junctions is connected to an unlimited source as shown in Figure 10. Each section is 50 m long and is initially filled with stagnant fluid at a pressure of 1.5 bar. The grid resolution is set to $\Delta x = 5.0 \times 10^{-1}\,\mathrm{m}$, based on a consideration of required CPU-time and the accuracy of the results. A simulation performed with a grid of $\Delta x = 5.0 \times 10^{-2}\,\mathrm{m}$ showed an insignificant change in the simulation results reported.

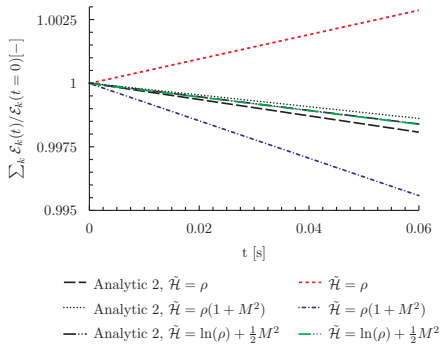

FIGURE 6. CS #1, Energy profiles for the three different momentum related coupling constants. The increase in energy for pressure as coupling constant, $\tilde{\mathcal{H}} = \rho$, is due to unphysical energy production in the junctions.

The source is connected at the inlet of pipe section S1 and holds a constant pressure of 2.0 bar. At $T = 0.0$ s, a membrane separating the source from the pipe is broken, and fluid is entering pipe section S1.

At $T = 10.0$ s, a stationary flow through the network is established. The flow conditions are evaluated using an integral analysis within a set of fixed boundaries. For any boundary the following holds if mass and energy is conserved:

$$\sum_{k \in S_i} A_k \rho_k v_k = \sum_{k \in S_o} A_k \rho_k v_k, \tag{89}$$

$$\sum_{k \in S_i} A_k v_k (E_k + p_k) = \sum_{k \in S_o} A_k v_k (E_k + p_k), \tag{90}$$

where S_i and S_o are the sets of pipe sections with flow direction into and out of the fixed boundary, respectively.

In our analysis we use four different boundaries, indicated as CV_1 to CV_4 in Figure 10. For each boundary we calculate the deviances:

$$M_{\text{ratio}} = \frac{\sum_{k \in S_o} A_k \rho_k v_k - \sum_{k \in S_i} A_k \rho_k v_k}{\sum_{k \in S_i} A_k \rho_k v_k}, \tag{91}$$

$$E_{\text{ratio}} = \frac{\sum_{k \in S_o} A_k v_k (E_k + p_k) - \sum_{k \in S_i} A_k v_k (E_k + p_k)}{\sum_{k \in S_i} A_k v_k (E_k + p_k)}, \tag{92}$$

based on densities, ρ_k and velocities, v_k that are averaged over all grid cells of each pipe section.

First we assume that the cross-sectional areas of all pipe sections are equal. The corresponding results are presented in Table 2. As seen, M_{ratio} deviates from zero. This is most probably due to minor deviations from steady state in one or more of the pipe sections. However, the effect of energy production and dissipation at the junctions is clearly seen from E_{ratio}. There is a significant difference between M_{ratio} and E_{ratio} for the boundaries CV_1, CV_2 and CV_3 for pressure and momentum flux as coupling constant. In the case of pressure as constant, there is energy dissipation

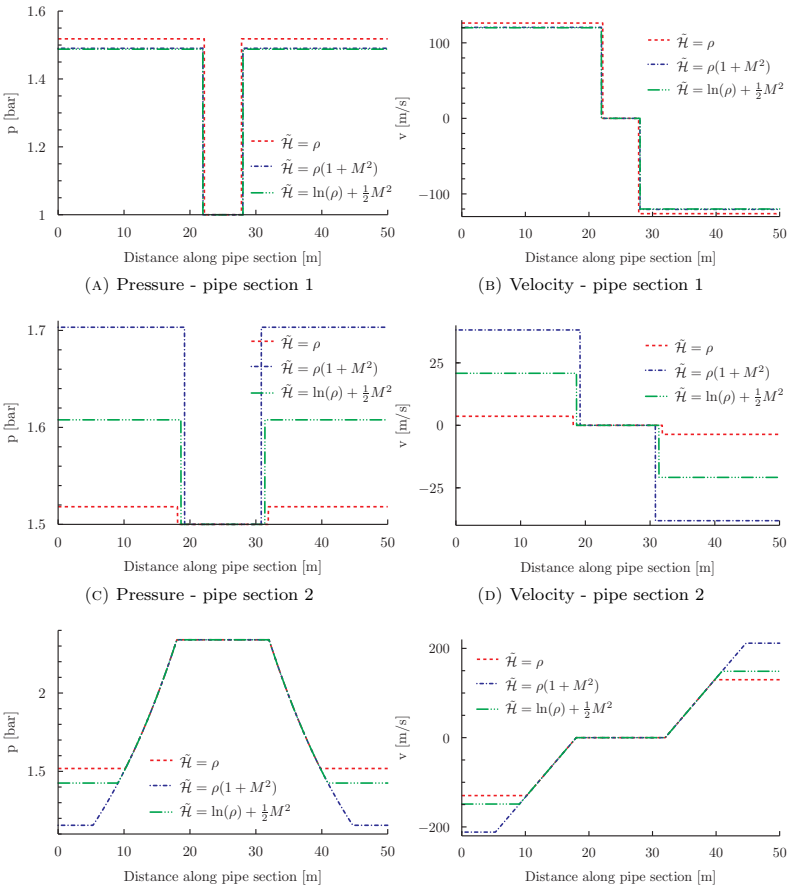

(A) Pressure - pipe section 1

(B) Velocity - pipe section 1

(C) Pressure - pipe section 2

(D) Velocity - pipe section 2

(E) Pressure - pipe section 3

(F) Velocity - pipe section 3

FIGURE 7. CS #2, Results at $T = 0.06\,\mathrm{s}$ for the three different momentum related coupling constants.

at the junctions J1 to J7. In the case of momentum flux as constant, energy is produced in the same junctions.

Looking at the last boundary, CV_4, we observe that the two deviances M_{ratio} and E_{ratio} are approximately equal for all three momentum related coupling constants. At this boundary the mass balance (89), the symmetry property of the momentum related coupling constant (31) and the application of the coupling constant (6) on

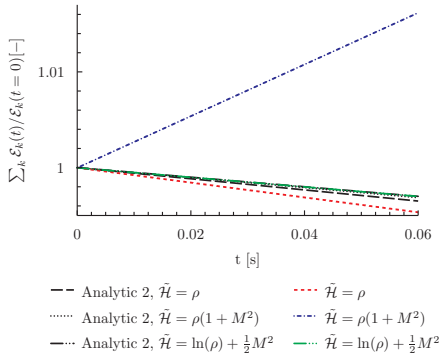

FIGURE 8. CS #2, Energy profiles for the three different momentum related coupling constants. The increase in energy for momentum flux as coupling constant, $\tilde{\mathcal{H}} = \rho\left(1 + M^2\right)$, is due to unphysical energy production in the junctions.

		$M_{\text{ratio}}[\%]$	$E_{\text{ratio}}[\%]$
$\mathcal{H}(\rho, M) = \rho$	CV_1	-0.0014	-0.47
	CV_2	-0.016	-0.60
	CV_3	-0.017	-0.63
	CV_4	-0.039	-0.039
$\mathcal{H}(\rho, M) = \rho(1 + M^2)$	CV_1	-0.0015	0.46
	CV_2	-0.013	0.56
	CV_3	-0.014	0.59
	CV_4	-0.031	-0.030
$\mathcal{H}(\rho, M) = \ln(\rho) + \frac{1}{2}M^2$	CV_1	-0.0017	-0.0015
	CV_2	-0.017	-0.017
	CV_3	-0.019	-0.019
	CV_4	-0.042	-0.042

TABLE 2. Steady state simulation results, open network where all pipe sections have equal cross-sectional areas.

loss-less pipe flow result in the following set of equations:

$$A_1 v_1 \rho_1 = A_{16} v_{16} \rho_{16}, \tag{93}$$

$$\mathcal{H}(\rho_1, v_1) = \mathcal{H}(\rho_{16}, v_{16}). \tag{94}$$

Due to the symmetry property of the coupling constant, the solution to this set of equations is identical to the solution to the Equations (29) and (30) found for the test case of a standard Riemann problem. Hence, for the CV_4 boundary, the three different momentum related coupling constants all yield entropic solutions.

The steady state pressure and velocity profiles for the pipe-sections are showed in Figure 11.

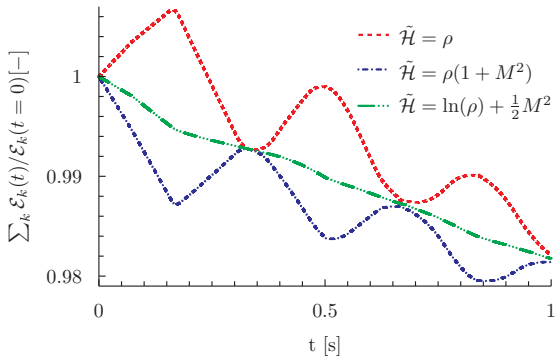

(A) CS # 1

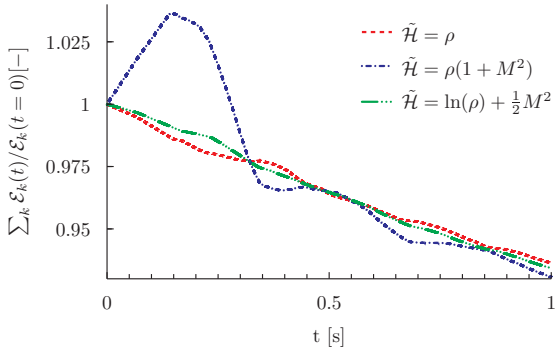

(B) CS # 2

FIGURE 9. Energy profiles for the three different momentum related coupling constants. Note that only Bernoulli invariant as momentum related coupling constant, $\tilde{\mathcal{H}} = \ln(\rho) + 1/2M^2$, yields a monotonically decreasing profile, as explained in Section 5.1.2.

Next we change the assumption of pipe sections of equal cross-sectional areas to the following:

$$A_{16} = A_1 \tag{95}$$

$$\sum_{k=2x}^{2x+1} A_k = A_x; \quad A_{2x} = A_{2x+1} \quad \text{for } x \in [1, 7]. \tag{96}$$

Meaning that at each junction, except J8, the cross sectional area of each of the outgoing pipe sections is half of the cross sectional area of the ingoing pipe.

The corresponding results are shown in Table 3. For this network there is no significant difference between the three momentum related constants and the deviances are negligible. An analysis on a junction connecting three pipe sections, similarly as in [22], shows why.

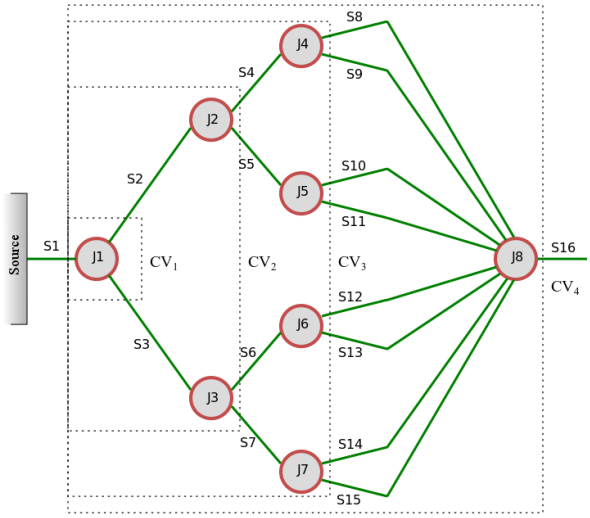

FIGURE 10. Open system consisting of 16 pipe sections and eight junctions. All pipe sections are modelled as straight pipes.

		M_{ratio}[-]	E_{ratio}[-]
$\mathcal{H}(\rho, M) = \rho$	CV_1	-3.8×10^{-9}	-3.8×10^{-9}
	CV_2	-6.9×10^{-9}	-6.6×10^{-9}
	CV_3	-2.7×10^{-10}	-9.2×10^{-10}
	CV_4	1.5×10^{-10}	-2.0×10^{-10}
$\mathcal{H}(\rho, M) = \rho(1 + M^2)$	CV_1	2.3×10^{-9}	1.4×10^{-9}
	CV_2	-2.9×10^{-9}	-3.1×10^{-9}
	CV_3	7.0×10^{-9}	7.1×10^{-9}
	CV_4	4.7×10^{-9}	5.0×10^{-9}
$\mathcal{H}(\rho, M) = \ln(\rho) + \frac{1}{2}M^2$	CV_1	-1.8×10^{-9}	-1.5×10^{-9}
	CV_2	-2.1×10^{-9}	-1.1×10^{-9}
	CV_3	-7.1×10^{-9}	-5.2×10^{-9}
	CV_4	-9.4×10^{-9}	-6.5×10^{-9}

TABLE 3. Steady state simulation results, open network with adjusted pipe cross-sectional areas as defined by the Equations (95) and (96).

Junction J1 with the connected pipe sections S1, S2 and S3 is representative for the junctions J1 to J7. These are the junctions impacting the results for CV_1 to CV_3. Due to the symmetry in the branches of the network, the velocities in the pipe sections S2 and S3 are equal. Observation 4 and Observation 5 shows that

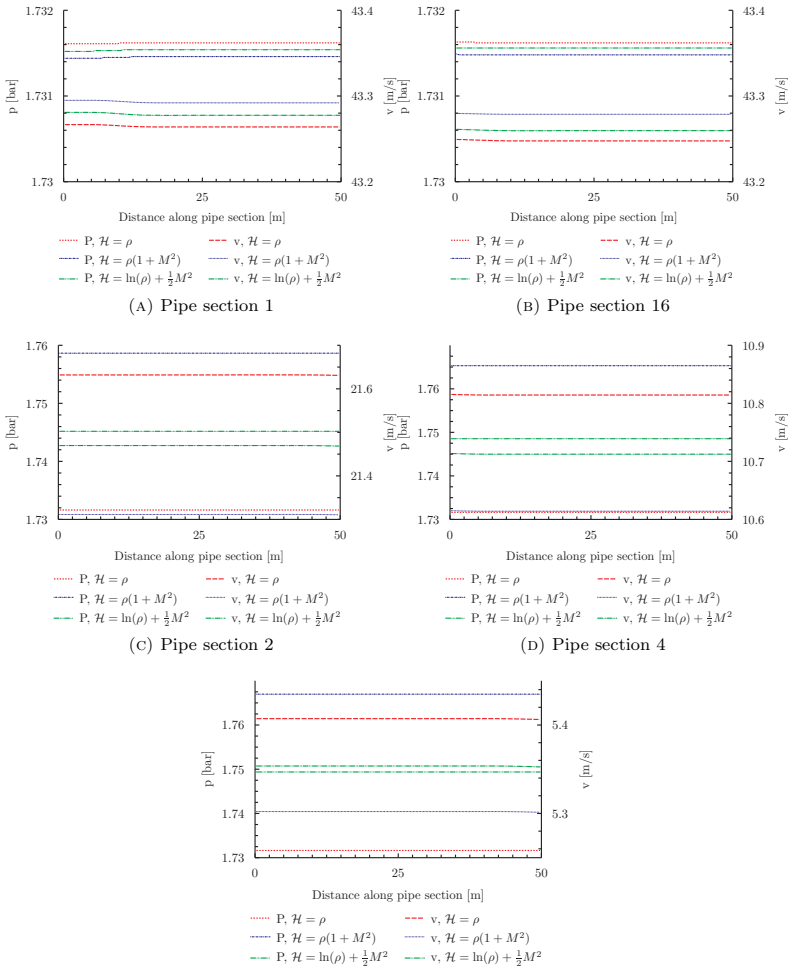

(A) Pipe section 1

(B) Pipe section 16

(C) Pipe section 2

(D) Pipe section 4

(E) Pipe section 8

FIGURE 11. Pressure and velocity profiles in each pipe section at $T = 10.0\,\mathrm{s}$ for the three different momentum related coupling constants.

network models using pressure or momentum flux as coupling constant yields energy conservation in the junctions due to the selected cross-sectional area ratios (95)-(96).

Observation 4. A network model using pressure as momentum related coupling constant (33) yields energy conservation in the junctions of Figure 10 for pipe sections with cross-sectional areas as described by the Equations (95) and (96).

Proof. We consider junction J1 with the connected pipe sections S1, S2 and S3. Mass conservation at the junction (5) may be expressed as:

$$\sum_{k=1}^{3} A_k \rho_k^* v_k^* = \tilde{\mathcal{H}} \sum_{k=1}^{3} A_k v_k^* = 0 \rightarrow \sum_{k=1}^{3} A_k v_k^* = 0 \tag{97}$$

Due to symmetry in the network, $A_2 = A_3$ and $v_2^* = v_3^*$. Then,

$$v_2^* = -\frac{A_1}{2A_2} v_1^*. \tag{98}$$

The entropy condition (7) becomes:

$$\begin{aligned} Q =& \sum_{k=1}^{3} A_k \rho_k^* v_k^* \left(\frac{1}{2} (v_k^*)^2 + a^2 \ln \frac{\rho_k^*}{\rho_0} \right) \\ =& \tilde{\mathcal{H}} \sum_{k=1}^{3} A_k v_k^* \left(\frac{1}{2} (v_k^*)^2 + a^2 \ln \frac{\tilde{\mathcal{H}}}{\rho_0} \right) \\ =& \frac{\tilde{\mathcal{H}}}{2} \sum_{k=1}^{3} A_k (v_k^*)^3, \end{aligned} \tag{99}$$

$$\begin{aligned} \hat{Q} =& \frac{2Q}{\tilde{\mathcal{H}}} \\ =& \sum_{k=1}^{3} A_k (v_k^*)^3 \\ =& A_1 (v_1^*)^3 + 2A_2 (v_2^*)^3 \\ =& A_1 (v_1^*)^3 + 2A_2 \left(-\frac{A_1}{2A_2} v_1^* \right)^3 \\ =& A_1 (v_1^*)^3 \left(1 - \frac{A_1^2}{4A_2^2} \right). \end{aligned} \tag{100}$$

From the final expression in (100) we see that energy is conserved in the junction for $v_1^* = 0$ and for $A_2 = {}^1\!/_2 A_1$. As seen from Equation (96), the last condition for energy conservation is fulfilled. □

Observation 5. A network model using momentum flux as momentum related coupling constant (34) yields energy conservation in the junctions of Figure 10 for pipe sections with cross-sectional areas as described in the Equations (95) and (96).

Proof. We consider junction J1 with the connected pipe sections S1, S2 and S3. Mass conservation at the junction (5) may be expressed as:

$$\sum_{k=1}^{3} A_k \rho_k^* v_k^* = \tilde{\mathcal{H}} a \sum_{k=1}^{3} A_k \frac{M_k^*}{1 + (M_k^*)^2} = 0 \rightarrow \sum_{k=1}^{3} A_k \frac{M_k^*}{1 + (M_k^*)^2} = 0 \tag{101}$$

Due to symmetry in the network, $A_2 = A_3$ and $v_2^* = v_3^*$. Then,

$$\frac{M_2^*}{1 + (M_2^*)^2} = -\frac{A_1}{2A_2} \frac{M_1^*}{1 + (M_1^*)^2}. \tag{102}$$

The entropy condition (7) becomes:

$$\begin{aligned}
Q =& \sum_{k=1}^{3} A_k \rho_k^* v_k^* \left(\frac{1}{2}(v_k^*)^2 + a^2 \ln \frac{\rho_k^*}{\rho_0} \right) \\
=& \sum_{k=1}^{3} A_k \frac{\tilde{\mathcal{H}}}{1+(M_k^*)^2} a M_k^* \left(\frac{1}{2}(v_k^*)^2 + a^2 \ln \frac{\frac{\tilde{\mathcal{H}}}{1+(M_k^*)^2}}{\rho_0} \right) \\
=& a^3 \tilde{\mathcal{H}} \sum_{k=1}^{3} A_k \frac{M_k^*}{1+(M_k^*)^2} \left(\frac{(M_k^*)^2 - 2\ln\left(1+(M_k^*)^2\right)}{2} \right),
\end{aligned} \tag{103}$$

$$\begin{aligned}
\hat{Q} =& \frac{Q}{a^3 \tilde{\mathcal{H}}} \\
=& \sum_{k=1}^{3} A_k \frac{M_k^*}{1+(M_k^*)^2} \left(\frac{(M_k^*)^2 - 2\ln\left(1+(M_k^*)^2\right)}{2} \right) \\
=& \sum_{k=1}^{3} A_k z_k(M_k^*) b_k(M_k^*) \\
=& A_1 z_1(M_1^*) b_1(M_1^*) + 2A_2 z_2(M_2^*) b_2(M_2^*) \\
=& A_1 z_1(M_1^*) b_1(M_1^*) + 2A_2 \left(-\frac{A_1}{2A_2} z_1(M_1^*) \right) b_2(M_2^*) \\
=& A_1 z_1(M_1^*) \left(b_1(M_1^*) - b_2(M_2^*) \right).
\end{aligned} \tag{104}$$

Energy conservation, $\hat{Q} = 0$, is obtained for two different conditions; $z_1 = 0$ and $b_1(M_1^*) = b_2(M_2^*)$. The first condition implies that $M_1^* = 0$. The second condition is fulfilled for $M_1^* = M_2^*$ and $M_1^* = -M_2^*$. In our case, the physically relevant solution is $M_1^* = -M_2^*$. From Equation (102) we see that this corresponds to the condition $A_1 = 2A_2$, which is fulfilled by Equation (96). □

Observation 4 and Observation 5 show that the velocities in each of the pipe sections are equal, if we refer to the global axis directed from the source to the outlet of pipe section 16. This is also the situation for the network model using Bernoulli invariant as coupling constant. Looking at the expressions for momentum flux and Bernoulli invariant as coupling constant, Equation (34) and (35), we see that this implies equal density, and thus equal pressure, too. For the present case the resulting pressure is $p = 1.7305\,\text{bar}$. The velocity is $v = 43.468\,\text{m/s}$.

6. **Summary.** We investigate solutions to the generalized Riemann problem for the isothermal Euler equations analytically and numerically. Restricted to monotone coupling constants and pipe sections of equal cross-sectional area, a proof of existence and uniqueness of such solutions was given in our previous work [22]. In the present paper we have expanded this proof to the case of pipe sections of different cross-sectional areas.

We have also compared the solution of a network model that describes a standard Riemann problem to the analytical solution of such a problem. The analysis lead to two constraints on the momentum related coupling constant; it must be symmetric in the ρv variable and monotone in the ρ variable.

A classical high-resolution Roe scheme is used to simulate the flow in each pipe section. For the pipe-junction interfaces we have proposed a numerical method

which ensures conservation of mass at the junctions. In our implementation, boundary conditions are generally managed using the ghost cell approach. At pipe-junction interfaces the ghost cell variables are thus set equal to the boundary condition predicted by the network model, $\boldsymbol{U}_k^*$. Conservation of mass at each junction is obtained by using the upwind Godunov flux as numerical flux function at the pipe-junction boundaries.

Numerical results are presented for two different network configurations; a closed system consisting of three pipe sections connected at two junctions and an open system consisting of pipe sections in a symmetrical branch-tree structure. The results are analysed with respect to entropy consistency. That is, the evaluation is performed by applying the entropy condition in order to determine if a solution is physically reasonable or not. This is done in order to evaluate the three different options for momentum related coupling constant used in the network model.

We present long-term simulation results, which show the impact of unphysical solutions predicted by the network models. For the closed system, this is seen as an increase in total energy at certain time intervals. For the open system, steady state energy fluxes are used to identify energy production in junctions.

Analytical predictions of entropy consistency for junctions connecting three pipe sections of equal cross-sectional areas were provided in [22]. Numerical results for such junctions, derived in the present paper, are in accordance with these predictions. They show that the options of pressure and momentum flux yields unphysical solutions for certain initial data. Only Bernoulli invariant as momentum related coupling constant yields entropic solutions for all the presented test cases.

Acknowledgements. This work was financed through the research project *Enabling low emission LNG systems*. The author acknoledges the project partners; Statoil and GDF SUEZ, and the Research Council of Norway (193062/S60) for support through the *Petromaks* programme.

The author also acknowledges valuable discussions with Tore Flåtten and his suggestions concerning the numerical implementation and analysis of the numerical results.

REFERENCES

[1] M. K. Banda, M. Herty and A. Klar, *Gas flow in pipeline networks*, Netw. Heterog. Media, **1** (2006), 41–56.

[2] M. K. Banda, M. Herty and A. Klar, *Coupling conditions for gas networks governed by the isothermal Euler equations*, Netw. Heterog. Media, **1** (2006), 295–314.

[3] M. K. Banda, M. Herty and J.-M. T. Ngnotchouye, *Toward a mathematical analysis for drift-flux multiphase flow models in networks*, SIAM J. Sci. Comput., **31** (2010), 4633–4653.

[4] M. K. Banda, M. Herty and J.-M. T. Ngnotchouye, *Coupling drift-flux models with unequal sonic speeds*, Math. Comput. Appl., **15** (2010), 574–584.

[5] J. Brouwer, I. Gasser and M. Herty, *Gas pipeline models revisited: model hierarchies, non-isothermal models, and simulations of networks*, Multiscale Model. Simul., **9** (2011), 601–623.

[6] G. M. Coclite, M. Garavello and B. Piccoli, *Traffic flow on a road network*, SIAM J. Math. Anal., **36** (2005), 1862-1886.

[7] R. M. Colombo and M. Garavello, *A well posed Riemann problem for the p-system at a junction*, Netw. Heterog. Media, **1** (2006), 495–511.

[8] R. M. Colombo and M. Garavello, *On the Cauchy problem for the p-system at a junction*, SIAM J. Math. Anal., **39** (2008), 1456–1471.

[9] R. M. Colombo, M. Herty and V. Sachers, *On 2 × 2 conservation laws at a junction*, SIAM J. Math. Anal., **40** (2008), 605–622.

[10] R. M. Colombo and C. Mauri, *Euler system for compressible fluids at a junction*, J. Hyperbol. Differ. Eq., **5** (2008), 547–568.

[11] C. M. Dafermos, "Hyperbolic Conservation Laws in Continuum Physics", 3rd edition, Springer-Verlag, 2010.
[12] M. Garavello, *A review of conservation laws on networks*, Netw. Heterog. Media, **5** (2010), 565–581.
[13] M. Herty, *Coupling conditions for networked systems of Euler equations*, SIAM J. Sci. Comput., **30** (2008), 1596–1612.
[14] M. Herty and M. Seaïd, *Simulation of transient gas flow at pipe-to-pipe intersections*, Netw. Heterog. Media, **56** (2008), 485–506.
[15] H. Holden and N. H. Risebro, *A mathematical model of traffic flow on a network of unidirectional roads*, SIAM J. Math. Anal., **26** (1995), 999–1017.
[16] S. W. Hong and C. Kim, *A new finite volume method on junction coupling and boundary treatment for flow network system analyses*, Int. J. Numer. Meth. Fluids, **65** (2011), 707–742.
[17] T. Kiuchi, *An implicit method for transient gas flows in pipe networks*, Int. J. Heat and Fluid Flow, **15** (1994), 378–383.
[18] R. J. LeVeque, "Finite Volume Methods for Hyperbolic Problems", 6th edition, Cambridge University Press, 2007.
[19] A. Osiadacz, *Simulation of transient gas flows in networks*, Int. J. Numer. Meth. Fluids, **4** (1984), 13–24.
[20] R. J. Pearson, M. D. Bassett, P. Batten and D. E. Winterbone, *Two-dimensional simulation of wave propagation in a three-pipe junction*, J. Eng. Gas Turbines Power, **122** (2000), 549–555.
[21] J. Pérez-García, E. Sanmiguel-Rojas, J. Hernández-Grau and A. Viedma, *Numerical and experimental investigations on internal compressible flow at T-type junctions*, Experimental Thermal and Fluid Science, **31** (2006), 61–74.
[22] G. A. Reigstad, T. Flåtten, N. E. Haugen and T. Ytrehus, *Coupling constants and the generalized Riemann problem for isothermal junction flow*, Submitted (2013), Preprint available at: *http://www.math.ntnu.no/conservation/2013/007.html*.
[23] P. L. Roe, *Approximate Riemann solvers, parameter vectors, and difference schemes*, Journal of Computational Physics, **43** (1981), 357–372.
[24] E. F. Toro, "Riemann Solvers and Numerical Methods for Fluid Dynamics", 3rd edition, Springer-Verlag, 2009.

E-mail address: Gunhild.Reigstad@ntnu.no

E

Paper IV - Numerical Investigation of Network Models for Isothermal Junction Flow

Authors: Gunhild A. Reigstad and Tore Flåtten

Extended version of paper submitted to *the ENUMATH 2013 Proceedings Volume (Springer)*, November 2013

NUMERICAL INVESTIGATION OF NETWORK MODELS FOR ISOTHERMAL JUNCTION FLOW

GUNHILD A. REIGSTAD[A,C] AND TORE FLÅTTEN[B]

Abstract. This paper deals with the issue of how to properly model fluid flow in pipe junctions. In particular, we investigate the numerical results from three alternative network models, all three based on the isothermal Euler equations. Using two different test cases, we focus on the physical validity of simulation results from each of the models. Unphysical solutions are characterised by the presence of energy production in junctions.

Our results are in accordance with previous conclusions; that only one of the the network models yields physical solutions for all subsonic initial conditions. The last test case shows in addition how the three models may predict fundamentally different waves for a given set of initial data.

Key words. gas flow, networks, junctions

AMS subject classification. 35L65, 76N15

1. Introduction

A network model describes the global weak solution of hyperbolic conservation laws defined on N segments of the real line that are connected at a common point. In addition to fluid flow in pipeline junctions, such models are used to describe for example traffic flow, data networks, and supply chains [4].

An example of a junction with N connected pipe sections is shown in Figure 1. Each pipe section is modelled along a local axis ($x \in \mathbb{R}^+$) and $x = 0$ at the pipe-junction interface. The problem is investigated by defining a generalized Riemann problem at the junction, and thus the condition of constant initial conditions in each pipe section is presupposed. The flow condition in each pipe section is found as the solution to the half-Riemann problem

$$\begin{aligned} \frac{\partial \boldsymbol{U}_k}{\partial t} + \frac{\partial}{\partial x}\boldsymbol{F}(\boldsymbol{U}_k) &= 0, \\ \boldsymbol{U}_k(x,0) &= \begin{cases} \bar{\boldsymbol{U}}_k & \text{if } x > 0 \\ \boldsymbol{U}_k^* & \text{if } x < 0, \end{cases} \end{aligned} \tag{1}$$

restricted to $x \in \mathbb{R}^+$. $\boldsymbol{U}_k^*$ is a constructed state, defined as

$$\boldsymbol{U}_k^*\left(\bar{\boldsymbol{U}}_1, \ldots, \bar{\boldsymbol{U}}_N\right) = \lim_{x \to 0^+} \boldsymbol{U}_k(x,t). \tag{2}$$

$\boldsymbol{U}_k^*$ is per definition connected to the initial condition, $\bar{\boldsymbol{U}}_k$, by waves of non-negative speed only. This ensures that the constructed state propagates into the pipe section.

Date: January 20, 2014.

[A]Dept. of Energy and Process Engineering, Norwegian University of Science and Technology (NTNU), NO-7491 Trondheim, Norway.

[B]SINTEF Materials and Chemistry, P.O. Box 4760 Sluppen, NO-7465 Trondheim.

Email: Gunhild.Reigstad@ntnu.no, Tore.Flatten@sintef.no.

[C]Corresponding author.

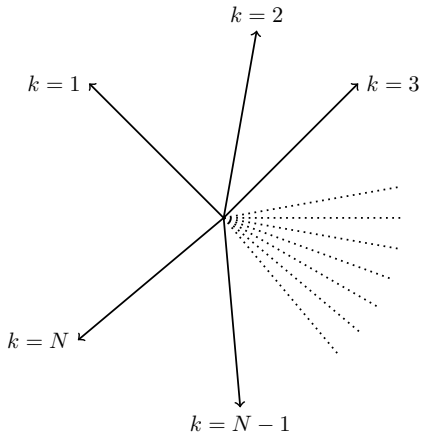

Figure 1. A junction with N connected pipe sections

In the present paper we consider the isothermal Euler equations, which are described by the isentropic conservation law

$$\frac{\partial}{\partial t}\begin{bmatrix}\rho\\ \rho v\end{bmatrix} + \frac{\partial}{\partial x}\begin{bmatrix}\rho v\\ \rho v^2 + p(\rho)\end{bmatrix} = \begin{bmatrix}0\\ 0\end{bmatrix}, \tag{3}$$

together with the pressure law

$$p(\rho) = a^2\rho. \tag{4}$$

Here ρ and v are the fluid density and velocity, respectively, $p(\rho)$ is the pressure and a is the constant speed of sound in the fluid. Initial conditions of standard Riemann problems are, for this set of equations, connected by two waves. Only waves of the second family have non-negative speed at subsonic conditions. Therefore $\boldsymbol{U}_k^*$ and $\bar{\boldsymbol{U}}_k$ are connected by either a rarefaction or a shock wave of this family [6].

In addition to the wave-equation describing the relation between $\boldsymbol{U}_k^*$ and $\bar{\boldsymbol{U}}_k$, a set of equations is needed for $\boldsymbol{U}_k^*$ to be uniquely defined. The equations are denoted *coupling conditions*, and for the isothermal Euler equations, they are related to mass and momentum

CC1: Mass is conserved at the junction

$$\sum_{k=1}^{N} \rho_k^* v_k^* = 0. \tag{5}$$

CC2: There is a unique, scalar momentum related coupling constant at the junction

$$\mathcal{H}(\rho_k^*, v_k^*) = \tilde{\mathcal{H}} \qquad \forall k \in \{1, \dots, N\}. \tag{6}$$

Three different expressions for the momentum related coupling constant are considered in this paper. Pressure (7) and momentum flux (8) have been frequently used in the literature [1, 2, 3, 5].

The Bernoulli invariant (9) was recently proposed [6].

$$\mathcal{H}(\rho_k^*, v_k^*) = \rho_k^* \tag{7}$$

$$\mathcal{H}(\rho_k^*, v_k^*) = \rho_k^* \left(1 + \left(\frac{v_k^*}{a}\right)^2\right) \tag{8}$$

$$\mathcal{H}(\rho_k^*, v_k^*) = \ln(\rho_k^*) + \frac{1}{2}\left(\frac{v_k^*}{a}\right)^2 \tag{9}$$

The suitability of a suggested momentum related coupling constant is evaluated according to two criteria. First, a standard Riemann problem in a pipe section of uniform cross sectional area may be modelled as two pipe sections connected at a junction. The resulting network model must then have a solution equal to the solution of the standard Riemann problem. This imposes a symmetry- and a monotonicity constraint on the momentum related coupling constant [7]. Second, the solutions of the network model must be physically reasonable. This is determined by the entropy condition (10), which states that energy production does not occur in a junction if the solution is physical.

$$E_{\text{crit}} = \sum_{k=1}^{N} \rho_k^* v_k^* \left(\frac{1}{2}(v_k^*)^2 + a^2 \ln \frac{\rho_k^*}{\rho_0}\right) \leq 0, \tag{10}$$

where ρ_0 is some reference density.

The entropy condition was first used by Colombo and Garavello [3] and is based on the mechanical energy flux function. The presented condition (10) is derived for the isothermal Euler equations.

An analytical investigation on the relation between the entropy condition and the momentum related coupling constant was previously performed for the special case of three pipe sections connected at a junction [6]. The analysis showed that for certain flow rates within the subsonic domain, both pressure (7) and momentum flux (8) as coupling constant yield unphysical solutions. Physical solutions for all subsonic flow rates were only guaranteed when the Bernoulli invariant (9) was used as coupling constant. In the present paper, two numerical test cases will be used to verify this analysis and to explore the behaviour of the different models.

The first test case consists of five pipe sections connected at a junction. The case illustrates how the network model easily may be applied to a junction connecting a large number of pipe sections. We will as well evaluate the results in terms of physical soundness using the entropy condition (10).

The second case consists of three pipe sections connected by two junctions such that a closed system is constructed. We will show how the different models produce fundamentally different results in terms of rarefaction and shock waves. The total energy of the system as a function of time will as well be presented in order to display the effect of having unphysical solutions.

2. Numerical Results

The fluid flow in each pipe section is solved by a classical approximate Riemann solver of Roe as described by Reigstad [7]. In the two test cases, the speed of sound in the fluid is set to $a = 300\,\text{m/s}$ and the Courant-Friedrichs-Lewy condition is set to $C = 0.5$.

2.1. Case 1: Five Pipe Sections Connected at a Junction.

Five pipe sections, each of length $L = 50\,\text{m}$ are connected at a single junction. The initial conditions of each pipe section are given in Table 1. Interaction between the fluids in the pipe sections first occur at $T = 0.0\,\text{s}$ and immediately afterwards one wave enters each section.

Pipe section	p [bar]	v [m/s]
1	1.00	0.0
2	1.20	0.0
3	1.30	0.0
4	1.50	0.0
5	1.60	0.0

Table 1. Case 1: Initial conditions

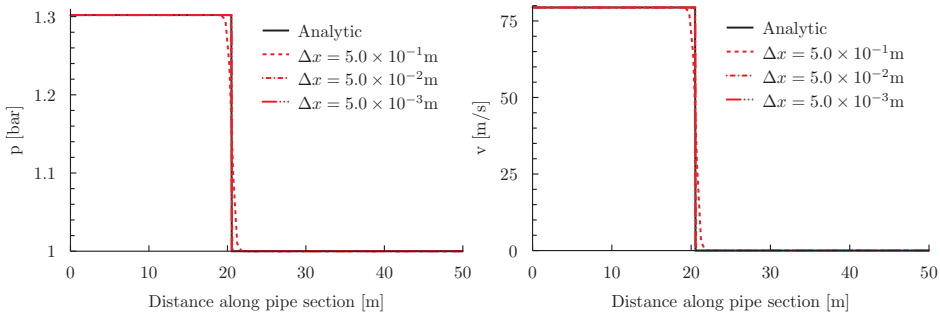

(a) Pressure - pipe section 1 **(b)** Velocity - pipe section 1

Figure 2. Case 1, pipe section 1: Comparison between numerical and analytical results. ($\tilde{\mathcal{H}} = \rho$, $T = 0.06\,\mathrm{s}$)

For a given set of initial conditions we may calculate the constructed states, $\boldsymbol{U}_k^*$, and the analytical velocity and pressure profiles at a given time as function of distance through the pipe section. Figure 2 compares such analytical profiles to simulation results performed with three different numerical grid resolutions. Only the lowest resolution of $\Delta x = 5.0 \times 10^{-1}\,\mathrm{m}$ produces profiles that deviates significantly from the analytical results. Thus, a grid resolution of $\Delta x = 5.0 \times 10^{-2}\,\mathrm{m}$ was chosen. The figure only presents results for the first pipe section, for pressure as momentum related coupling constant. The results are however comparable for the other coupling constants and pipe sections.

Figure 3 presents pressure and velocity profiles for each of the five pipe sections. Results are showed for each of the three momentum related coupling constants. As seen, the resulting boundary conditions differ, but the predictions of rarefaction and shock waves are consistent.

Our main focus is to evaluate the simulation results with the aid of the entropy condition (10). The results are shown in Figure 4. As expected, Bernoulli invariant as coupling constant yields energy conservation at the junction. The two other options lead to energy production at the junction for the given set of initial data. That is, the solutions are unphysical.

Analytically, the E_{crit} profile for a given set of initial conditions is a constant value. The deviation seen in Figure 4 is due to the numerical implementation, where the constructed state, $\boldsymbol{U}_k^*$, at a new time-step is calculated based on the calculated conditions in the inner grid cell closest to the interface, at the previous time-step. As the waves propagate into the pipe sections, the numerical $\boldsymbol{U}_k^*$ values will deviate from the analytical ones. However, the impact is temporary and the entropy function soon regains its initial value.

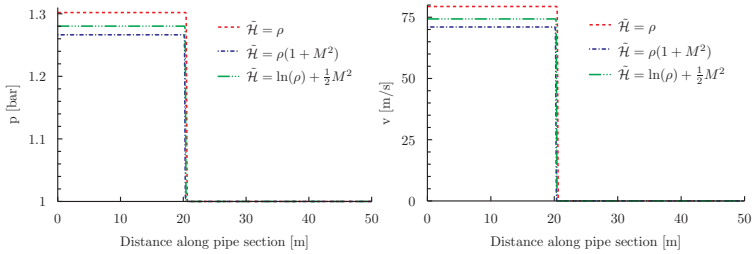

(a) Pressure - pipe section 1 **(b)** Velocity - pipe section 1

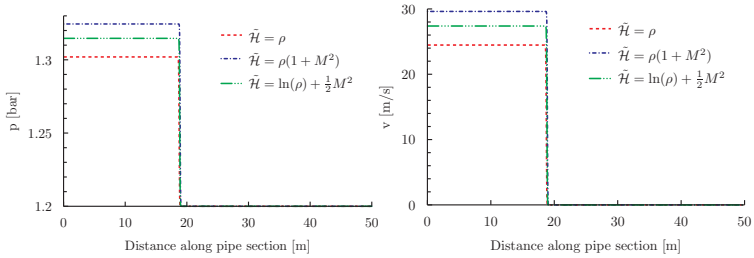

(c) Pressure - pipe section 2 **(d)** Velocity - pipe section 2

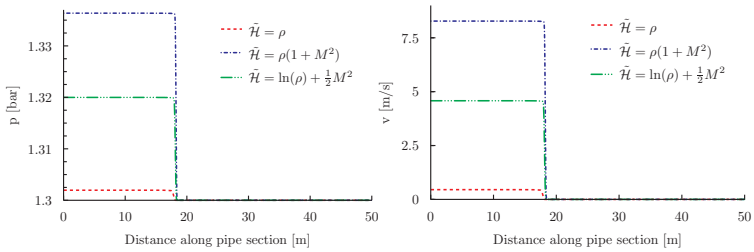

(e) Pressure - pipe section 3 **(f)** Velocity - pipe section 3

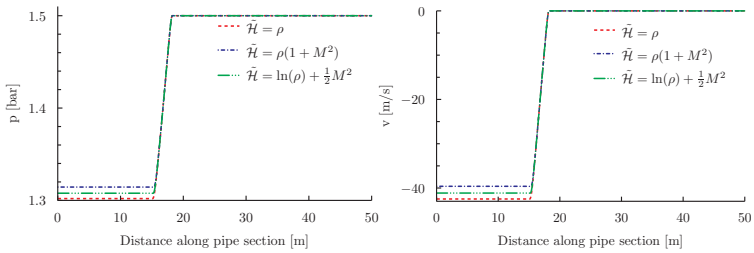

(g) Pressure - pipe section 4 **(h)** Velocity - pipe section 4

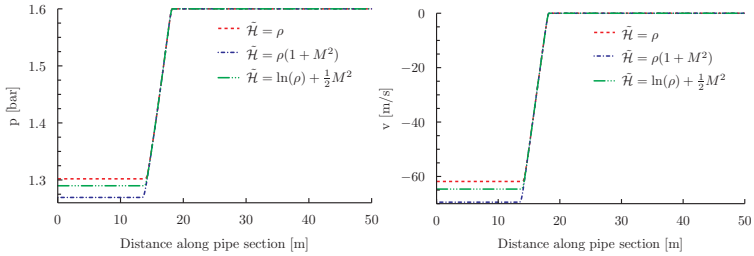

(i) Pressure - pipe section 5 **(j)** Velocity - pipe section 5

Figure 3. Case 1: Pressure and velocity profiles at $T = 0.06\,\mathrm{s}$ for the three different momentum related coupling constants.

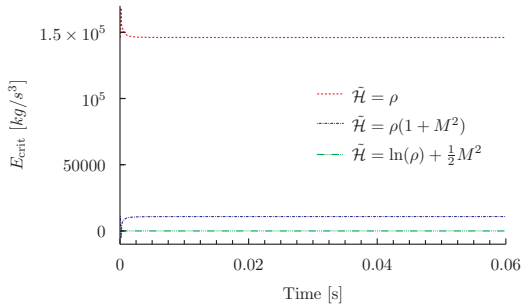

Figure 4. Case 1: Entropy function values for the three different network models. Unphysical solutions are characterised by $E_{\text{crit}} > 0$.

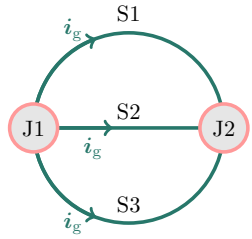

(a) Principal diagram

(b) Relation between the global axis, $\boldsymbol{i}_g$, and the local axis, $\boldsymbol{i}_l$, used by the network model.

Figure 5. Closed system consisting of three sections and two junctions.

2.2. **Case 2: A Closed System of Three Pipe Sections and Two Junctions.** An outline of the closed system is shown in Figure 5a. Three pipe sections, labelled S1 to S3, each of length $L = 50\,\text{m}$, are connected by two junctions. The global axis direction, $\boldsymbol{i}_g$, is set in the direction from junction J1 to junction J2, as indicated in the figure. It should be noted that for junction J2, the global axis and the local axis, $\boldsymbol{i}_l$, that is applied by the network theory are of opposite directions, see Figure 5b.

Initially, the pipe sections are filled with stagnant fluid of uniform pressure. At $T = 0.0\,\text{s}$ two waves enter each pipe section as the interaction between the fluids is initiated. The initial conditions are summarised in Table 2.

Figure 6 presents grid refinement results for the first pipe section, $S1$, using pressure as momentum related coupling constant. However, results for the other pipe sections and coupling

Pipe section	p [bar]	v [m/s]
1	1.0	0.0
2	1.5	0.0
3	1.9	0.0

Table 2. Case 2: Initial conditions

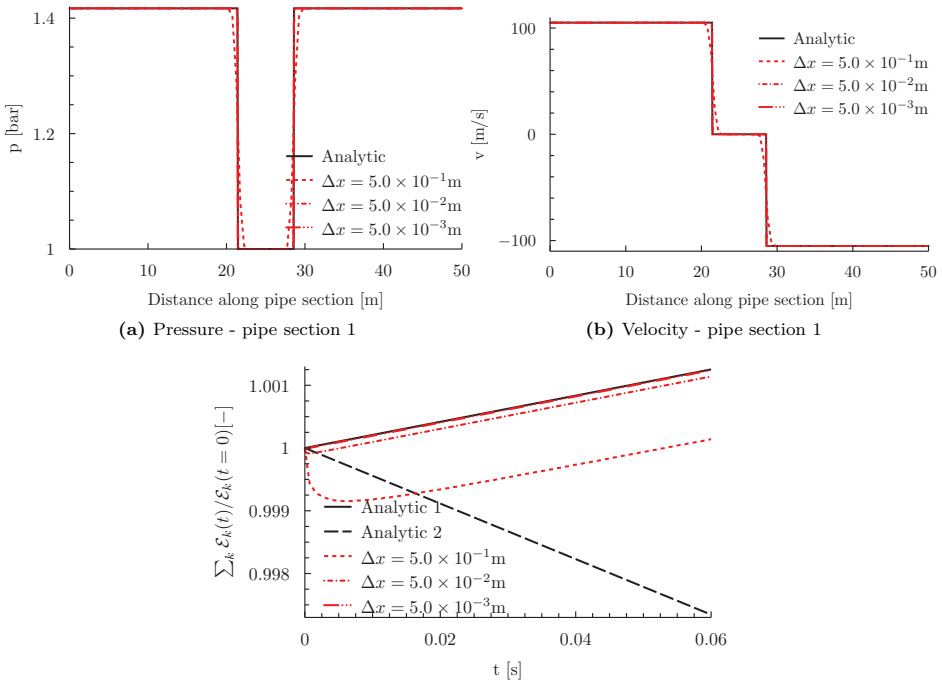

(a) Pressure - pipe section 1

(b) Velocity - pipe section 1

(c) Total energy relative to initial condition

Figure 6. Case 2, pipe section 1: Comparison between numerical and analytical results. ($\tilde{\mathcal{H}} = \rho$, $T = 0.06\,\mathrm{s}$)

constants are comparable. The analytical pressure- and velocity profiles in Figure 6a and 6b are solutions to standard Riemann problems, as in the previous case.

Figure 6c shows the total energy of the system as function of time. The grid refinement results are compared against the "Analytic 1" profile, while the "Analytic 2" profile is used to identify energy production or dissipation at the junctions. The application of the latter profile will be described later.

The derivation of the two analytic energy profiles are described in [7], and the profiles may be calculated as the waves in each pipe have not yet interacted at $T = 0.06\,\mathrm{s}$.

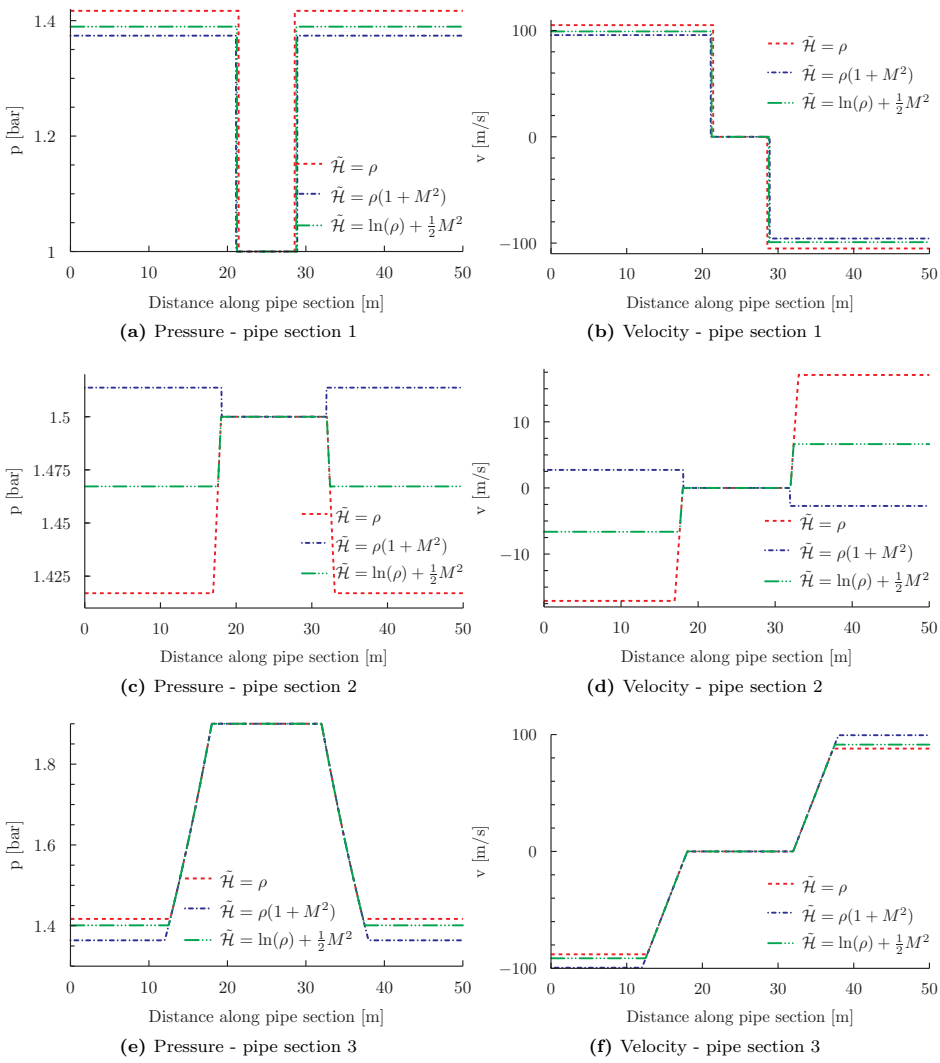

(a) Pressure - pipe section 1 **(b)** Velocity - pipe section 1

(c) Pressure - pipe section 2 **(d)** Velocity - pipe section 2

(e) Pressure - pipe section 3 **(f)** Velocity - pipe section 3

Figure 7. Case 2: Pressure and velocity profiles at $T = 0.06\,\mathrm{s}$ for the three different momentum related coupling constants.

Figure 6a and 6b shows that only the coarsest grid of $\Delta x = 5.0 \times 10^{-1}\,\mathrm{m}$ produces simulation results that deviates significantly from the analytical pressure and velocity profiles. From Figure 6c, however, we see that in order to get accurate energy results a grid of $\Delta x = 5.0 \times 10^{-3}\,\mathrm{m}$ is needed. Thus, this was selected as grid size.

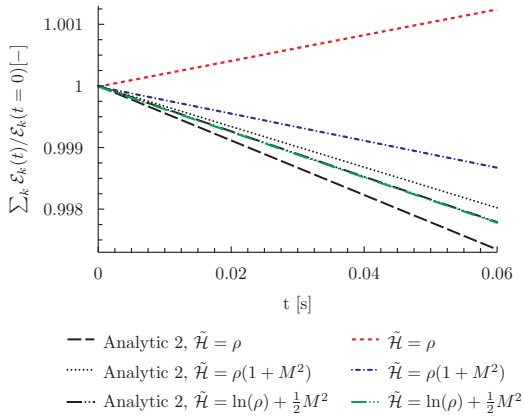

Figure 8. Case 2: Energy-profiles for the three different momentum related coupling constants.

Pressure- and velocity profiles for each of the three pipe sections and each of the momentum related coupling constants are presented in Figure 7. In the first pipe section, $S1$, the three coupling constants all predict that two shock waves will enter. Similarly, two rarefaction waves are predicted to propagate into the third pipe section. In the second pipe section, the three models yields different kind of waves. The models using pressure and Bernoulli invariant as momentum related coupling constant predict two rarefaction waves to enter, while the model using momentum flux predicts shock waves. This is due to the predicted pressure at the pipe-junction boundary, p_2^*. Momentum flux as coupling constant results in a pressure which is larger than the pressure within the pipe, $p_2^* > \bar{p}_2$. The two other models predict pressures that are lower. Correspondingly, the Lax-criterion for shock- and rarefaction waves results in the difference in predicted wave type [3].

Total energy as function of time is showed in Figure 8 and 9. In Figure 8 numerical results are compared to analytical profiles derived under the constraint of energy conservation at the junctions. Figure 9 presents long term numerical results, for which no analytical profiles are available.

The physical soundness of the numerical solutions showed in Figure 8 is determined by a comparison with the profiles denoted "Analytic 2". If the numerical profiles show a larger total energy than the corresponding analytic curve, energy production is present in the numerical results, and thus the solutions are unphysical [7].

As earlier predicted, models with momentum flux or pressure as momentum related coupling constant yield unphysical solutions for the selected set of initial data [6]. Using the Bernoulli invariant as coupling constant results in energy conservation at the junctions.

The development of the total energy until $T = 1.00\,\mathrm{s}$ is found in Figure 9. A net reduction in total energy may be observed for all three network models. The influence of the energy production in the junctions is clearly seen for pressure as momentum related coupling constant, as the profile does not decrease monotonically. In general, for certain sets of initial data, non-monotonicity will as well be observed for momentum flux as coupling constant.

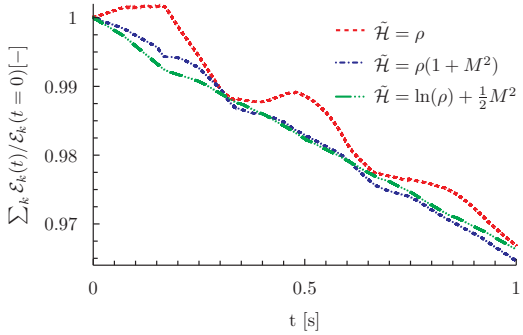

Figure 9. Case 2: Energy-profiles for the three different momentum related coupling constants.

3. Summary

Numerical results from three different network models have been investigated, mainly in terms of physical soundness. Results from two different network layouts, one open and one closed, are considered. Two layout-related evaluation approaches are applied, and unphysical solutions are identified as those with energy production in one or more junctions. The two test cases show that the models including pressure or momentum flux as coupling constant have unphysical solutions for the selected initial data. The network model which uses Bernoulli invariant as coupling constant has physical solutions, as energy is conserved at the junctions.

This is in accordance with analytical results; only Bernoulli invariant yields physical solutions for all subsonic initial conditions [6].

Acknowledgements

The work of the first author was financed through the research project *Enabling low emission LNG systems*. The author acknowledges the project partners; Statoil and GDF SUEZ, and the Research Council of Norway (193062/S60) for support through the *Petromaks* programme.

References

[1] M. K. Banda, M. Herty and A. Klar, Gas flow in pipeline networks, *Netw. Heterog. Media* **1**, 41–56, (2006).
[2] M. K. Banda, M. Herty and A. Klar, Coupling conditions for gas networks governed by the isothermal Euler equations, *Netw. Heterog. Media* **1**, 295–314, (2006).
[3] R. M. Colombo and M. Garavello, A well posed Riemann problem for the p-system at a junction, *Netw. Heterog. Media* **1**, 495–511, (2006).
[4] M. Garavello, A review of conservation laws on networks, *Netw. Heterog. Media*, **5**, 565–581 (2010).
[5] M. Herty and M. Seaïd, Simulation of transient gas flow at pipe-to-pipe intersections, *Netw. Heterog. Media* **56**, 485–506, (2008).
[6] G. A. Reigstad, T. Flåtten, N. E. Haugen and T. Ytrehus, Coupling constants and the generalized Riemann problem for isothermal junction flow, *Submitted* (2013).
[7] G. A. Reigstad, Numerical network models and entropy principles for isothermal junction flow, *Accepted by Netw. Heterog. Media* (2013).

F

Paper V - Existence and Uniqueness of Solutions to the Generalized Riemann Problem for Isentropic Flow

Author: Gunhild A. Reigstad

To be submitted

Is not included due to copyright